

OCEAN

ENGINEERING

GROUP

Computational Modeling of Rudder Cavitation and
Propeller/Rudder Interaction

Shreenaath Natarajan

August 2003

Report No. 03-5

ENVIRONMENTAL AND WATER RESOURCES ENGINEERING

DEPARTMENT OF CIVIL ENGINEERING

THE UNIVERSITY OF TEXAS AT AUSTIN

Austin, TX 78712

Copyright
by
Shreenaath Natarajan
2003

**Computational Modeling of Rudder Cavitation and
Propeller/Rudder Interaction**

by

Shreenaath Natarajan, B.Tech.

Thesis

Presented to the Faculty of the Graduate School
of The University of Texas at Austin
in Partial Fulfillment
of the Requirements
for the Degree of

Master of Science in Engineering

The University of Texas at Austin

August 2003

Computational Modeling of Rudder Cavitation and Propeller/Rudder Interaction

APPROVED BY
SUPERVISING COMMITTEE:

Supervisor: _____
Spyros A. Kinnas

To my parents and my sister

Acknowledgements

First and foremost, I would like to thank my supervisor, Professor Spyros A. Kinnas with greatest appreciation and gratefulness. His encouragement and support has inspired me over the last two years of my graduate school. His enthusiasm and bright ideas has always helped me give my very best. This thesis marks the culmination of a two year learning process, over these years, he has been a patient teacher, a mentor, an advisor and for all this, sir, I thank you.

I would also like to thank Dr. Loukas F. Kallivokas for taking his time off the busy schedule and reading this thesis and providing me with invaluable assistance and encouragement.

I would like to take this opportunity to thank my family. Their encouragements and confidence in me and my abilities has made me scale new heights.

I would like to thank the Offshore Technology Research Center and the following members of Phase III of the University/Navy/Industry Consortium on Cavitation Performance of High Speed Propulsors for supporting the research work: AB Volvo Penta, American Bureau of Shipping, El Pardo Model Basin, Hyundai Maritime Research Institute, Kamewa AB, Michigan Wheel Corporation, Naval Surface Warfare Center Carderock Division, Office of Naval Research (Contract N000140110225), Ulstein Propeller AS, VA Tech Escher Wyss GMBH, Wärtsilä Propulsion Netherlands B.V. and Wärtsilä Propulsion Norway AS. Finally, I would

like to thank the faculty of the College of Engineering at The University of Texas at Austin for the excellent education I received.

Computational Modeling of Rudder Cavitation and Propeller/Rudder Interaction

by

Shreenaath Natarajan, M.S.E.

The University of Texas at Austin, 2003

SUPERVISOR: Spyros A. Kinnas

An iterative method which couples a finite volume method, a vortex-lattice method and, a boundary element method is developed to analyze the cavitating performance of marine rudders subject to the propeller induced flow. The present method also accounts for the effect of a hull or the walls of a tunnel. The cavitating flow around the rudder and the inflow to the rudder, as induced by the propeller, are solved for separately.

The cavitating flow around the rudder is modeled by a low-order potential based boundary element method. The three-dimensional flow induced by the propeller on the rudder is predicted by a three-dimensional Euler solver coupled with a lifting surface vortex-lattice method. The propeller is modeled via body forces in the Euler solver. The three-dimensional effective wake for the propeller is evaluated by subtracting from the total inflow (determined via the Euler solver) the velocities induced by the propeller (determined via the vortex-lattice method).

Once the propeller induced flow to the rudder is evaluated, the boundary element method is used to predict the cavity patterns on the rudder. The presence of the hull is included by considering the image of the rudder with respect to the hull. The results of the present method are validated versus those of other methods and available analytical solutions. Comparisons of the predicted cavity shapes for a horn-type rudder with the observed cavity shapes from an experiment are presented. The boundary element method is also extended for rudders with flap and twisted rudders.

The propeller-rudder interaction is predicted by a three-dimensional Euler solver, using a multi-block approach. The propeller is represented by body forces in one finite volume block, whereas the rudder is represented as a solid boundary in the other finite volume block. The flow inside each of the two blocks is solved separately, and the interaction between the two blocks is accounted for iteratively. Overlapping structured grids are used in the two blocks which exchange information on their boundaries through interpolation.

Table of Contents

Acknowledgements	v
Abstract	vii
List of Tables	xii
List of Figures	xiii
Nomenclature	xix
Chapter 1. Introduction	1
1.1 Background	1
1.2 Motivation	4
1.3 Objective	5
1.4 Overview	6
Chapter 2. Literature Review	8
2.1 Vortex-Lattice Method	8
2.2 Boundary Element Method	9
2.3 Effective Wake Prediction	10
2.4 Propeller-Rudder Interaction	11
2.4.1 Multi-Block Scheme	12
Chapter 3. Formulation and Numerical Implementation	15
3.1 Euler Equations	15
3.2 Steady Euler Solver	16
3.2.1 Axisymmetric Steady Euler Solver	17
3.2.2 Three-dimensional Steady Euler Solver	20
3.2.3 Boundary Conditions	23
3.3 Potential Flow Solver	28

3.3.1	Boundary Element Method	28
3.3.2	Vortex-Lattice Method	37
Chapter 4.	Convergence and Validation Studies	39
4.1	Rudder with Image model	40
4.1.1	Convergence Studies	41
4.2	Validation for the Elliptic Wing	46
4.2.1	Convergence Studies	49
4.3	Comparison with Experimental Observations	54
4.3.1	Summary of the Experiment	54
4.3.2	Definition of Rudder Angles	56
4.3.3	Test Conditions Selected for Comparisons	57
4.3.4	Nominal Wake at the Propeller Plane	59
4.3.5	Prediction of Effective Wake	62
4.3.6	Determining Inflow to the Rudder	64
4.3.7	Comparison with Observations from Experiments	69
4.4	Flapped Rudder	72
4.4.1	Convergence Studies for a Flapped Rudder	75
4.4.2	Results for a Flapped Rudder	78
4.5	Twisted Rudder	83
Chapter 5.	The Propeller-Rudder Interaction	87
5.1	Grid Generation	88
5.2	Boundary Conditions	92
5.2.1	Fourth-order Smoothing	94
5.3	Results for Flow Around the Rudder	97
5.4	Validation tests	101
5.4.1	Inclusion of the Tunnel Effects in the BEM	101
5.4.2	Comparison of the Results from the Euler and the Panel Method	103
5.5	Multi-Block Method	108
5.5.1	Iterative Process to Compute the Effective Wake	108
5.5.2	Interpolation Scheme	110
5.5.3	Validation of the Interpolation scheme	113

5.6	Results of Propeller-Rudder Interaction	117
5.6.1	Results for a Straight Rudder	117
5.6.2	Results for a Horn-type Rudder	122
Chapter 6.	Conclusions and Recommendations	127
6.1	Conclusions	127
6.2	Recommendations	128
	Bibliography	131
	Vita	141

List of Tables

4.1	Test conditions simulated in the model water tunnel testing facility .	58
4.2	The values of various coefficients using the nominal and the effective wake	65

List of Figures

1.1	Sketches of cavitation pattern observed in a water tunnel testing facility, over the horn-type rudder at an angle of attack $\alpha = 5^\circ$ and at a cavitation number of $\sigma_R = 1.24$ (top) and $\sigma_R = 1.65$ (bottom). . .	3
3.1	Ship-fixed Cartesian coordinate system (taken from [Choi 2000]) . .	17
3.2	Cell (i, j, k) on which the finite volume method is applied (taken from [Choi 2000])	21
3.3	Boundary conditions for the Euler solver which evaluates the propeller induced inflow to the rudder	25
3.4	Boundary conditions on the domain (shown at an axial location) . .	26
3.5	Potential flow around a cavitating rudder subject to the propeller induced flow	28
3.6	Rudder with partial cavity and the required physical conditions . . .	31
3.7	Rudder with the inflow mirrored with respect to the hull	36
3.8	Rudder with the influence from the images with respect to the hull .	37
4.1	Rudder with the inflow mirrored with respect to the hull	40
4.2	Cylindrical grid at the inflow plane of the tunnel	41
4.3	Solution at the center plane of the domain obtained from the 3-D Euler solver, including the tunnel wall effects	42
4.4	Convergence of circulation with number of panels in the chordwise direction. $R = 0$ is the lower tip and $R = 0.5$ is the upper tip of the rudder (close to the hull)	43
4.5	Convergence of circulation with number of panels in the spanwise direction. $R = 0$ is the lower tip and $R = 0.5$ is the upper tip of the rudder (close to the hull)	44
4.6	Convergence of pressure distribution along the strip at $y/R = 0.34$.	44
4.7	Convergence of cavitation volume with total number of panels . . .	45
4.8	The elliptic planform wing with an elliptic cross-section of 0.0125 thickness to chord ratio, used in the validation of PROPCAV in wetted flow.	47
4.9	Circulation distribution predicted by PROPCAV and analytical, for an elliptic wing	47

4.10	Lift coefficients, predicted by PROPCAV and analytical, for an elliptic wing at various ratios	48
4.11	Lift and drag coefficients, predicted by PROPCAV and analytical, for an elliptic wing at various angles of attack	48
4.12	The grid at the inflow plane of the domain used in GBFLOW-3D showing the boundary conditions applied	49
4.13	Solution at the center plane of the domain obtained from the 3-D Euler solver, with hull effects	50
4.14	Convergence of circulation distribution with the number of panels in the chordwise direction. $R = 0$ is the lower tip and $R = 1.0$ is the upper tip of the rudder (close to the hull)	51
4.15	Convergence of circulation distribution with the number of panels in the spanwise direction. $R = 0$ is the lower tip and $R = 1.0$ is the upper tip of the rudder (close to the hull)	52
4.16	Convergence of pressure distribution along the strip at $y/R = 0.34$.	52
4.17	Convergence of cavitation volume with total number of panels	53
4.18	Photograph of a horn-type rudder geometry (top) with corresponding BEM model (bottom)	55
4.19	Cartesian coordinate system used in 3-D BEM formulation	56
4.20	Definition of the rudder angle in the experiment	57
4.21	Definition of the angle of attack used in the BEM solver	58
4.22	Measured axial nominal wake as seen by the propeller	60
4.23	Nominal wake at the propeller plane reconstructed from the harmonic analysis of the data shown in the previous figure	61
4.24	Computational domain used in GBFLOW-3D with the tunnel walls and the propeller shown. Only one half of the whole domain is shown.	62
4.25	Effective wake predicted at the propeller plane, including the propeller-tunnel interaction	63
4.26	Advance ratio predicted for the design $K_T = 0.2012$ for the predicted effective wake through trial and error	64
4.27	Comparison of the loading on the propeller predicted by MPUF-3A using the provided nominal wake and the predicted effective wake .	65
4.28	Predicted axial velocity contours and streamlines of the propeller flow field at the center plane of the domain	66
4.29	Predicted pressure contours and streamlines of the propeller flow field at the center plane of the domain	67
4.30	Tangential velocity contours and streamlines of the propeller flow field at the center plane of the domain	67

4.31	Tangential velocity contours and total velocity vectors induced by the propeller to the horn-type rudder	68
4.32	Cavity pattern observed (top) and predicted by PROPCAV (bottom) on the port side at a cavitation number $\sigma_R = 1.24$ and $\alpha = 5^\circ$	70
4.33	Cavity pattern observed (top) and predicted by PROPCAV (bottom) on the port side at a cavitation number $\sigma_R = 1.65$ and $\alpha = 5^\circ$	71
4.34	Definition of pivot axis and flap angle for flapped rudder	73
4.35	Re-paneled geometry of the flapped rudder with a flap angle $\alpha_{flap} = 10^\circ$ and flap pivot axis $X_f/C_{bot} = 0.75$	74
4.36	Convergence of circulation in chordwise direction for a rudder with flap angle, $\alpha_{flap} = 10^\circ$ and $X_f/C_{bot} = 0.75$	76
4.37	Convergence of circulation in spanwise direction for a rudder with flap angle, $\alpha_{flap} = 10^\circ$ and $X_f/C_{bot} = 0.75$	76
4.38	Location of the panel strip along the span of the rudder at which the convergence of pressure distribution with the number of chordwise panels is studied	77
4.39	Convergence of pressure distribution (along the strip-6 shown in Figure 4.38) for a rudder with flap angle, $\alpha_{flap} = 10^\circ$ and $X_f/C_{bot} = 0.75$	77
4.40	Lift and drag coefficients for a flapped rudder with varying flap angles subjected to a uniform inflow	79
4.41	Circulation distribution for a flapped rudder with varying flap angles subjected to a uniform inflow	79
4.42	Cavitation for a flapped rudder subjected to a uniform inflow at a cavitation number $\sigma_R = 0.55$ and a flap angle $\alpha_{flap} = -10^\circ$; predicted by PROPCAV	80
4.43	Cavitation for a flapped rudder subjected to a uniform inflow at a cavitation number $\sigma_R = 0.55$ and a flap angle $\alpha_{flap} = 10^\circ$; predicted by PROPCAV	80
4.44	Axial velocity contours and streamlines of the propeller flow field at the center plane of the domain	81
4.45	Tangential velocity contours and streamlines of the propeller flow field at the center plane of the domain	81
4.46	Cavitation for a flapped rudder subjected to an inflow induced by the propeller at a cavitation number $\sigma_R = 2.0$ and a flap angle $\alpha_{flap} = 0^\circ$	82
4.47	Cavitation for a flapped rudder subjected to an inflow induced by the propeller at a cavitation number $\sigma_R = 2.0$ and a flap angle $\alpha_{flap} = -10^\circ$	82

4.48	BEM model of the twisted rudder geometry	84
4.49	Twist angle in degrees over the span of the rudder. S=0 is the lower tip of the rudder and S=1.0 is the upper tip of the rudder.	84
4.50	Tangential velocity contours and total velocity vectors for the propeller induced flow field over the twisted rudder	85
4.51	Cavitation for a twisted rudder subjected to a propeller induced inflow at a cavitation number $\sigma_R = 2.0$ and a maximum twist angle $\alpha_{twist} = 0^\circ$; predicted by PROPCAV	85
4.52	Cavitation for a twisted rudder subjected to a propeller induced inflow at a cavitation number $\sigma_R = 2.0$ and a maximum twist angle $\alpha_{twist} = 7.2^\circ$; predicted by PROPCAV	86
5.1	H-type grid showing the rudder along the meridional plane	89
5.2	Top view of the H-type grid showing the rudder section and the spacing used over a hydrofoil like rudder with $t_{max}/C = 0.2$	90
5.3	Side view H-type grid adapted over a horn-type rudder	90
5.4	Top view of the H-type grid over the section of a horn-type rudder with a NACA66 section ($t_{max}/C = 0.1$)	91
5.5	Boundary conditions on the H-type grid to compute the flow around the rudder	92
5.6	Pseudo cell treatment for the cells forward of leading edge and aft of the trailing edge along the repeat indices	93
5.7	Applying the 4 th -order smoothing along the indices close to the rudder section	96
5.8	Three-dimensional grid used to model the rudder with 20% thickness ratio and NACA66 thickness form	98
5.9	Axial velocity contours at the center plane of the grid for a rudder inside a tunnel	98
5.10	Pressure contours at the center plane of the grid for a rudder inside a tunnel	99
5.11	Axial velocity contours along with stream lines at a rudder section located at $y = 1.0$ (looking from the top wall of the tunnel) close to the top wall of the tunnel. The rudder section is also shown. The values inside the rudder section is due to plotting error.	99
5.12	Tangential velocity contours along with streamlines at a rudder section located at $y = 1.0$ (looking from the top wall of the tunnel) close to the top wall of the tunnel. The rudder section is also shown. The values inside the rudder section is due to plotting error.	100

5.13	Tunnel and hydrofoil, including the images with respect to the top wall (not shown), as modeled through the panel method	103
5.14	Pressure distributions obtained from the 3-D Euler solver and the panel method results are compared in the figures that follow at the shown locations. $y = 0$ is the upper tip (close to the top wall) and $y = 1$ is lower tip of the rudder	105
5.15	Comparison of pressure distributions obtained from the 3-D Euler solver and the panel method for a rudder with $t/C = 0.2$, at sections close to the top wall of the tunnel	106
5.16	Comparison of pressure distributions obtained from the 3-D Euler solver and the panel method for a rudder with $t/C = 0.2$, at sections close to the bottom of the rudder	106
5.17	Comparison of pressure distributions obtained from the 3-D Euler solver and the panel method for a rudder with $t/C = 0.1$, at sections close to the top wall of the tunnel	107
5.18	Comparison of pressure distributions obtained from the 3-D Euler solver and the panel method for a rudder with $t/C = 0.1$, at sections close to the bottom of the rudder	107
5.19	The two blocks used in the 3-D Euler solver	109
5.20	Cylindrical grid used in block-1 at the inflow plane for block-2 (as shown in Figure 5.19)	111
5.21	H-type grid used in block-2 at the outflow plane for block-1 (as shown in Figure 5.19)	111
5.22	Interpolation technique used to transfer data from block-1 to block-2 (top) and block-2 to block-1 (bottom)	112
5.23	Analytical function assumed on the H-type grid (shown in Figure 5.21)	114
5.24	Analytical function recovered on the cylindrical grid (shown in Figure 5.20) after performing interpolations from values in the H-type grid	114
5.25	Local relative error for a function, $f(y, z) = \sqrt{y^3 + z^3} + 1$	115
5.26	Analytical function recovered on the H-type grid (shown in Figure 5.21) after performing interpolations from values in the H-type grid	116
5.27	Local relative error for a function, $f(y, z) = \sqrt{y^3 + z^3} + 1$	116
5.28	3-D Euler solver grid showing rudder with NACA66 section and 20% thickness ratio	118
5.29	Tangential velocity contours on the center plane of Block-1 and 2 for a straight rudder	119
5.30	Axial velocity contours on the center plane of Block-1 and 2 for a straight rudder	120

5.31	Effective wake predicted after 3 iterations with the propeller-rudder interaction	120
5.32	Local relative error in axial velocity at a plane $X = 0.3$ in the overlapping zone	121
5.33	Local relative error in tangential velocity at a plane $X = 0.3$ in the overlapping zone	121
5.34	3-D Euler solver grid showing horn-type rudder with NACA0020 section	123
5.35	Tangential velocity contours on the center plane of block-1 and 2 for a horn-type rudder	124
5.36	Axial velocity contours on the center plane of block-1 and 2 for a horn-type rudder	125
5.37	Effective wake predicted after 6 iterations with the propeller-rudder interaction	126
5.38	Convergence of propeller forces with the number of iterations	126
6.1	Tunnel geometry adapted with the top section of the rudder (modeled in BEM)	130
6.2	Torpedo rudder from [Halstensen 2002]	131

Nomenclature

Latin Symbols

A_{H-H}	dipole self-influence coefficients on hydrofoil
A_{H-T}	dipole influence coefficients on hydrofoil due to tunnel
A_{T-H}	dipole influence coefficients on tunnel due to hydrofoil
A_{T-T}	dipole self-influence coefficients on tunnel
B_H	source influence coefficients on hydrofoil
B_T	source influence coefficients on tunnel
AR	Aspect Ratio
C	chord length at each section for 3-D hydrofoil
C_o	chord length at mid-span of 3-D hydrofoil
C_p	pressure coefficient, $C_p = (P - P_o)/(0.5\rho n^2 D^2)$ for propeller $C_p = (P - P_o)/(0.5\rho V_s^2)$ otherwise
C_Q	torque coefficient based on V_s , $C_Q = \frac{Q}{0.5\rho V_s^2 \pi R^3}$
C_T	thrust coefficient based on V_s , $C_T = \frac{T}{0.5\rho V_s^2 \pi R^2}$
D	propeller diameter, $D = 2R$ for propeller $D = 2S$ for rudder
F_n	Froude number based on n , $F_n = n^2 D/g$
Fr_{rudder}	Froude number based on S , $Fr_{rudder} = V_s^2/gS$

g	gravitational acceleration
G	Green's function
h	cavity thickness over the blade surface
J_s	advance ratio based on V_s , $J_s = V_s/nD$
K_Q	torque coefficient, $K_Q = Q/\rho n^2 D^5$
K_T	thrust coefficient, $K_T = T/\rho n^2 D^4$
n	propeller rotational frequency (rev/s)
P	pressure
P_{atm}	atmospheric pressure
P_c	cavitating pressure
P_o	far upstream pressure, at the propeller axis
P_v	vapor pressure of water
p, q	field point and variable point
\vec{q}_t	total velocity
q_c	magnitude of total cavity velocity
R	propeller radius or half span of 3-D hydrofoil
Re	Reynolds number based on reference length L , $Re = \frac{\rho U_\infty L}{\mu}$
S	Span of the rudder
S_B	blade surface
S_C	partial or super cavity surface
S_H	hub surface for propeller foil surface for 3-D hydrofoil
S_W	wake surface

s, v, n	non-orthogonal coordinates on local panel
s, w, n	orthogonal coordinates on local panel
s, u, n	orthogonal coordinates on local wake panel
S_{ij}	area of cell in two-dimensional formulation
t	non-dimensional time
T	propeller thrust, or time period of motion
\mathbf{U}	column matrix for time derivative terms
U_∞	flow velocity at infinity
u, v, w	x, y and z -direction velocities
\vec{v}	$= (u, v, w)$ or (u_x, u_r, u_θ) , total velocity vector
V_s	ship speed
\hat{V}_c	computational cell volume
\vec{x}	$= (x, y, z)$ or (x, r, θ) , location vector on the ship fixed coordinate system
(x, r, θ)	downstream, radial and circumferential coordinates respectively
(x, y, z)	downstream, upward and port side coordinates respectively
X_e	axial location where effective velocity is determined
X_p	axial location of propeller plane

Greek Symbols

α	angle of attack for 3-D hydrofoil
β	artificial compressibility factor
γ	vorticity
Γ	propeller blade circulation
δ	cavity trailing edge thickness for cavity problem
$\delta t, \Delta t$	time step size
Δp	pressure difference
$(\Delta x, \Delta y)$	cell size in x and y direction
μ	dynamic viscosity of water
ν	kinematic viscosity of water
ρ	fluid density
σ	cavitation number based on U_∞ , $\sigma = (P_o - P_c)/(0.5\rho U_\infty^2)$
σ_n	cavitation number based on n , $\sigma_n = (P_o - P_c)/(0.5\rho n^2 D^2)$
σ_R	rudder cavitation number based on V_s , $\sigma_R = (P_o - P_c)/(0.5\rho V_s^2)$
ϕ	perturbation potential
Φ	total potential
ψ	angle between \vec{s} and \vec{v}
ω	propeller angular velocity

Subscripts

$1, 2, 3, 4, \dots$	node numbers
A, B, C, D, \dots	cell indices
(i, j, k)	node or cell indices in each direction; i is axial, j is radial, and k is circumferential.
N, W, S, E, T, B	face (in three-dimension) or edge (in axisymmetric) indices at north, west, south, east, top, and bottom of a cell
T, I, E	total, propeller induced, and effective wake velocities (in some figures)

Superscripts

$n, n + 1$	time step indices
+	upper cavity, or wake surface
-	lower cavity, or wake surface

Acronyms

BEM	Boundary Element Method
CFD	Computational Fluid Dynamics
CPU	Central Processing Unit (time)
DBC	Dynamic Boundary Condition
DTMB	David Taylor Model Basin
DTNSRDC	David Taylor Naval Ship Research and Development Center
FPSO	Floating, Production, Storage and Offloading (vessels)
FVM	Finite Volume Method
KBC	Kinematic Boundary Condition
MIT	Massachusetts Institute of Technology
NACA	National Advisory Committee for Aeronautics
PIV	Particle Image Velocimetry
VLM	Vortex Lattice Method

Computer Program Names

GBFLOW-3X	axisymmetric steady Euler solver
GBFLOW-3D	three-dimensional steady Euler solver
GBFLOW-MB	three-dimensional steady Multi-Block Euler solver
MPUF-3A	cavitating propeller potential flow solver based on VLM
PROPCAV	cavitating propeller potential flow solver based on BEM

Chapter 1

Introduction

1.1 Background

A marine rudder provides directional stability, maneuverability and control to the ship. The rudder's effectiveness in producing a turning moment is proportional to its lift force. Typically, rudders are placed behind the propeller slipstream, where the flow is accelerated, to enhance their effectiveness at low ship speeds.

The complex vortical inflow induced by the propeller on the rudder often causes cavitation on the rudder. This research models sheet cavitation on the rudder. Cavitation occurs when the pressure drops below the saturated vapor pressure, resulting in the formation of continuous vapor filled bubbles or sheet cavities. Other types of cavitation on rudders, such as gap cavitation (occurring in the gap between the flap and the immovable part of the rudder), tip vortex cavitation and hub vortex cavitation will not be addressed in this work. Cavitation can cause serious structural damage at the regions on the rudder surface where the cavities collapse. Cavitation also accelerates erosion. Furthermore, cavitation can cause an increase in rudder drag, ship hull vibration and radiated noise. As a result of these shortcomings, the hydrodynamic performance of the rudder is compromised. Designs that minimize rudder cavitation will decrease maintenance costs and improve performance.

Over the years, the reduction of cavitation and the improvement of performance have been important factors in the design of rudders. [Shen et al. 2000] developed a twisted rudder that avoids cavitation under normal loading conditions. The shape of the rudder matches the complex flow in the wake of the propeller. This reduces cavitation by reducing the angle of attack to the rudder sections due to the propeller swirl. Flapped rudders provide higher lift forces at smaller flap angles. As a result, flapped rudders exhibit better maneuvering characteristics than all-movable rudders. A horn-type rudder is commonly used in high displacement container ships where the hydrodynamic loading on the rudder is large. Blade sheet cavitation appears initially close to the leading edge. As the angle of attack or the ship speed increase, sheet cavitation grows over the rudder surface. Sheet cavitation, seen close to the bottom leading edge, and other types of cavitation, as mentioned above, are shown on a horn-type rudder in Figure 1.1.

One of the most challenging tasks in modern ship design is predicting propeller-rudder interaction; the effect of the rudder on the performance of the propeller and vice-versa. Multi-component propulsors offer higher efficiencies due to the cancellation of the vortical flow downstream of the propeller. The loading on the propeller also decreases as the loading is shared by the components. Types of multi-component propulsors include contra-rotating propellers, stator-rotor propulsors, as well as podded or ducted propulsors. The task of predicting the performance becomes more challenging with the increase in the number of components in the propulsion system.

In practice, potential flow theory based methods are used to evaluate the performance of a propeller in the ship wake inflow. As shown in [Kinnas et al. 2002]

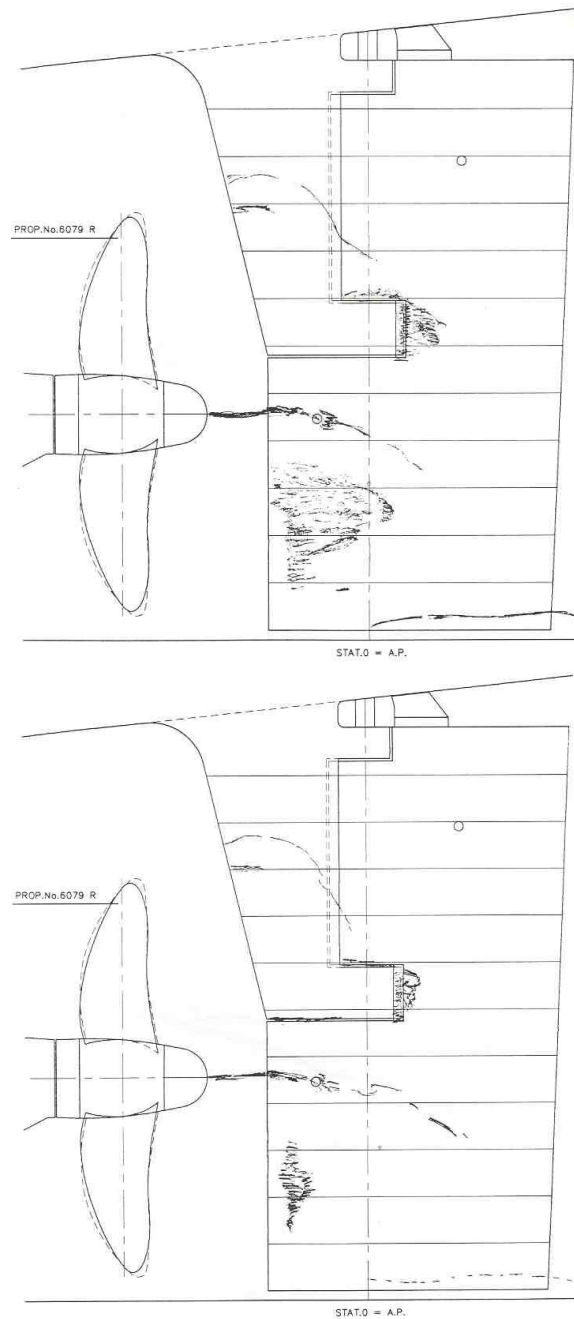


Figure 1.1: Sketches of cavitation pattern observed in a water tunnel testing facility, over the horn-type rudder at an angle of attack $\alpha = 5^\circ$ and at a cavitation number of $\sigma_R = 1.24$ (top) and $\sigma_R = 1.65$ (bottom).

these methods are capable of predicting the propeller performance (including the effects of cavitation) for a wide range of operating conditions. Similar strategies are adopted for evaluating the performance of a rudder subject to the inflow induced by the propeller. The time-efficiency of these methods is the main reason for their widespread use. However, potential flow theory based methods neglect the effect of vortical inflow. Hence the concept of *effective wake* is introduced:

Effective wake is the corrected inflow which includes the interaction between the propeller, the rudder, and the vorticity in the inflow.

1.2 Motivation

The hydrodynamic loading of propellers and rudders has been continuously increasing with the increasing need for ships of higher displacement. This higher load further exacerbates the serious problem of cavitation on propeller and rudder surfaces. The accurate analysis of the flow around a rudder in the influence of the propeller is a challenging task. The hydrodynamic interaction between the propeller and the rudder is of great importance because of its effect on the performance of both.

Surface panel methods have been applied successfully for the analysis of marine propulsors and all-movable rudders. A three-dimensional Finite Volume Method (FVM) based Euler solver coupled with a Vortex Lattice Method (VLM) based potential flow solver have been applied to predict the performance of single propellers [Choi 2000] and [Choi and Kinnas 2001], and more recently, to predict the performance of multi-component propulsor systems, including podded propulsors and ducted propulsors [Kinnas et al. 2002].

The above mentioned iterative procedure can be used to predict the inflow to the rudder induced by the propeller. This work aims at predicting the cavitation over the rudder using the inflow induced by the propeller. This work will also address the development of an algorithm for predicting propeller-rudder interaction, which can lead to an improved prediction of cavitation and hydrodynamic forces on the rudder.

1.3 Objective

The objectives of this research are: (a) to develop a robust and computationally efficient numerical method which can predict sheet cavitation (midchord, face or back cavitation) and the hydrodynamic forces on the rudder subject to a known inflow; (b) to evaluate the inflow to the rudder induced by the propeller; and (c) to determine the propeller-rudder interaction.

The following approach is adopted in order to achieve these objectives:

1. The cavitating flow around the rudder is modeled via a low order boundary element method based on the perturbation potential.
2. The three-dimensional inflow over the rudder induced by the propeller is obtained by a three-dimensional Euler solver.
3. The propeller-rudder interaction is considered by a three-dimensional Euler solver using a multi-block approach. Overlapping non-matching grids are used in the two blocks, with the propeller being represented by body forces in one finite volume block, and the rudder being represented as a solid boundary in the other finite volume block. Iterations are performed between the two

blocks, by exchanging information on their boundaries through interpolations, in order to predict the effective wake to the propeller.

4. The results from the present method are validated using the results of other numerical methods or available analytical solutions, as well as observations in an experiment.

1.4 Overview

This dissertation is organised into four main chapters.

Chapter 1 contains background, motivation and objectives of this research.

Chapter 2 presents a literature review of previous work on prediction of performance of rudders as well as propeller-rudder interaction.

Chapter 3 describes in detail the numerical formulation of a three-dimensional FVM based Euler solver. This chapter also describes the three-dimensional formulation of a Boundary Element Method (BEM) used for determining the cavitation over the rudder. The implementation of hydrostatic effects and hull effects are also discussed in this chapter. For completeness, a brief overview of the VLM based potential flow solver, used in the propeller analysis, is also provided.

Chapter 4 presents several validation tests and convergence studies. This chapter also presents the comparison of the predicted cavity shapes with the observed cavity shapes from the experiments for a horn-type rudder. Results for a flapped rudder and a twisted rudder are also presented.

Chapter 5 details the propeller-rudder interaction which couples the VLM and the

Euler solver. The multi-block approach which is adopted to predict the propeller-rudder interaction is also described. The chapter includes sections on the grid generation scheme and the boundary conditions used in the Euler solver. The results from the 3-D Euler solver are validated with the results from the BEM solver in the case of a rudder subjected to uniform inflow. Validation tests for the interpolation scheme used for the exchange of boundary information between blocks, and results from the propeller-rudder interaction scheme are presented in this chapter.

Chapter 6 presents a summary and the conclusions of this thesis and some recommendations for future work.

Chapter 2

Literature Review

2.1 Vortex-Lattice Method

A vortex-lattice method was introduced for the analysis of fully wetted unsteady performance of marine propeller subjected to non-uniform inflow by [Kerwin and Lee 1978]. This method is classified as a lifting surface vortex-lattice method (VLM). The method was later extended to treat unsteady cavitating flows by [Lee 1979] and [Breslin et al. 1982] using the linearized cavity theory. The linear theory cannot capture the correct effect of blade thickness on cavity, and [Kerwin et al. 1986], [Kinnas 1991] implemented the leading edge correction to take into account the non-linear blade thickness effect. The method was later extended to predict unsteady partial cavitation with the prescribed mid-chord cavity detachment location by [Kinnas and Fine 1989], and the steady super cavitation by [Kudo and Kinnas 1995]. The search algorithm for cavity detachment in the case of back mid-chord cavitation was added by [Kinnas et al. 1998a], and the code was named MPUF-3A.

In MPUF-3A, the discrete vortices and sources are placed on the mean camber surface of the blade. A robust arrangement of the singularities and the control point locations is employed to produce accurate results [Kinnas and Fine 1989]. The unknown strengths of the singularities are determined so that the kinematic and dy-

dynamic boundary conditions are satisfied at the control points on the mean camber surface. The kinematic boundary condition requires the flow to be tangent to the mean camber surface. The dynamic boundary condition requires the pressure on the cavity to be equal to the vapor pressure, and is applied only at the control points in the cavitating part of the blade.

The latest version of MPUF-3A also includes wake alignment in circumferentially averaged inflow [Greeley and Kerwin 1982], non-linear thickness-loading coupling [Kinnas 1992], the effect of hub, and wake alignment in the case of inclined shaft [Kinnas and Pyo 1999].

2.2 Boundary Element Method

Since the boundary element method discretizes the blade surface instead of the mean camber surface, the effect of the non-linear thickness-loading coupling is inherently included. Also, the BEM captures the flow details at the propeller leading edge and tip more accurately than the VLM.

The perturbation potential based panel method was introduced for the analysis of non-cavitating propeller performance in steady flow by [Lee 1987; Kerwin et al. 1987], and in unsteady flows using the hyperboloidal geometry panel by [Hsin 1989; Kinnas and Hsin 1992].

In [Kinnas and Fine 1992], [Kinnas and Fine 1993a] and [Kinnas and Fine 1993b], a low-order potential-based boundary element method was introduced for the non-linear analysis of 3-D flow around cavitating hydrofoils or cavitating propellers subjected to non-axisymmetric inflows. The method was named PROPCAV, and was

later extended to predict leading edge and mid-chord partial cavitation on either the face or the back of the blades by [Mueller and Kinnas 1999]. Young and Kinnas [1999, 2001] extended PROPCAV to treat the mixed partial and super cavity on both back and face sides of the blades (or hydrofoils) simultaneously. Recently, PROPCAV was further extended to treat super-cavitating propellers with finite thickness trailing edge as well as surface piercing propellers by Young and Kinnas [2001, 2003b]. The treatment of a developed tip vortex cavity and a fully unsteady wake alignment procedure were also incorporated in PROPCAV by Lee and Kinnas [2001, 2003].

In the present work, the hydrofoil version of PROPCAV is used to determine several types of sheet cavitation (mid-chord, face and or back) on constant chord rudders, horn-type rudders, flapped rudders, and twisted rudders.

2.3 Effective Wake Prediction

Effective wake is the corrected inflow to the propeller which is evaluated by subtracting from the total inflow (determined in the 3-D Euler solver) the velocities induced by the propeller (determined in MPUF-3A). It is well known that the accurate prediction of the effective wake is very crucial in determining the cavity extent and volume on the propeller blades, as well as the magnitude of the predicted pressure pulses on the hull.

Experimental investigations and theoretical studies using the steady axisymmetric Euler equations were first presented by [Huang et al. 1976; Huang and Cox 1977] and [Huang and Groves 1980; Shih 1988], respectively.

Later, effective wake prediction methods using RANS (Reynolds Averaged Navier-Stokes) equations were developed for axisymmetric flow applications [Stern et al. 1988a,b; Kerwin et al. 1994, 1997]. [Stern, 1994] applied the RANS equations to non-axisymmetric inflow applications, and their work addressed propeller-hull interaction and the differences between nominal and effective wakes. In both methods, the propeller was represented by body force terms in the RANS equations.

In [Choi and Kinnas 1998], [Kinnas et al. 2000], [Choi and Kinnas 2001] a steady 3-D Euler solver (WAKEFF-3D), based on a finite volume approach and the artificial compressibility method, was developed for the prediction of the 3-D effective wake of single propellers in unbounded flow or in the presence of a circular section tunnel. In [Choi and Kinnas 2003], [Choi and Kinnas 2000b], [Choi and Kinnas 2000a] and [Choi 2000], a fully three-dimensional unsteady Euler solver (WAKEFF-3U), based on a finite volume approach and the pressure correction method, was developed and applied to the prediction of the unsteady effective wake for propellers subject to non-axisymmetric inflows. It was found that the 3-D Euler solver (WAKEFF-3D) predicted a 3-D effective wake inflow which was very close to the time average of the fully unsteady wake inflow (predicted by WAKEFF-3U).

2.4 Propeller-Rudder Interaction

The hydrodynamic interaction between propeller and rudder is of great importance because of its effect on the performance of both. [Molland 1981] performed a wind tunnel experiment on rudders operating behind a propeller without a ship hull. A systematic series of tests on various propeller-rudder configurations were carried out with a zero rudder angle by [Stierman 1989]. [Tamashima et al. 1993] used a

simplified propeller theory, which treats the propeller as an actuator disc, to calculate the performance of the propellers, and a panel method to calculate the forces acting on the rudder. In [Han et al. 1999], they developed a numerical technique using BEM to analyze the propeller-rudder interaction, and the calculated results were compared with the measurements obtained from experiments. The effect of ship hull and the propeller on the rudder cavitation were studied through a series of experiments Shen et al. [1997]. In addition, the surface pressure distributions measured over the rudder were compared with the pressure distributions predicted by panel methods.

[Han et al. 2001] used a surface panel method to solve the flow around a horn-type rudder and a vortex-lattice method to solve the flow around the propeller, respectively. The three-dimensional flow around the rudder and the propeller was computed simultaneously, considering the interactions between them. The surface pressure distributions and the cavity patterns on the horn-type rudder were calculated and compared with the measurements in experiments conducted at Samsung Ship Model Basin (SSMB).

2.4.1 Multi-Block Scheme

Multi-block methods have been developed to perform the numerical flow simulations around complex geometries such as:

1. Computation of flow around bodies which move relative to each other. Examples: (a) stator-rotor interaction in a hydraulic turbine, (b) propeller-hull interaction, (c) propeller-rudder interaction. In all the above cases there is a relative motion between the components.

2. Computation of time-accurate unsteady solutions. In this case, the grid has to be recalculated after each time step. Interpolations are performed from the grids in one reference frame to the other at the interfaces. Grids of this kind are called *Chimera grids*.

In the design of hydraulic turbines, it is a fairly standard practice to simulate the different components separately. Since there are strong interactions between the components, many attempts have been made lately to introduce this interaction through different coupling procedures. In [Ruprecht et al. 1999a] and [Ruprecht et al. 1999b], the interaction between a stator and rotor was analyzed for an axial type hydraulic turbine. The calculation was performed in parallel. The parallelization was obtained by decomposing the domain into two blocks with overlapping meshes. The interaction of the rotor and the stator was obtained through interpolations, which were performed on the sliding interface, where the flux integrals were exchanged at the nodes.

[Hyams et al. 2000] developed a RANS incompressible flow solver for performing time-accurate, viscous, high Reynolds number flow simulations, around a ship hull with stern appendages using multi-element non-overlapping meshes. [Newman et al. 2002] predicted the propeller and ship hull interaction using a RANS solver based on the multi-block approach. The propeller analysis was performed in a rotating frame of reference and the flow over the hull is performed in a fixed frame of reference. The analysis and design via optimization of a twisted rudder was also addressed, with the propeller modeled via body forces.

[Djomehri et al. 2000] used a multi-block overset grid method to simulate flow around complex aerospace configurations. They discretized the flow domain us-

ing overlapping structured grids. The solution process exchanged information on the boundaries of the blocks through interpolation.

The 3-D Euler solver [Choi 2000] has been successfully applied to compute the steady, time-averaged solution of the flow around propeller(s) represented by body forces in one single block. [Kakar 2002] used the 3-D Euler solver to predict the flow around podded propulsors, using an adaptive gridding around the pod and the strut, and by representing the propeller by body forces in one single block. In the case of propeller-rudder interaction, it is difficult to generate a single block structured grid around both the propeller and the rudder in one single block, on the other hand, it is relatively easy to generate an H-type grid around the rudder. The method described in this thesis combines a cylindrical grid in the vicinity of the propeller with an H-type grid in the vicinity of the rudder.

Chapter 3

Formulation and Numerical Implementation

The formulations for the steady, three-dimensional Euler solver and the cavitating potential flow solver are presented in this chapter. In this and the next chapter it is assumed that the rudder does not affect the propeller inflow. A method to evaluate the effect of the rudder on the propeller is presented in Chapter 5.

3.1 Euler Equations

The governing equations are the continuity equation and the x-, y-, z- momentum equations for incompressible flows. The vector form of the continuity and momentum equations for an inviscid fluid can be written as :

$$\nabla \cdot \vec{\hat{v}} = 0 \quad (3.1)$$

$$\hat{\rho} \frac{\partial \vec{\hat{v}}}{\partial \hat{t}} + \hat{\rho} \vec{\hat{v}} \cdot \nabla(\vec{\hat{v}}) = -\nabla \hat{p} + \hat{\rho} \vec{\hat{f}} \quad (3.2)$$

In equation (3.2), $\vec{\hat{v}}$ is the total velocity; $\vec{\hat{f}}$ is the body force per unit mass; $\hat{\rho}$ is the density of the fluid; \hat{p} is the pressure; and \hat{t} is the time. In the above equations, the hat ($\hat{\quad}$) indicates a dimensional variable.

The variables are made non-dimensional by a reference length which is chosen as the propeller radius R , and a reference velocity is taken as the ship speed V_s .

$$(x, y, z) = \frac{(\hat{x}, \hat{y}, \hat{z})}{R} \quad (3.3)$$

$$\vec{v} \equiv (u, v, w) = \frac{(\hat{u}, \hat{v}, \hat{w})}{V_s} \quad (3.4)$$

$$\vec{f} \equiv (f_x, f_y, f_z) = \frac{(\hat{f}_x, \hat{f}_y, \hat{f}_z)}{V_s^2/R} \quad (3.5)$$

$$t = \frac{\hat{t}}{R/V_s}, \quad p = \frac{\hat{p}}{\rho V_s^2} \quad (3.6)$$

With these dimensionless variables, the unsteady incompressible Euler equation can be rewritten as follows:

$$\nabla \cdot \vec{v} = 0 \quad (3.7)$$

$$\frac{\partial \vec{v}}{\partial t} + \vec{v} \cdot \nabla(\vec{v}) = -\nabla p + \vec{f} \quad (3.8)$$

3.2 Steady Euler Solver

The three-dimensional steady Euler solver is used to solve the flow around the propeller and other boundaries (e.g. hub or hull) in the absence of the rudder. The Euler equations are discretized using a finite volume method and the artificial compressibility method [Chorin 1967]. A ship-fixed coordinate system is used for the 3-D steady Euler solver formulation, as shown in Figure 3.1. The center of the propeller disk is considered as the origin of the coordinate system. The details of the numerical method behind the Euler solver are explained in [Choi 2000] and [Choi and Kinnas 2001].

A cartesian coordinate system is used for the three-dimensional formulation, while a cylindrical coordinate system is used in the axisymmetric formulation. In the

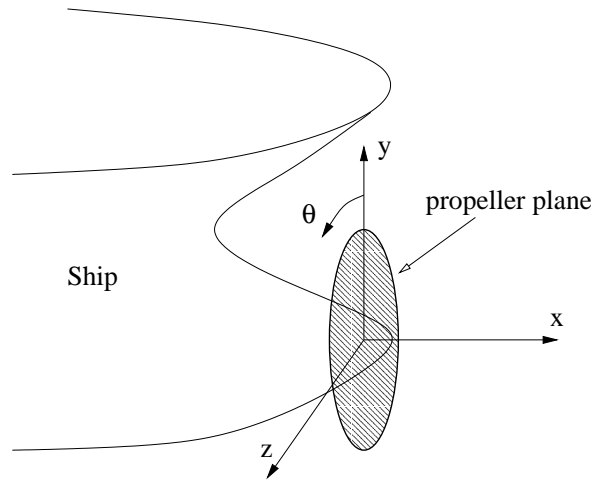


Figure 3.1: Ship-fixed Cartesian coordinate system (taken from [Choi 2000])

cartesian coordinate system, the positive y points vertically upward, and the positive z -axis points port side (left) of the ship. In a cylindrical system, the positive r is outward, and the angle θ is measured around the x -axis starting from the top (y -axis), as shown in Figure 3.1.

3.2.1 Axisymmetric Steady Euler Solver

The axisymmetric Euler solver is used to solve for flow around axisymmetric hull appendages and also in preliminary propeller design under axisymmetric (circumferentially averaged) inflow. The most advantageous characteristic of the axisymmetric Euler solver is that it takes less time to run than the three-dimensional Euler solver.

The dimensionless governing equations can be written in the cylindrical coordinate system (x, r, θ) with the corresponding velocity components (u_x, u_r, u_θ) . In the cylindrical coordinate system, the steady Euler equations can be written as follows:

$$\frac{\partial \mathbf{F}}{\partial x} + \frac{\partial \mathbf{G}}{\partial r} + \frac{\partial \mathbf{H}}{\partial \theta} = \mathbf{Q} \quad (3.9)$$

In equation (3.9), the column matrices \mathbf{F} , \mathbf{G} , \mathbf{H} , and \mathbf{Q} are defined as follows:

$$\mathbf{F} = \begin{bmatrix} ru_x \\ r(u_x^2 + p) \\ ru_x u_r \\ ru_x u_\theta \end{bmatrix}, \quad \mathbf{G} = \begin{bmatrix} ru_r \\ ru_x u_r \\ r(u_r^2 + p) \\ ru_r u_\theta \end{bmatrix},$$

$$\mathbf{H} = \begin{bmatrix} u_\theta \\ u_x u_\theta \\ u_r u_\theta \\ u_\theta^2 + p \end{bmatrix}, \quad \mathbf{Q} = \begin{bmatrix} 0 \\ rf_x \\ (u_\theta^2 + p) + rf_r \\ -u_r u_\theta + rf_\theta \end{bmatrix} \quad (3.10)$$

For the axisymmetric flow, the following assumption is also made.

$$\frac{\partial \mathbf{H}}{\partial \theta} = 0 \quad (3.11)$$

In the artificial compressibility method [Chorin 1967], the following pseudo-unsteady terms are added to the left hand side of the steady incompressible Euler equation (3.9). The purpose is to mimic the solution procedure of the unsteady compressible Euler equations.

$$\frac{\partial \mathbf{U}}{\partial t^*} \equiv \frac{\partial}{\partial t^*} \begin{bmatrix} r\tilde{\rho} \\ ru_x \\ ru_r \\ ru_\theta \end{bmatrix} \quad (3.12)$$

where, t^* is a pseudo-time which can be regarded just as an iteration parameter. Following [Chorin 1967], the artificial density, $\tilde{\rho}$, is related to the pressure, p , through the following artificial equation of state.

$$p = \frac{\tilde{\rho}}{\beta} \quad (3.13)$$

In equation (3.13), β is the artificial compressibility factor which is a controllable constant. The method requires that the artificial Mach number,

$$M = \frac{\sqrt{u_x^2 + u_r^2 + u_\theta^2}}{c}, \quad (3.14)$$

is less than 1.0, where c is the artificial speed of sound, defined as,

$$c = \frac{1}{\sqrt{\beta}}. \quad (3.15)$$

The addition of the pseudo-unsteady terms (3.12) to the steady incompressible Euler equation (3.9), with the use of equation (3.11), brings the axisymmetric governing equations to the following form.

$$\frac{\partial \mathbf{U}}{\partial t^*} + \frac{\partial \mathbf{F}}{\partial x} + \frac{\partial \mathbf{G}}{\partial r} = \mathbf{Q} \quad (3.16)$$

with

$$\mathbf{U} = \begin{bmatrix} rp \\ ru_x \\ ru_r \\ ru_\theta \end{bmatrix}, \quad \mathbf{F} = \begin{bmatrix} ru_x/\beta \\ r(u_x^2 + p) \\ ru_xu_r \\ ru_xu_\theta \end{bmatrix}, \quad \mathbf{G} = \begin{bmatrix} ru_r/\beta \\ ru_xu_r \\ r(u_r^2 + p) \\ ru_ru_\theta \end{bmatrix}, \quad (3.17)$$

$$\mathbf{Q} = \begin{bmatrix} 0 \\ rf_x \\ (u_\theta^2 + p) + rf_r \\ -u_ru_\theta + rf_\theta \end{bmatrix}$$

As the boundary conditions and body forces are steady, the solution converges to the steady state in the limit $t^* \rightarrow \infty$. When steady state is reached, the pseudo-unsteady term, $\partial \mathbf{U} / \partial t^*$, becomes zero, and equations (3.16) and (3.17) are equivalent to those of the incompressible flow. In this way, the artificial compressibility method guarantees that the steady incompressible solution is obtained at the end (i.e. at large pseudo-times).

Equation (3.16) is the final form of the governing equations to be solved by the finite volume method.

The details of the numerical implementation of the two-dimensional (i.e. axisymmetric) Euler equations (3.16) are omitted here, because they are very similar to those of the three-dimensional Euler equations given in the next section.

3.2.2 Three-dimensional Steady Euler Solver

The method of artificial compressibility [Chorin 1967] is applied again in the three-dimensional steady Euler solver. The dimensionless governing equations (3.7) and (3.8) can be written in the following three-dimensional cartesian form after introducing the pseudo-unsteady term.

$$\frac{\partial \mathbf{U}}{\partial t^*} + \frac{\partial \mathbf{F}}{\partial x} + \frac{\partial \mathbf{G}}{\partial y} + \frac{\partial \mathbf{H}}{\partial z} = \mathbf{Q} \quad (3.18)$$

The terms \mathbf{U} , \mathbf{F} , \mathbf{G} , \mathbf{H} , and \mathbf{Q} are defined as follows.

$$\mathbf{U} = \begin{bmatrix} p \\ u \\ v \\ w \end{bmatrix}, \quad \mathbf{F} = \begin{bmatrix} u/\beta \\ u^2 + p \\ uv \\ uw \end{bmatrix}, \quad \mathbf{G} = \begin{bmatrix} v/\beta \\ uv \\ v^2 + p \\ vw \end{bmatrix}, \quad \mathbf{H} = \begin{bmatrix} w/\beta \\ uw \\ vw \\ w^2 + p \end{bmatrix}, \quad (3.19)$$

$$\mathbf{Q} = \begin{bmatrix} 0 \\ f_x \\ f_y \\ f_z \end{bmatrix}$$

The first term in equation (3.18) vanishes when the steady state is reached and the incompressible steady flow solution is obtained.

For the finite volume formulation, the Euler equations (3.18) are integrated over a cell of volume \mathcal{V} . With the use of the divergence theorem, the integral form of the

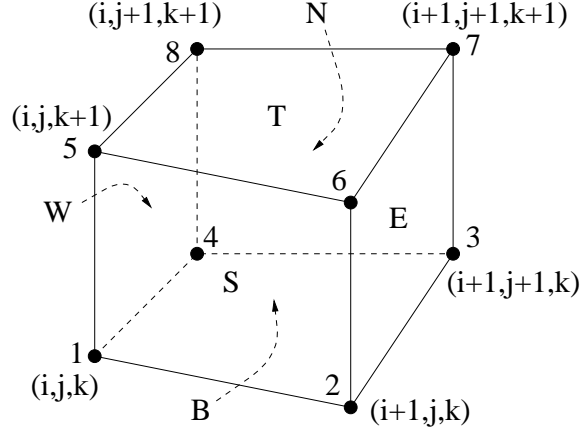


Figure 3.2: Cell (i, j, k) on which the finite volume method is applied (taken from [Choi 2000])

Euler equation can be written as follows.

$$\frac{\partial}{\partial t} \iiint_V \mathbf{U} dV + \iint_S (\mathbf{F}n_x + \mathbf{G}n_y + \mathbf{H}n_z) dS = \iiint_V \mathbf{Q} dV \quad (3.20)$$

The fluid domain is discretized into hexahedral cells, as shown in Figure 3.2. The unit surface normal vector, \vec{n} , with components (n_x, n_y, n_z) , points in the outward direction from the cell.

The semi-discrete equation in which space is discretized can be written as follows for each cell.

$$\frac{\partial \mathbf{U}_{(i,j,k)}}{\partial t} V_{(i,j,k)} + \sum_{faces} (\mathbf{F}A_x + \mathbf{G}A_y + \mathbf{H}A_z) = \mathbf{Q}_{(i,j,k)} V_{(i,j,k)} \quad (3.21)$$

where, $V_{(i,j,k)}$ is the volume of the cell (i, j, k) , and (A_x, A_y, A_z) are the projections of the area of each face along the (x, y, z) directions, respectively.

The vertex based scheme is used in the present method, in which all variables in \mathbf{U} are stored at the nodes, 1, 2, 3, \dots , 8 as shown in Figure 3.2.

For the time discretization, Ni's Lax-Wendroff method [Ni 1982] is applied. That is, the variable \mathbf{U} at a particular node, at the next time (pseudo-time) step $n + 1$, is

approximated by the following second order difference.

$$\mathbf{U}_{(i,j,k)}^{n+1} \simeq \mathbf{U}_{(i,j,k)}^n + \left(\frac{\partial \mathbf{U}}{\partial t} \right)_{(i,j,k)}^n \Delta t + \left(\frac{\partial^2 \mathbf{U}}{\partial t^2} \right)_{(i,j,k)}^n \frac{(\Delta t)^2}{2} \quad (3.22)$$

where, Δt is the time step size, and the superscript n represents the value of the current time step. The first order term, $\partial \mathbf{U} / \partial t$, at each node is approximated by the average of its values at the neighboring cells, where the value at each cell is expressed using the discretized governing equation (3.21).

$$\left(\frac{\partial \mathbf{U}}{\partial t} \right)_{(i,j,k)}^n \simeq \frac{1}{8} \sum_{cell_s} \left(\frac{\partial \mathbf{U}}{\partial t} \right)_{cell}^n \quad (3.23)$$

Similarly, the second order term is also approximated with the average from the neighbouring cells [Choi 2000].

The artificial dissipation (or viscosity) is applied to improve the stability of the numerical method [Anderson 1995]. The second and fourth order dissipations, respectively μ_2 and μ_4 , are scaled by Δt and added to the right hand side of equation 3.22.

$$\mu_2 = \sigma_2 (\delta_{ii} \mathbf{U}_{(i,j,k)}^n + \delta_{jj} \mathbf{U}_{(i,j,k)}^n + \delta_{kk} \mathbf{U}_{(i,j,k)}^n) \quad (3.24)$$

$$\mu_4 = \sigma_4 (\delta_{iiii} \mathbf{U}_{(i,j,k)}^n + \delta_{jjjj} \mathbf{U}_{(i,j,k)}^n + \delta_{kkkk} \mathbf{U}_{(i,j,k)}^n) \quad (3.25)$$

where, the artificial dissipation coefficients, σ_2 and σ_4 , are user specified constant parameters that control the amount of the dissipation.

The finite central difference operators, δ_{ii} and δ_{iiii} , for example, are defined as follows.

$$\delta_{ii} = ()_{i-1} - 2()_i + ()_{i+1} \quad (3.26)$$

$$\delta_{iii} = (\)_{i-2} - 4(\)_{i-1} + 6(\)_i - 4(\)_{i+1} + (\)_{i+2} \quad (3.27)$$

The time step size is determined based on the CFL condition [Courant et al. 1967]

$$\Delta t < \min_{i,j,k} \left\{ \min \left(\frac{\Delta x}{u}, \frac{\Delta y}{v}, \frac{\Delta z}{w} \right) \right\} \quad (3.28)$$

The iteration in time is continued until the maximum change of variables is less than a certain tolerance.

For most of the cases presented in this thesis, the second order dissipation coefficient, σ_2 , is set equal to zero. The fourth order artificial dissipation coefficient, σ_4 , is determined by trial and error so that it has the smallest required value for the Euler solver to converge.

A special treatment of the artificial dissipation terms in the case of applying the Euler code on a rudder is described in Section 5.2.1. The steady 3-D Euler code is called GBFLOW-3D and its latest version can handle hull or tunnel boundaries, contra-rotating propellers, stator-rotor combinations, ducted and podded propulsors [Gu et al. 2003].

3.2.3 Boundary Conditions

In the three-dimensional Euler solver there are six boundaries, as shown in Figure 3.3: (a) the upstream boundary where the flow comes in, (b) the downstream boundary where the flow goes out, (c) the hull boundary at the top, (d) the outer boundary at the far field (or the wall boundaries in the case of bounded flow), (e) the shaft (hub) or center line boundary, and (f) the periodic boundary which connects the be-

ginning and the end of indices along the circumferential direction. It should be noted that even though the rudder is shown in Figure 3.3, its boundary is not gridded. As mentioned earlier, in this section we only address the flow around the propeller and the other boundaries, in the *absence* of the rudder.

The applied boundary conditions are shown in the Figure 3.3. The top boundary is treated as a hull, while the side and bottom boundaries are treated as either solid boundaries or far-stream boundaries (in which case they must be located farther from the propeller than shown in the Figure 3.4). In the case of flow inside a tunnel, the side and bottom boundaries are also treated as solid boundaries as described later in this section. In the case of unbounded flow under the hull (more appropriate for full scale calculations), the side and bottom boundaries are treated as far-stream boundaries.

The boundary conditions applied in the present method are summarized next.

- Upstream boundary:

The velocities are set equal to the given values, and the first derivative of the pressure with respect to the axial direction is taken equal to zero.

$$(u, v, w) = (u, v, w)_{given} \quad (3.29)$$

$$\frac{\partial p}{\partial n} = \frac{\partial p}{\partial x} = 0 \quad (3.30)$$

where, $(u, v, w)_{given}$ are the components of uniform inflow or the *nominal wake components* in the case of a propeller problem.

- Downstream boundary:

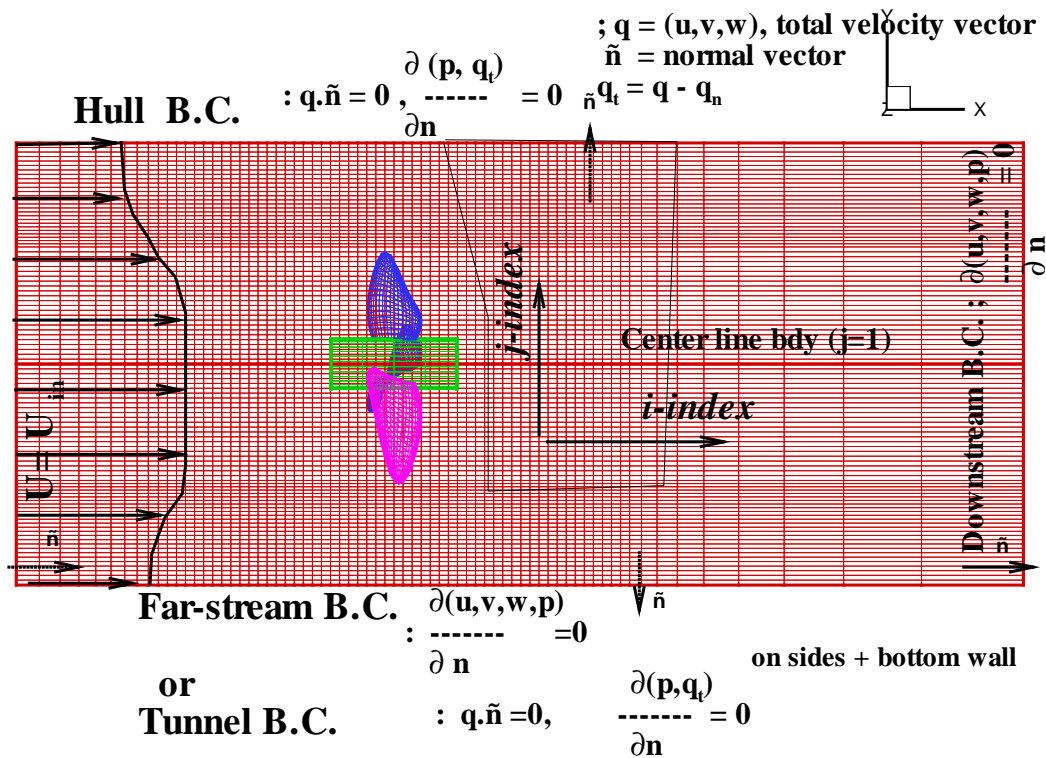


Figure 3.3: Boundary conditions for the Euler solver which evaluates the propeller induced inflow to the rudder

The derivatives of all the velocity components and the pressure with respect to the axial direction are taken equal to zero.

$$\frac{\partial(u, v, w, p)}{\partial n} = \frac{\partial(u, v, w, p)}{\partial x} = 0 \quad (3.31)$$

- Center line boundary ($j=1$ line in the grid):

In the case of the axisymmetric solver, the first derivative of the axial velocity along the radial direction is taken equal to zero. The tangential and radial components are taken equal to zero. In the case of the three-dimensional solver, the values of the velocities and pressures at the center boundary ($j = 1$) are taken equal to the average of the values at ($j = 2$).

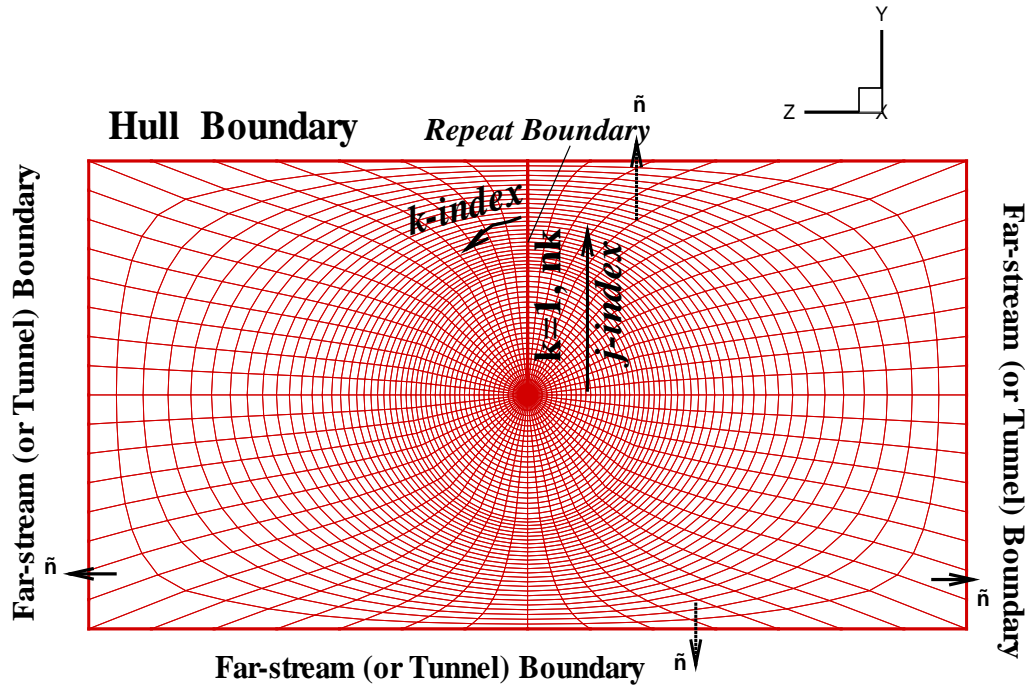


Figure 3.4: Boundary conditions on the domain (shown at an axial location)

- In the axisymmetric solver (j is the index in the radial direction),

$$(u_x, p)_{j=1} = (u_x, p)_{j=2} \quad (3.32)$$

$$u_r = u_\theta = 0 \quad (\text{at } j = 1) \quad (3.33)$$

- In the three-dimensional solver,

$$(u, v, w, p)_{(i,1,k)} = \frac{1}{N_k} \sum_{k=1, N_k} (u, v, w, p)_{(i,2,k)} \quad (3.34)$$

where, N_k is the number of nodes in the circumferential direction.

- Far-stream boundary :

The derivatives of the velocity components and the pressure along the normal direction at the boundary are taken equal to zero.

$$\frac{\partial(u, v, w, p)}{\partial n} = 0 \quad (3.35)$$

$$(3.36)$$

- Hull boundary (free slip):

The normal component of the velocity is set equal to zero, and the derivatives of the other velocity components and the pressure with respect to the direction normal to the hull are taken equal to zero.

$$\frac{\partial(p)}{\partial n} = 0 \quad (3.37)$$

$$\vec{q} \cdot \vec{n} = 0 \quad (3.38)$$

$$\vec{q} = \vec{q}_t + \vec{q}_n \quad (3.39)$$

$$\frac{\partial(\vec{q}_t)}{\partial n} = 0 \quad (3.40)$$

where, \vec{q} is the total velocity, $q = (u, v, w)$, \vec{q}_t is the component of the total velocity along the tangential direction, \vec{q}_n is the component of the total velocity along the normal direction.

- Periodic or Repeat boundary as shown in Figure 3.4 (three-dimensional problem only):

$$(u, v, w, p)_{k=1} = (u, v, w, p)_{k=N_k} \quad (3.41)$$

where k is the index along the circumferential direction.

3.3 Potential Flow Solver

3.3.1 Boundary Element Method

In this section a 3-D potential based BEM is used for the numerical modeling of the cavitating flow around a rudder. The performance characteristics of the rudder are mostly affected by the ship hull geometry and the propeller action. The flow induced by the propeller is determined through GBFLOW-3D coupled with MPUF-3A. This is under the assumption that the effect of the rudder on the propeller inflow is negligible. In the case of a rudder operating close to the propeller, this assumption is not valid. This case will be discussed in Chapter 5.

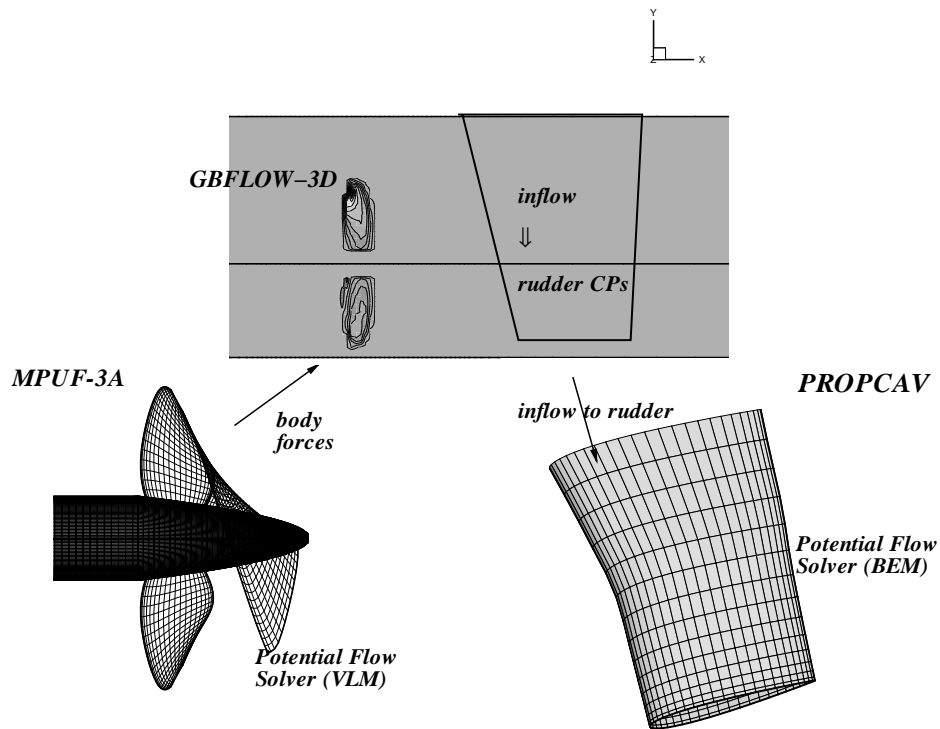


Figure 3.5: Potential flow around a cavitating rudder subject to the propeller induced flow

The propeller is represented by body forces predicted by MPUF-3A [Lee et al.

2003]. Once the iterations between GBFLOW-3D and MPUF-3A have converged, the total flow field induced by the propeller is computed at the rudder control points.

The rudder is treated as a 3-D cavitating hydrofoil using PROPCAV. In PROPCAV, a Fredholm integral equation of the second kind is solved for the perturbation potential. A Dirichlet type boundary condition is applied on the cavitating surfaces and a Neumann type boundary condition is applied on the wetted surface of the hydrofoil. The cavity surface is determined in an iterative manner until both the prescribed pressure on the cavity surface and the flow tangency conditions are satisfied on the cavity.

Formulation of Potential flow around a Cavitating Rudder

Consider the cavitating flow over the rudder, as shown in Fig. 3.6, subject to a general inflow \vec{U}_{in} which is induced by the propeller. We consider steady flow, i.e. \vec{U}_{in} is only a function of space, and is determined as described in the beginning of this section. Assuming that the flow around the rudder is incompressible, inviscid and irrotational, the time dependent perturbation potential, $\phi(x, y, z, t)$, can be expressed as follows:

$$\vec{q}(x, y, z, t) = \vec{U}_{in}(x, y, z) + \nabla\phi(x, y, z, t) \quad (3.42)$$

The governing equation everywhere inside the fluid region is given by:[Kinnas and Fine 1993a; Mueller and Kinnas 1999]

$$\nabla^2\phi = 0; \text{ inside the fluid domain} \quad (3.43)$$

The perturbation potential on the combined foil and cavity surface, as shown in Figure 3.6 satisfies the following integral equation obtained from Green's third identity:

$$2\pi\phi_p = \int_{S_B} \left[\phi_q \frac{\partial G(p; q)}{\partial n_q} - G(p; q) \frac{\partial \phi_q}{\partial n_q} \right] dS + \int_{S_W} \Delta\phi_W \frac{\partial G(p; q)}{\partial n_q} dS \quad (3.44)$$

where p , and the point of integration q corresponds to the variable point in the integration. As shown in Figure 3.6, S_B is the foil and cavity surface, S_W is the trailing wake surface, $G(p; q) = 1/R$ is the Green's function, $R(p; q)$ is the distance between the points p and q , and \vec{n}_q is the normal vector over the foil surface S_B and S_W . $\Delta\phi_W$ is the potential jump across the wake surface, S_W . The integration over the foil surface, S_B includes the cavitating portion of the foil surface S_{CB} and wetted portion of the foil surface S_{WB} .

The above integral equation is discretized using quadrilateral panels with constant strength dipoles and sources distributed over the rudder and cavity surface. In the present method the wake surface, S_W , is taken to be aligned with the ship speed. The unknowns, ϕ on the wetted foil, and $\partial\phi/\partial n$ on the cavity, are determined by inverting equation 3.44. Once the unknowns are determined the cavity thickness, $h(s, v)$, can be determined from solving the partial differential equation 3.57, [Kinnas and Fine 1993a].

- *Kinematic Boundary Condition on Non-cavitating (Wetted) surface*

The kinematic boundary condition, which is applied on the wetted portion of the foil surface, requires the flow to be tangent to the wetted blade. Thus, the source strengths, $\frac{\partial\phi}{\partial n}$, are known in terms of the inflow velocity, \vec{U}_{in} .

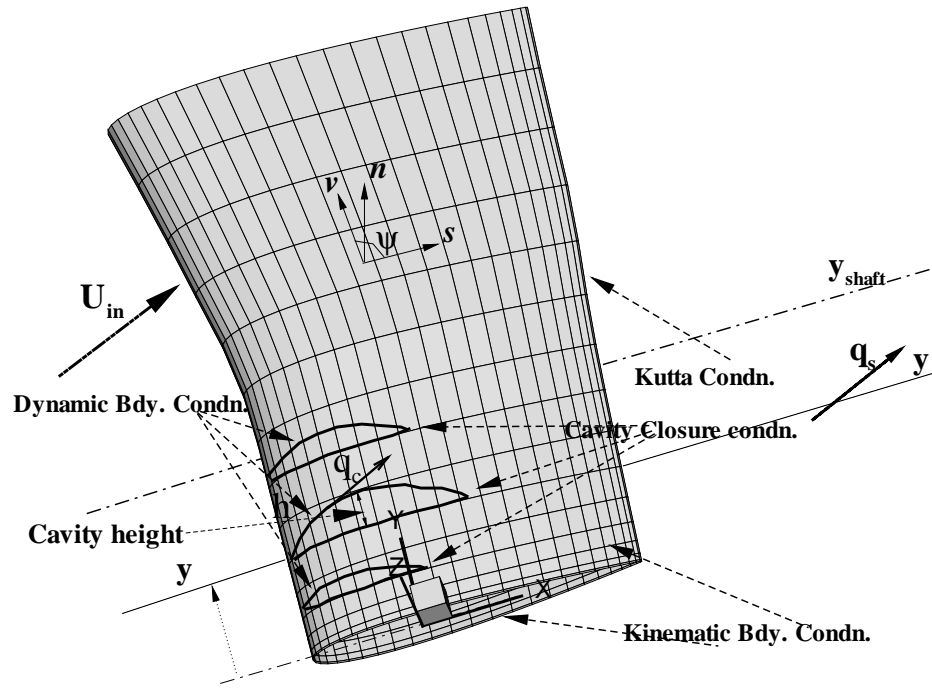


Figure 3.6: Rudder with partial cavity and the required physical conditions

$$\frac{\partial \phi}{\partial n} = -\vec{U}_{in} \cdot \vec{n} \quad (3.45)$$

where \vec{n} is the normal vector on the foil surface pointing into the fluid, as shown in Figure 3.6.

- *Kutta Condition*

The Kutta condition requires that the velocity at the trailing edge of the rudder (T.E.) to be finite.

$$\nabla \phi \text{ is finite at T.E.} \quad (3.46)$$

The Kutta condition could be enforced numerically by applying the Morino condition [Morino and Kuo 1974], which requires the difference of the potentials at the two sides of the trailing edge to be equal to the potential jump in the wake. Instead, an improved iterative pressure Kutta condition [Kinnas and Hsin 1992] is applied, which modifies the difference of potentials at the two sides of the trailing edge, to achieve equality of pressures at both sides of the T.E. everywhere along the span of the rudder [Young and Kinnas 2001].

- *Dynamic Boundary Condition on Cavitating Surfaces*

The dynamic boundary condition requires the pressure on the cavity to be constant and equal to the vapor pressure, p_v . To express the dynamic boundary conditions in terms of the flow velocities we apply the Bernoulli equation between a point on the cavity surface with a vertical coordinate y (on which the pressure is p_v and the velocity magnitude q_c) and a point with a vertical coordinate y_s far downstream¹ along the same streamline where the velocity magnitude is q_s and the pressure p_s :

$$p_v + \frac{\rho}{2}q_c^2 + \rho gy = p_s + \frac{\rho}{2}q_s^2 + \rho gy_s \quad (3.47)$$

Assuming that the pressure variation far downstream is practically hydrostatic, as this is verified by the small variation of the pressures predicted by GBFLOW-3D² far downstream, we get:

¹The Bernoulli equation cannot be applied between points on the rudder which are inside the propeller slipstream and points upstream of the propeller, due to the pressure jump across the propeller plane.

²The pressures in GBFLOW-3D do not include the hydrostatic pressure and are made non-dimensional with respect to ρV_s^2 . Example of the magnitude of pressure variations can be seen in Figure 4.29

$$p_v + \frac{\rho}{2}q_c^2 + \rho gy = p_{shaft} + \frac{\rho}{2}q_s^2 + \rho gy_{shaft} \quad (3.48)$$

where p_{shaft} is the absolute pressure at the propeller shaft axis and y_{shaft} is the vertical coordinate of the shaft axis.

Non-dimensionalising the equation through $\frac{\rho}{2}V_s^2$, the total constant velocity over the cavity is defined as follows:

$$q_c = V_s \sqrt{\left(\frac{q_s}{V_s}\right)^2 + \sigma(y)} \quad (3.49)$$

where the *local cavitation number* $\sigma(y)$, which depends on the vertical coordinate y , is defined as:

$$\sigma(y) = \sigma_R - 2g \frac{y - y_{shaft}}{V_s^2} \quad (3.50)$$

and the rudder cavitation number σ_R is,

$$\sigma_R = \frac{p_{shaft} - p_v}{\frac{\rho}{2}V_s^2} \quad (3.51)$$

In determining the value of q_c , as given by equation 3.49, q_s is also assumed to be equal to the magnitude of \vec{U}_{in} , the inflow velocity in the absence of the rudder. This implies that the rudder is past the contraction region in the propeller slipstream.

The following expression for $\frac{\partial \phi}{\partial s}$, where s is the curvilinear coordinate along the chordwise direction, is valid [Kinnas and Fine 1993a]:

$$\frac{\partial \phi}{\partial s} = -\vec{U}_{in} \cdot \vec{s} + V_v \cos \psi + \sin \psi \sqrt{q_c^2 - V_v^2} \quad (3.52)$$

where $V_v \equiv \frac{\partial \phi}{\partial v} + \vec{U}_{in} \cdot \vec{v}$; \vec{s} and \vec{v} are the local unit vectors in the chord-wise and span-wise direction, respectively. ψ is the angle between \vec{s} and \vec{v} , as shown in Figure

3.6. Equation 3.52 is integrated along s to provide us with the value of ϕ over the cavity surface [Kinnas and Fine 1993a].

- *Hydrostatic Effects*

The hydrostatic effects on the rudder as it appears on the equation 3.50, are introduced through Froude number which has been defined as shown below:

$$Fr_{rudder} = V_s^2 / (g * Span) \quad (3.53)$$

The Froude number for the flow over the rudder in the influence of propeller, is related to the Froude number, F_n and the advance ratio, J_s of the propeller as follows:

$$F_n = n^2 D / g \quad (3.54)$$

$$J_s = V_s / nD \quad (3.55)$$

$$Fr_{rudder} = J_s^2 * F_n * D_{prop} / Span \quad (3.56)$$

- *Cavity Detachment Criterion*

The algorithms to determine the cavity detachment on the suction and/or the pressure side of the rudder have been developed in [Mueller and Kinnas 1999; Young and Kinnas 2003b]. The iterative search algorithm is performed at each strip along the spanwise direction, by beginning at the leading edge and marching downstream towards the section trailing edge along each strip. The cavity detachment is adjusted iteratively until the *smooth detachment condition* [Young 2002] is satisfied:

1. Non-negative thickness at the cavity leading edge .

2. The pressure on the wetted portion of the rudder upstream of the cavity should be greater than the vapor pressure $P_{\text{upstream of cavity}} > P_v$.

- *Determining the Cavity Height*

Once the unknowns are determined the cavity height $h(s, v)$ can be determined by solving the following partial differential equation.

$$\frac{\partial h}{\partial s} [V_s - \cos \psi V_v] + \frac{\partial h}{\partial v} [V_v - \cos \psi V_s] = V_n \sin^2 \psi \quad (3.57)$$

where $V_s \equiv \frac{\partial \phi}{\partial s} + \vec{U}_{in} \cdot \vec{s}$ and $V_n \equiv \frac{\partial \phi}{\partial n} + \vec{U}_{in} \cdot \vec{n}$ are the tangential and the normal component of the total velocity vector, respectively.

- *Cavity Closure Condition*

The extent of the unknown cavity surface is determined as part of the solution. For a given cavitation number, σ_R , the cavity height at the trailing edge of the cavity is required to be equal to 0 (i.e. cavity closes at its trailing edge). This is the basis of the iterative solution method that is used to find the cavity planform [Mueller and Kinnas 1999]. As shown in [Kinnas and Fine 1993a] this condition provides us with an algorithm for determining the cavity length at each location along the rudder span.

- *Hull Effects on Rudder*

In PROPCAV, the effect of a flat hull on top of the rudder is considered by using an image model. Based on the conventional image models, the image of the rudder with

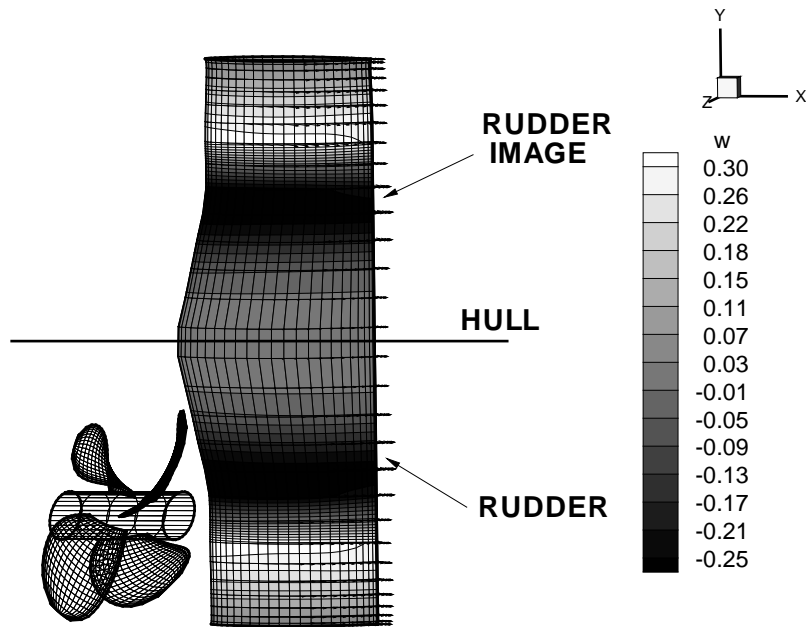


Figure 3.7: Rudder with the inflow mirrored with respect to the hull

respect to the hull is represented by sources and dipoles along with the rudder. This is achieved by physically modeling the image of the rudder through panels. Then the flow field over the rudder induced by the propeller is also imaged with respect to the hull, as shown in Figure 3.7.

The disadvantage with the above technique is that it requires the image of the rudder with respect to the hull to also be physically modeled through panels. This requires an additional memory capacity for the storage of influence coefficients, and a considerable increase in the computational effort to solve the system of matrices. Therefore, an alternative technique was adopted, as shown in Figure 3.8, in which the influence due to the image panels of the rudder and the wake are included through the influence coefficients on the rudder control points. The advantage of this technique is that only the rudder is considered for the computation, thus reducing the

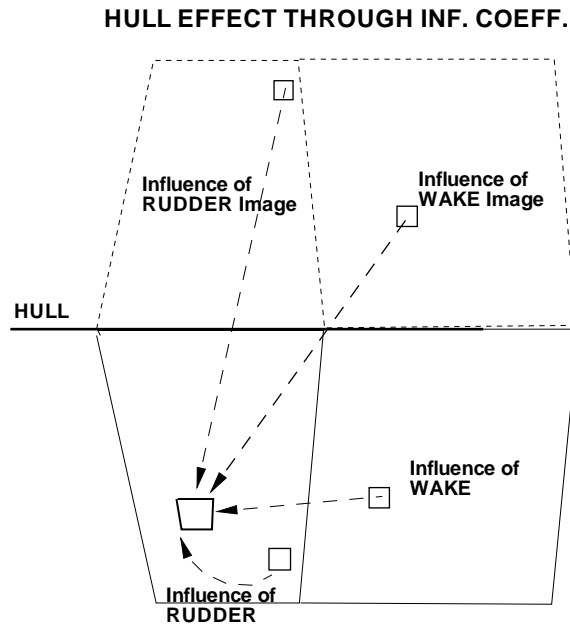


Figure 3.8: Rudder with the influence from the images with respect to the hull

computer memory and the required computational effort.

3.3.2 Vortex-Lattice Method

This section presents an overview of the vortex-lattice method based potential flow solver which is used for the analysis of the cavitating propeller flow. The complete formulation of the potential flow solver and the vortex lattice method may be found in chapter 6 by Kinnas in [Ohkusu 1996].

The *vortex-lattice method* which solves for the unsteady potential flow field around a cavitating propeller has been used successfully since the method was first developed by Kerwin and Lee [Kerwin and Lee 1978], Lee [Lee 1979] and Breslin et. al. [Breslin et al. 1982].

In the vortex-lattice method, a special arrangement of line vortex and source lattice is placed on the blade mean camber surface and its trailing wake surface. There are three types of singularities:

(a) the vortex lattice on the blade mean camber surface and the trailing wake surface which represents the blade loading and the trailing vorticity in the wake,

(b) the source lattice on the blade mean camber surface which represents the blade thickness, and

(c) the source lattice throughout the predicted sheet cavity domain which represents the cavity thickness.

This method is classified as a lifting surface method because the singularities (vortices and sources) are distributed on the blade mean camber surface, as opposed to the other class of methods, the surface panel methods, in which the singularities are distributed on both sides of the blade surface.

The unknown strengths of the singularities are determined so that the kinematic and the dynamic boundary conditions are satisfied at the control points on the blade mean camber surface.

The *Kinematic Boundary Condition* requires that the flow velocity is tangent to the mean camber surface, and is applied at all control points.

The *Dynamic Boundary Condition* requires that the pressure on the cavitating part of the blade mean camber surface is equal to the vapor pressure, and is applied only at the control points that are in the cavitating region.

Chapter 4

Convergence and Validation Studies

This chapter discusses the application of the low-order potential based Boundary Element Method (PROPCAV) to the problem of flow over a rudder under the influence of a propeller. The motivation for studying this problem without considering the propeller-rudder interaction is to understand the performance of the rudder with the vortical flow induced by the propeller. Results of extensive validation tests and convergence studies for a horn-type rudder are presented in the first section. Comparisons of cavity patterns predicted over a horn-type rudder with the cavity patterns observed in an experiment conducted at a cavitation tunnel are also presented in this section. Next, the PROPCAV is extended to the problem of a flapped rudder. The present model panels, the entire rudder section including the flap. In practice, a gap exists between the immovable component of the rudder and the flap. The developed model considers that the gap between the rudder and the flap is hydrodynamically sealed. Convergence studies for a rudder with flap angle is $\alpha_{flap} = 10^\circ$ are presented in this section. The performance of the flapped rudder with various flap angles is also presented. Finally, PROPCAV applied on a twisted rudder.

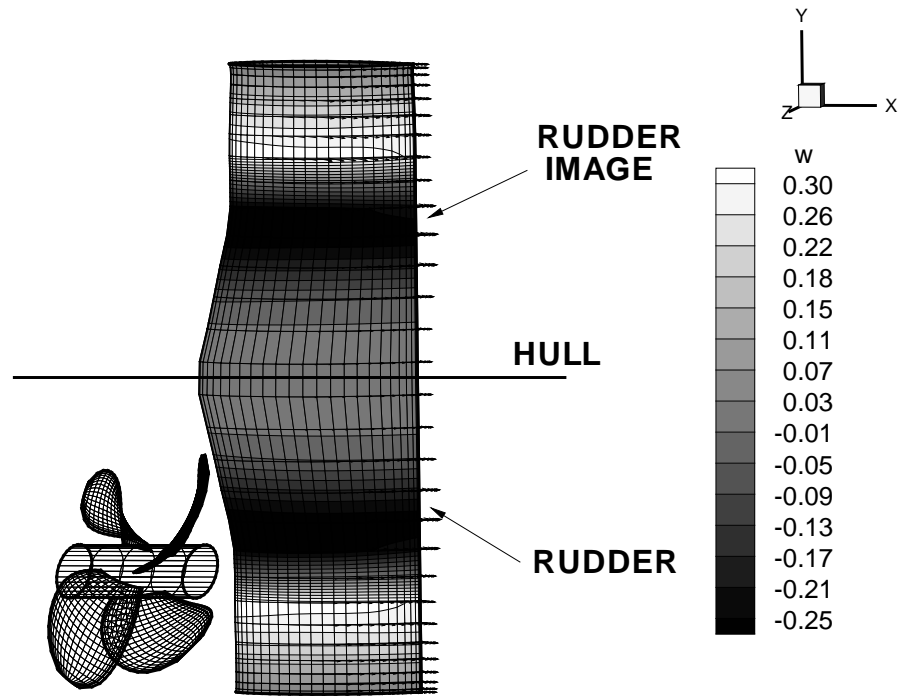


Figure 4.1: Rudder with the inflow mirrored with respect to the hull

4.1 Rudder with Image model

In this section, results obtained for a horn-type rudder modeled using PROPCAV are presented. The effect of the hull is introduced by considering the rudder with its image as a new hydrofoil, and by also mirroring the inflow with respect to the hull, as shown in Figure 4.1. The objective of performing this study is to examine the convergence of the method using the *DTMB 4497* propeller at an advance ratio, $J_s = 0.96$.

Propeller-tunnel interaction is accounted for through an iterative run between MPUF-3A and GBFLOW-3D. The iterative process starts using the uniform inflow for the propeller analysis in MPUF-3A. Using the computed propeller loading, the body

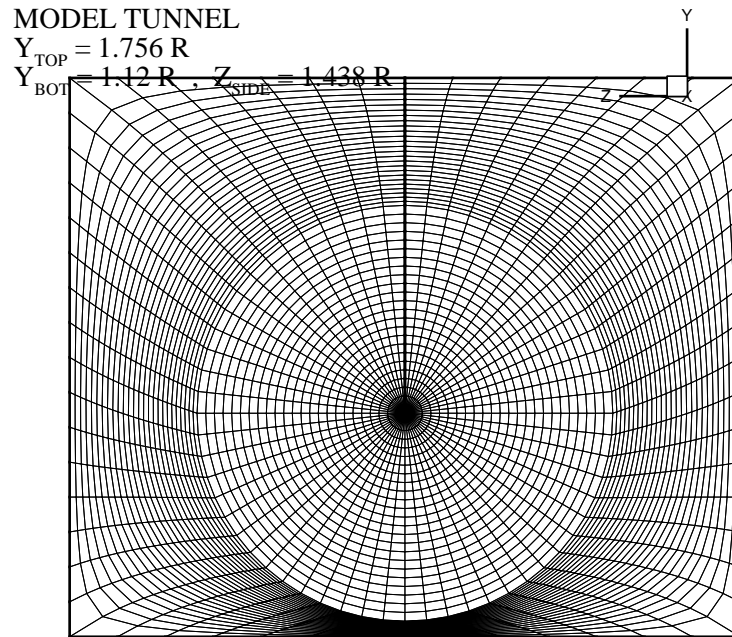


Figure 4.2: Cylindrical grid at the inflow plane of the tunnel

force representing the propeller is calculated. GBFLOW-3D computes the total velocity field using the body force found earlier. The effective wake can then be computed by subtracting the propeller induced velocity from the total velocity field. MPUF-3A uses the predicted effective wake as inflow to compute the updated propeller loading. The iterative process continues until convergence is reached. The cylindrical grid used in the GBFLOW-3D at the inflow plane is shown in Figure 4.2. Figure 4.3 shows the flow field induced by the propeller with the effects of a tunnel walls included.

4.1.1 Convergence Studies

Convergence studies are performed for PROPCAV applied to a rudder and its image. The two important parameters in this problem are the number of panels along

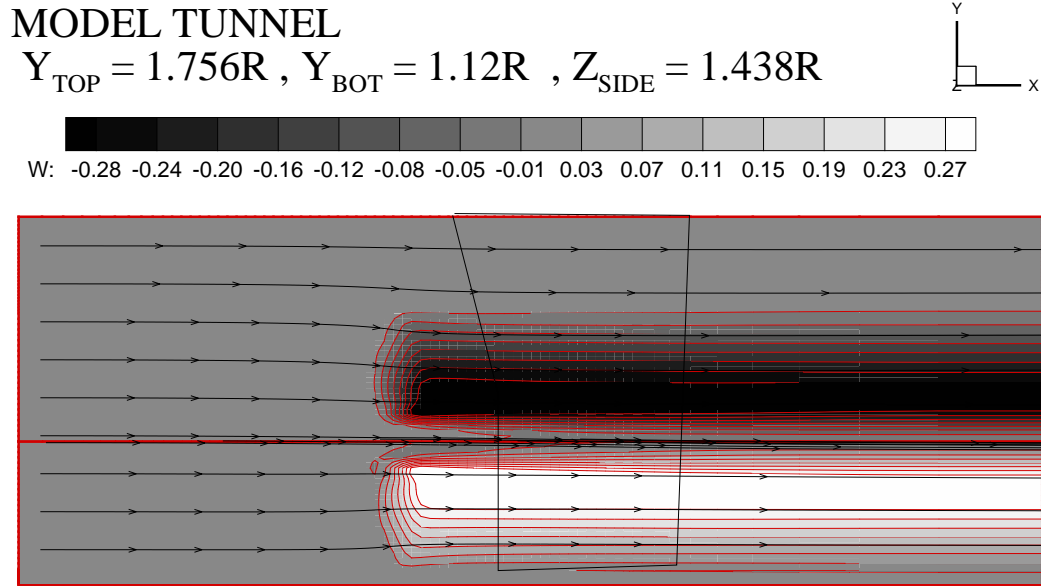


Figure 4.3: Solution at the center plane of the domain obtained from the 3-D Euler solver, including the tunnel wall effects

the chordwise and the spanwise directions. These studies help in ascertaining appropriate values of input parameters, which can achieve expected level of accuracy with minimum run time. The rates of convergence have not been determined for this particular case. Details regarding the convergence rates for cavitating hydrofoils and propellers can be found in [Young and Kinnas 2003a] . The circulation distribution on the rudder is a measure of the lift provided by the rudder. Hence, the convergence studies are performed on both the circulation and pressure distributions over the rudder.

Figures 4.4 and 4.5 show the convergence of the circulation distribution obtained from PROPCAV, with varying chordwise panels and spanwise panels respectively. A full-cosine spacing along the chordwise direction and a uniform spacing along the spanwise direction are used. The circulation distribution is shown along the span

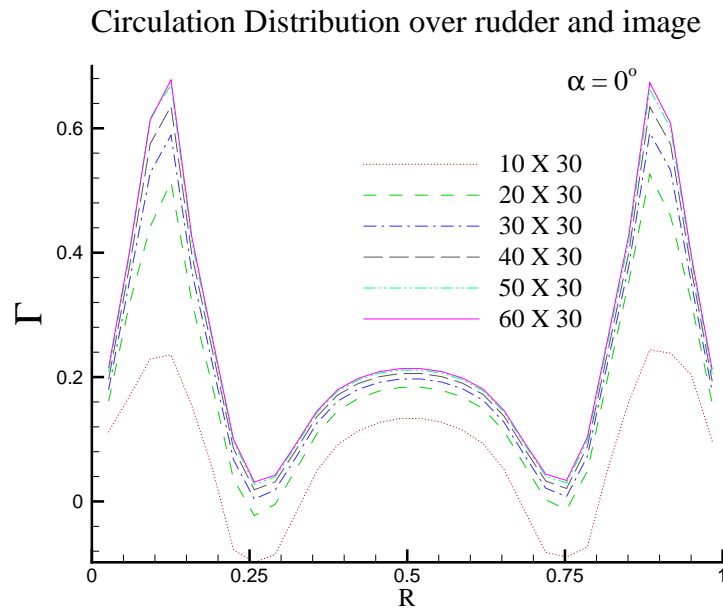


Figure 4.4: Convergence of circulation with number of panels in the chordwise direction. $R = 0$ is the lower tip and $R = 0.5$ is the upper tip of the rudder (close to the hull)

of the rudder and its image with respect to hull. The circulation is symmetric with respect to $R = 0.5$, which is the upper tip of the rudder (close to the hull). The convergence of the pressure distribution at a strip located at $y/R = 0.34$ is shown in Figure 4.6. The convergence of the cavitation volume is shown in Figure 4.7.

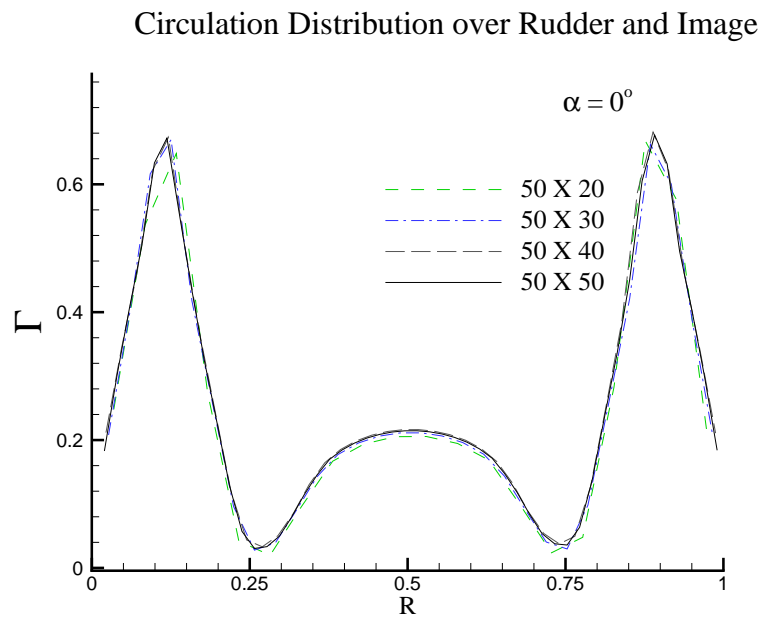


Figure 4.5: Convergence of circulation with number of panels in the spanwise direction. $R = 0$ is the lower tip and $R = 0.5$ is the upper tip of the rudder (close to the hull)

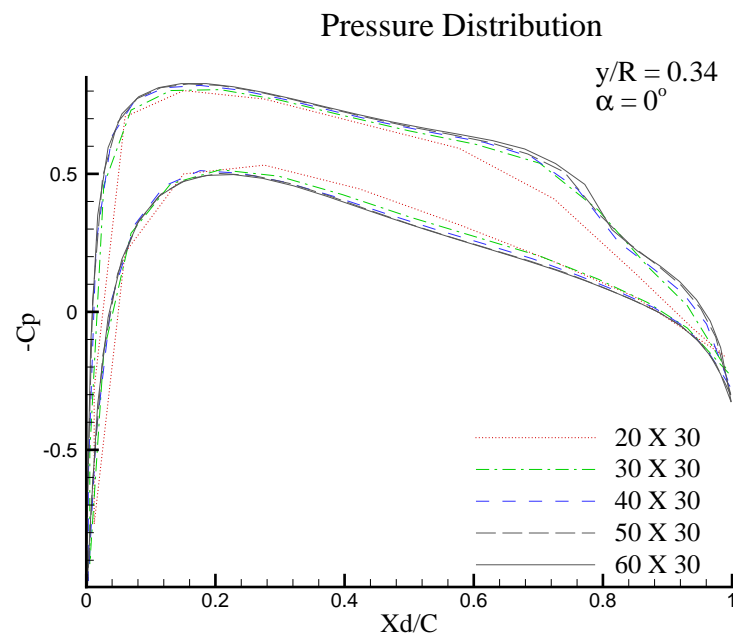


Figure 4.6: Convergence of pressure distribution along the strip at $y/R = 0.34$

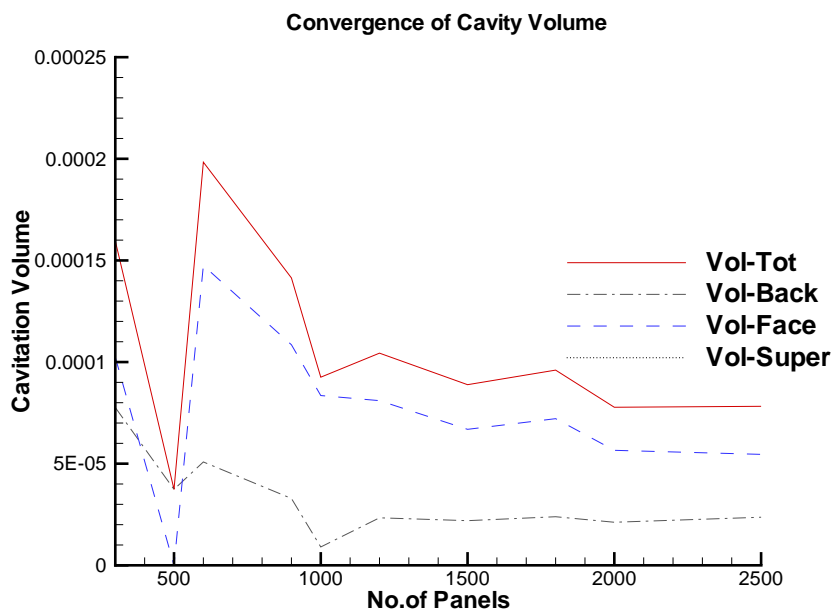


Figure 4.7: Convergence of cavitation volume with total number of panels

4.2 Validation for the Elliptic Wing

The predictions of PROPCAV in the case of non-cavitating flows are validated with the classical analytical solutions for elliptically loaded wings.

According to the lifting line theory, for an elliptic wing the lift coefficient, C_L , is given as,

$$C_L = \frac{2\pi\alpha}{1 + \frac{2}{AR}} \quad (4.1)$$

where α is the angle of attack of the section and AR is the aspect ratio defined as the ratio of square of the span by the planform area of the wing. For elliptic wings:

$$AR = \frac{4S}{\pi l_o} \quad (4.2)$$

where S is the span and l_o is the maximum chord of the elliptic wing, as shown in Figure 4.8. The circulation distribution over the elliptic wing has the classical elliptic loading:

$$\Gamma = \Gamma_o \sqrt{1 - 4\frac{z^2}{S^2}} \quad (4.3)$$

PROPCAV is applied to half span of the wing with the effect of the other half being included through images of the influence coefficients, as described in Section 3.3.1. In Figure 4.9, the predicted loading and the theoretical circulations are compared. In Figure 4.10, the lift coefficients predicted from PROPCAV are compared with the analytical values for various aspect ratios at a fixed angle of attack of $\alpha = 2^\circ$. Lift and drag coefficients are also compared for various angles of attack in Figure 4.11 at a particular aspect ratio of $AR = 12.5$. The PROPCAV predictions shown in the previous figures match the analytical values very well.

ELLIPTIC WING

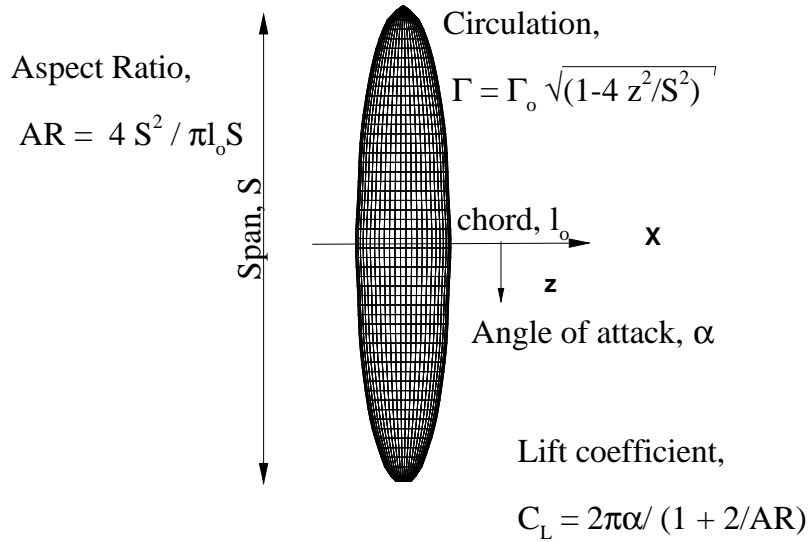


Figure 4.8: The elliptic planform wing with an elliptic cross-section of 0.0125 thickness to chord ratio, used in the validation of PROPCAV in wetted flow.

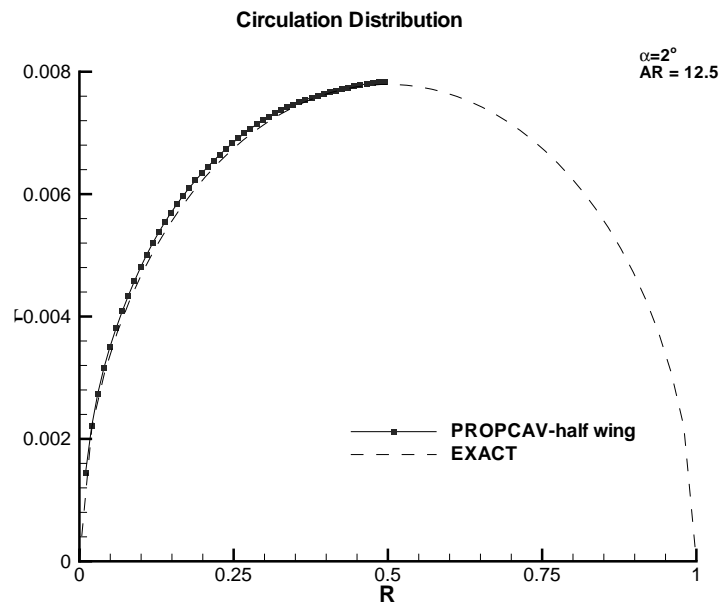


Figure 4.9: Circulation distribution predicted by PROPCAV and analytical, for an elliptic wing

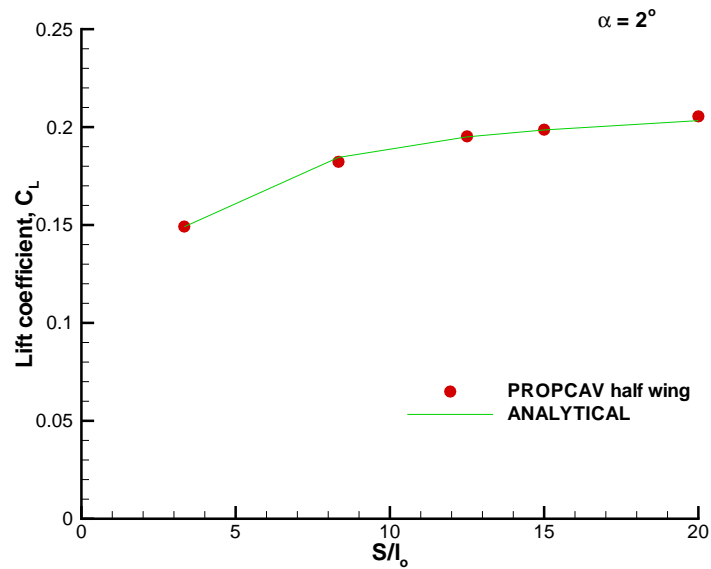


Figure 4.10: Lift coefficients, predicted by PROPCAV and analytical, for an elliptic wing at various ratios

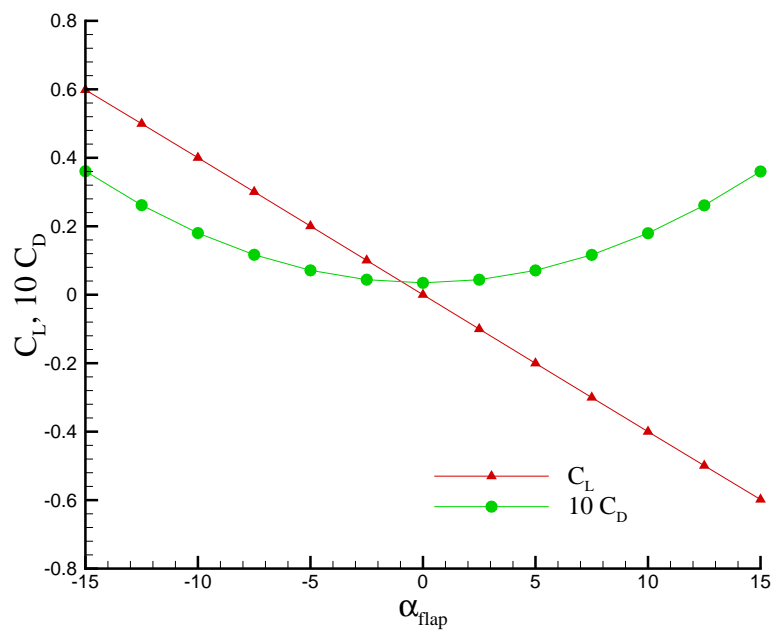


Figure 4.11: Lift and drag coefficients, predicted by PROPCAV and analytical, for an elliptic wing at various angles of attack

HULL ON TOP

$$Y_{\text{TOP}} = 1.756 R$$
$$Y_{\text{BOT}} = -1.756 R, Z_{\text{SIDE}} = 3.5 R$$

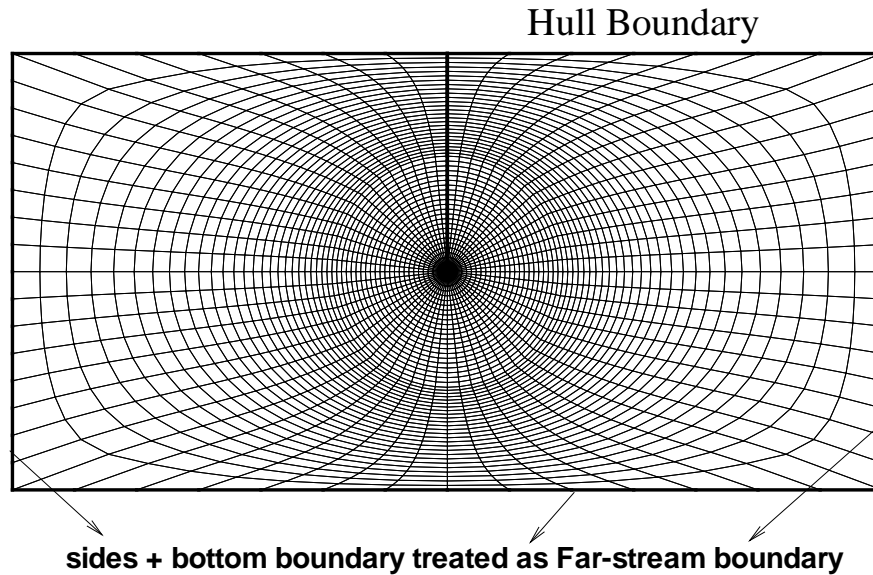
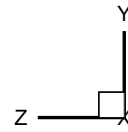


Figure 4.12: The grid at the inflow plane of the domain used in GBFLOW-3D showing the boundary conditions applied

4.2.1 Convergence Studies

Convergence studies are performed for PROPCAV applied to the rudder with the hull effects included through the images of the influence coefficients, as described in Section 3.3.1. Uniform inflow is assumed in predicting the propeller body forces using MPUF-3A. In GBFLOW-3D, the top boundary is treated as a flat hull, and the side and bottom boundaries are treated as far-stream boundaries, as shown in Figure 4.12. The inflow to the rudder induced by the propeller is predicted using GBFLOW-3D, with the body forces computed earlier, and is shown in Figure 4.13.

HULL ON TOP
 $Y_{TOP} = 1.756R$
 $Y_{BOT} = -1.756R$

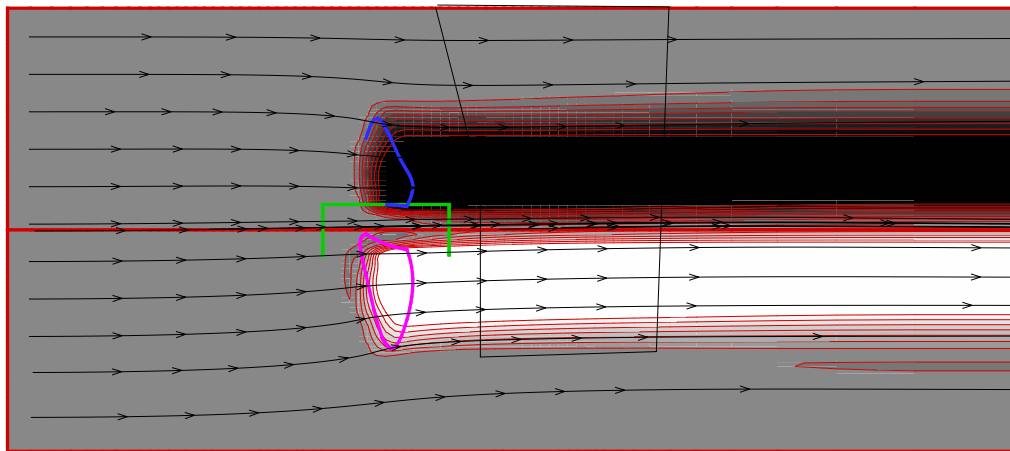
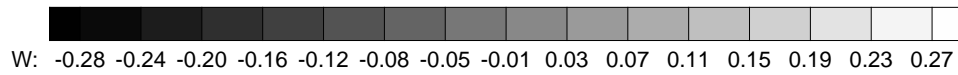
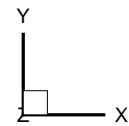


Figure 4.13: Solution at the center plane of the domain obtained from the 3-D Euler solver, with hull effects

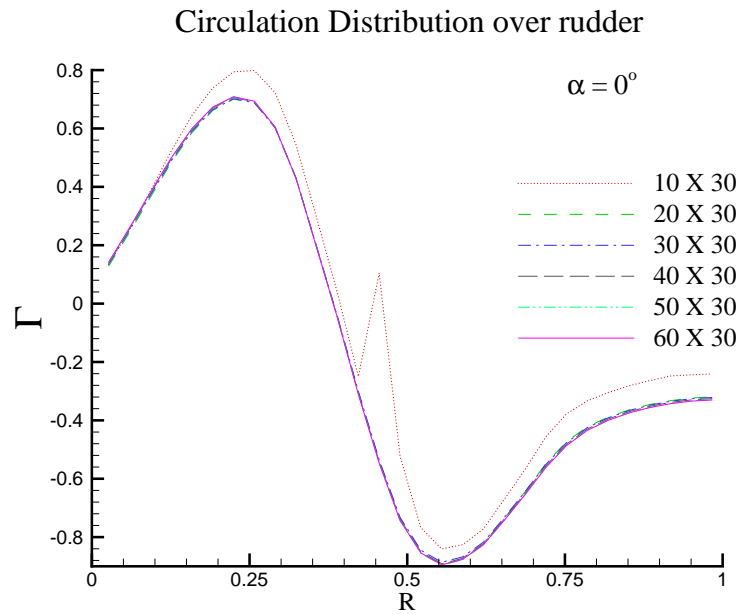


Figure 4.14: Convergence of circulation distribution with the number of panels in the chordwise direction. $R = 0$ is the lower tip and $R = 1.0$ is the upper tip of the rudder (close to the hull)

Figures 4.14 and 4.15 show the convergence of the circulation distribution obtained from PROPCAV, with varying chordwise panels and spanwise panels respectively. A full-cosine spacing along the chordwise direction and a uniform spacing along the spanwise direction is used. The circulation distribution is shown along the span of the rudder, in which $R = 0$ is the lower tip of the rudder, and $R = 1.0$ is the upper tip of the rudder (close to the hull). Convergence of the circulation distribution with increasing number of panels along the chordwise and spanwise direction is good. The convergence of pressure distribution along the strip located at $y/R = 0.34$ is shown in Figure 4.6. Convergence of the cavitation volume is shown in Figure 4.17.

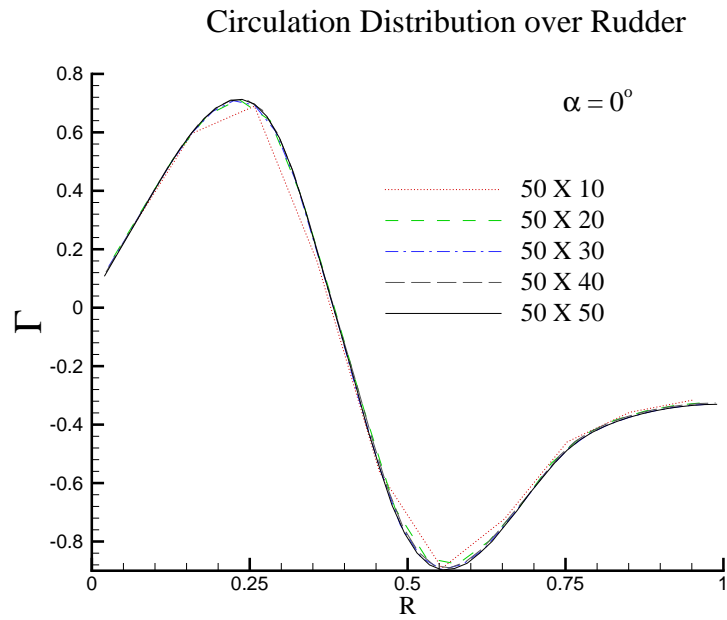


Figure 4.15: Convergence of circulation distribution with the number of panels in the spanwise direction. $R = 0$ is the lower tip and $R = 1.0$ is the upper tip of the rudder (close to the hull)

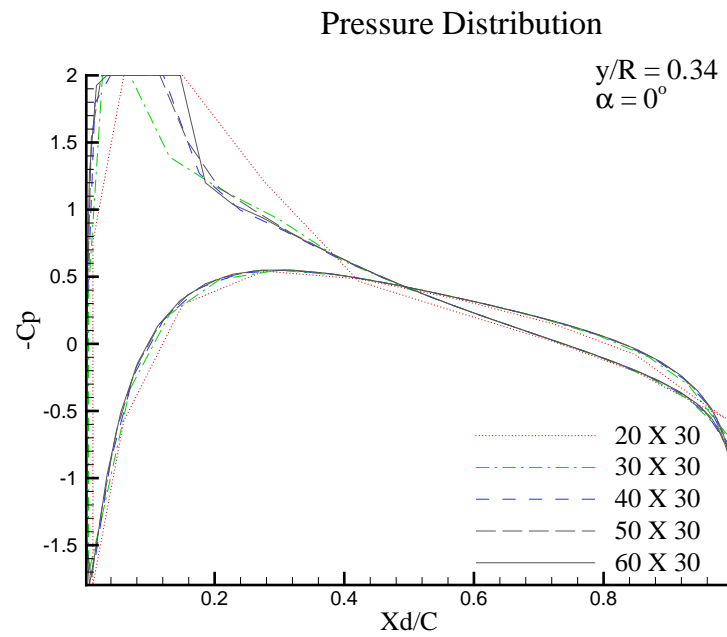


Figure 4.16: Convergence of pressure distribution along the strip at $y/R = 0.34$

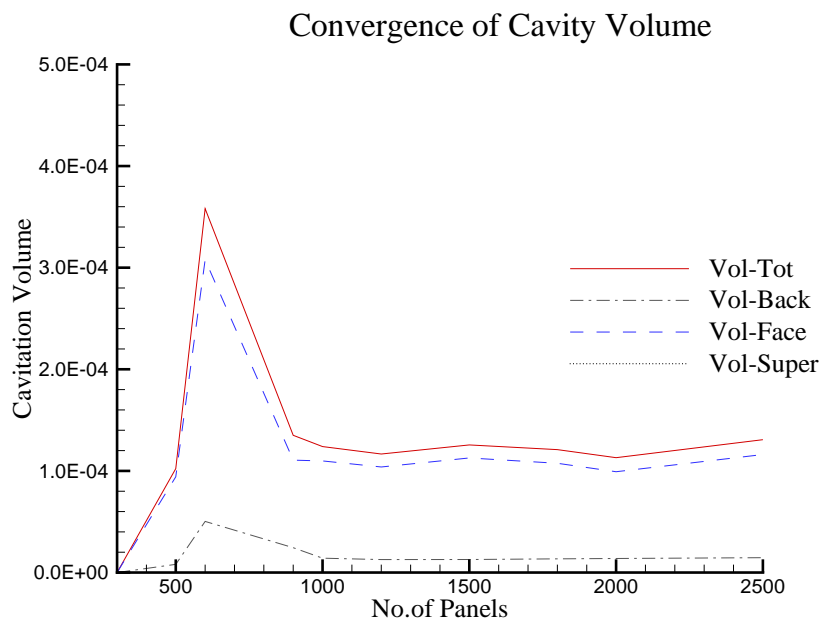


Figure 4.17: Convergence of cavitation volume with total number of panels

4.3 Comparison with Experimental Observations

The described approach is applied on rudders of various horn-type rudder geometries. Convergence studies on horn-type rudders are also performed. In order to validate the numerics of the method fully, it is essential to apply the method to a realistic geometry for which experimental data are available. The experiments were conducted for a horn-type rudder in the presence of a 6-bladed propeller, inside a cavitation tunnel. Details of the experiments are summarized in the next section. A photograph of the horn-type rudder and the corresponding BEM model are shown in Figure 4.18.

4.3.1 Summary of the Experiment

A series of experiments were conducted to determine the cavitation on the horn rudder subjected to an inflow induced by a 6-bladed propeller. The horn-type rudder has both movable and immovable parts. The movable part of the rudder is called the horn. The photographs were taken from the starboard side and sketches of the cavitation patterns on both port and starboard sides of the rudder were made, for a series of test conditions and rudder angles.

In the experiment, the propeller operates at a design thrust coefficient of $K_T = 0.2012$. The model tunnel also has hull appendages. The measured nominal axial velocity distribution at the propeller plane is shown in Figure 4.22.

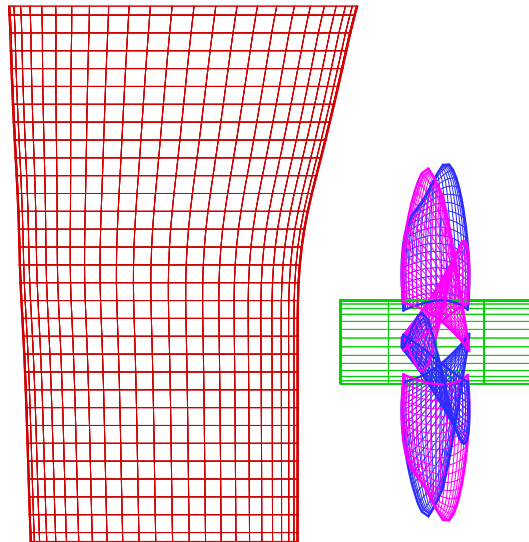
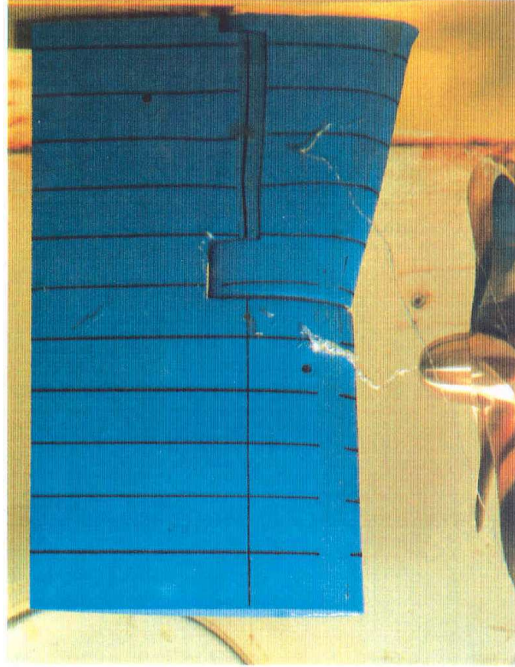


Figure 4.18: Photograph of a horn-type rudder geometry (top) with corresponding BEM model (bottom)

4.3.2 Definition of Rudder Angles

The cartesian coordinate system, as shown in Figure 4.19, is used in the three-dimensional BEM formulation. The origin of the coordinate system is located at the center of the bottom section of the rudder. The x-axis points downstream along the propeller shaft axis. The positive y-axis points vertically upward, and positive z-axis points towards port side of the ship.

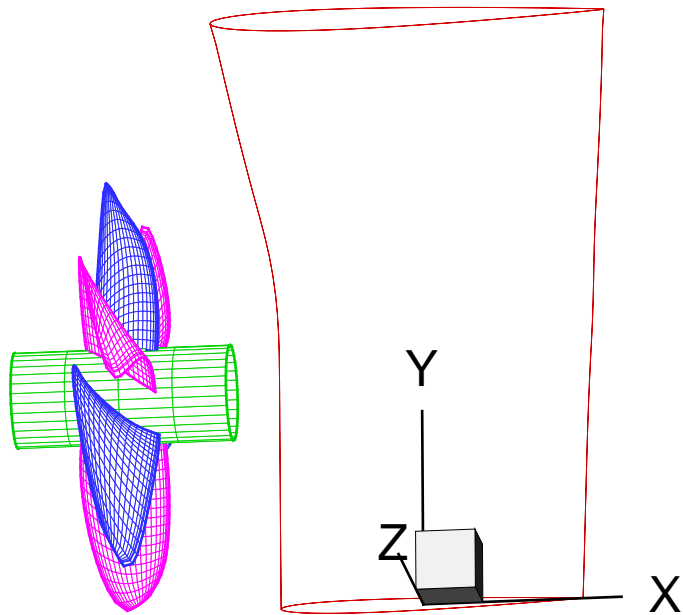


Figure 4.19: Cartesian coordinate system used in 3-D BEM formulation

In the experiment, the rudder turning angle towards the starboard side is considered to be positive, as shown in Figure 4.20. The movable horn part of the rudder is rotated about the rudder shaft axis, as shown in Figure 4.20. PROPCAV treats the rudder at an angle of attack, by rotating the inflow obtained over the rudder control points through an angle α , as shown in Figure 4.21. This procedure is valid for small angles of attack. In case of larger angles of attack the rudder should be rotated and

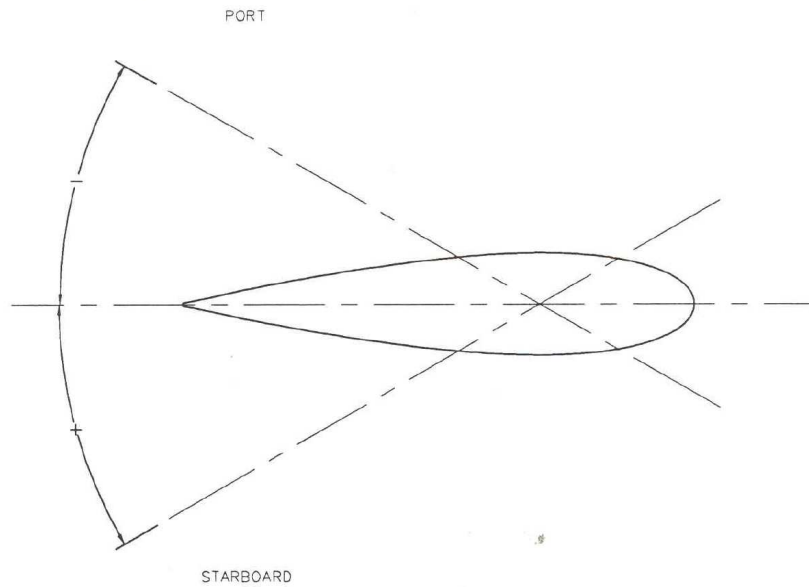


Figure 4.20: Definition of the rudder angle in the experiment

the propeller induced flow should be evaluated at the control points for the BEM.

4.3.3 Test Conditions Selected for Comparisons

The combination of test conditions selected is shown in Table 4.1. The experiment is performed at two cavitation numbers, $\sigma_R = 1.24$ and 1.65.

Under these conditions sheet cavitation occurs close to the bottom leading edge of the rudder surface. Sketches of the layout in the experiment are shown at the top of either Figures 4.32 and 4.33. For the same conditions cavitating hub and tip vortices from the propeller impinge on the rudder surface. In addition cavitation also occurs in the gap between the horn and the immovable part of the rudder. These types of cavitation are not addressed in this work.

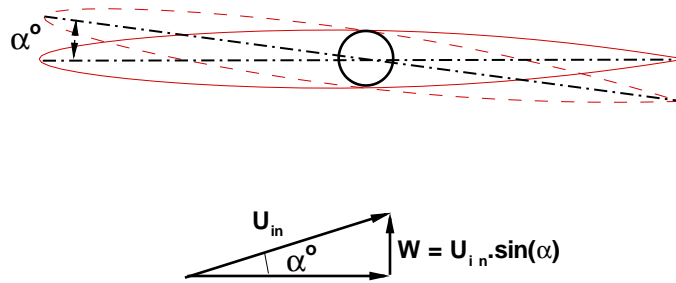


Figure 4.21: Definition of the angle of attack used in the BEM solver

Non-dimensional coefficients	Corresponding values
Model Scale Ratio	32.129
Model Ship Speed	2.305 m/s
Number of Blades	6
F_n	2.302
J_s	0.96

Table 4.1: Test conditions simulated in the model water tunnel testing facility

4.3.4 Nominal Wake at the Propeller Plane

The nominal wake is the velocity at an axial location upstream of the propeller in the absence of the propeller. The nominal axial velocity is measured at the propeller plane. The axial velocity distribution was measured at different angles and various radial locations. The circumferential variation in the axial velocity can be expressed in terms of harmonic coefficients as follows.

$$u(r, \theta) = A_0(r) + \sum_{n=1}^{\infty} \{A_n(r) \cos n\theta + B_n(r) \sin n\theta\} \quad (4.4)$$

The measured nominal axial velocity distribution is shown in Figure 4.22. The measured data are expressed in terms of cosine and sine harmonics, to be used for the prediction of propeller body forces in MPUF-3A. The axial velocity contours, reconstructed from the harmonics of the measured data, are shown in Figure 4.23.

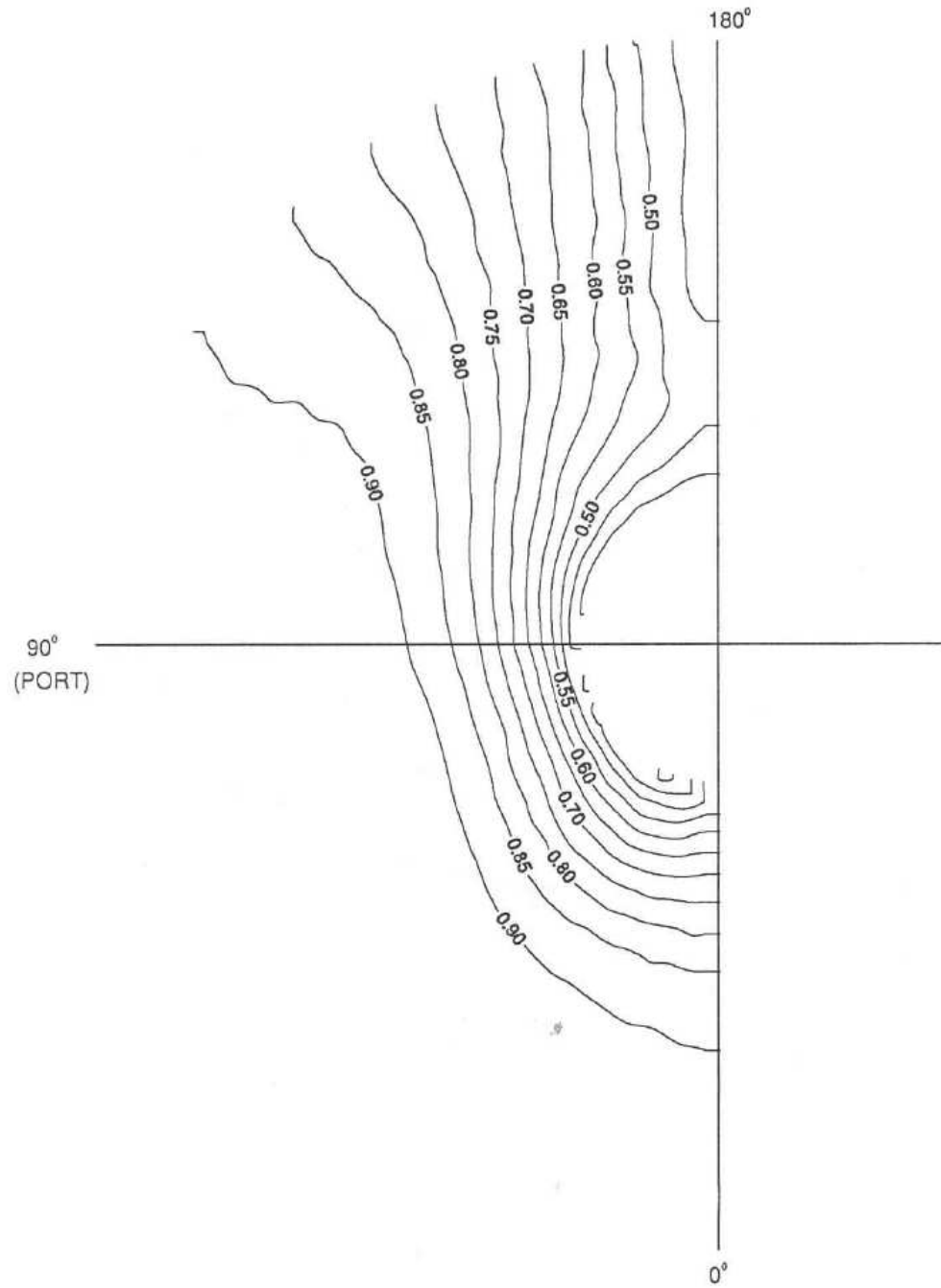


Figure 4.22: Measured axial nominal wake as seen by the propeller

Nominal Wake at the Propeller plane

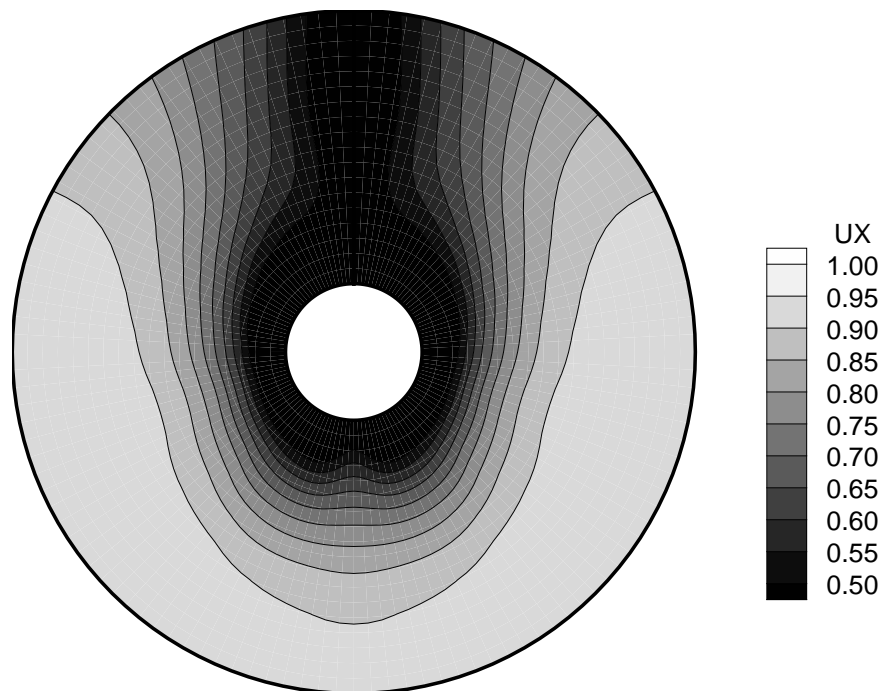


Figure 4.23: Nominal wake at the propeller plane reconstructed from the harmonic analysis of the data shown in the previous figure

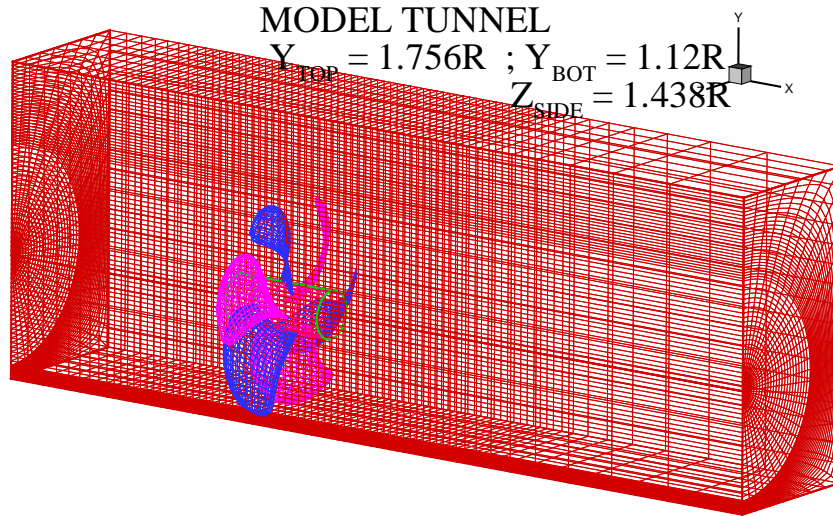


Figure 4.24: Computational domain used in GBFLOW-3D with the tunnel walls and the propeller shown. Only one half of the whole domain is shown.

4.3.5 Prediction of Effective Wake

The 6-bladed propeller is subjected to the inflow nominal wake shown in Figure 4.23. The flow induced by the propeller with the tunnel wall effects is computed using the 3-D Euler solver. The computational flow domain used in the 3-D Euler solver with $70 \times 50 \times 60$ cells in the axial, radial, and circumferential direction respectively (domain: $-3.0 \leq x \leq 5.0$) is shown in Figure 4.24. The propeller plane is located at $X = 0$, and the effective wake plane is evaluated at $X = -0.3$. Artificial dissipation coefficients $\sigma_2 = 0$ and $\sigma_4 = 1.5$ are applied.

The effective wake is predicted by considering the propeller-tunnel interaction, through an iterative run between MPUF-3A and GBFLOW-3D as described earlier, and is shown in Figure 4.25.

Effective Wake at the Propeller plane

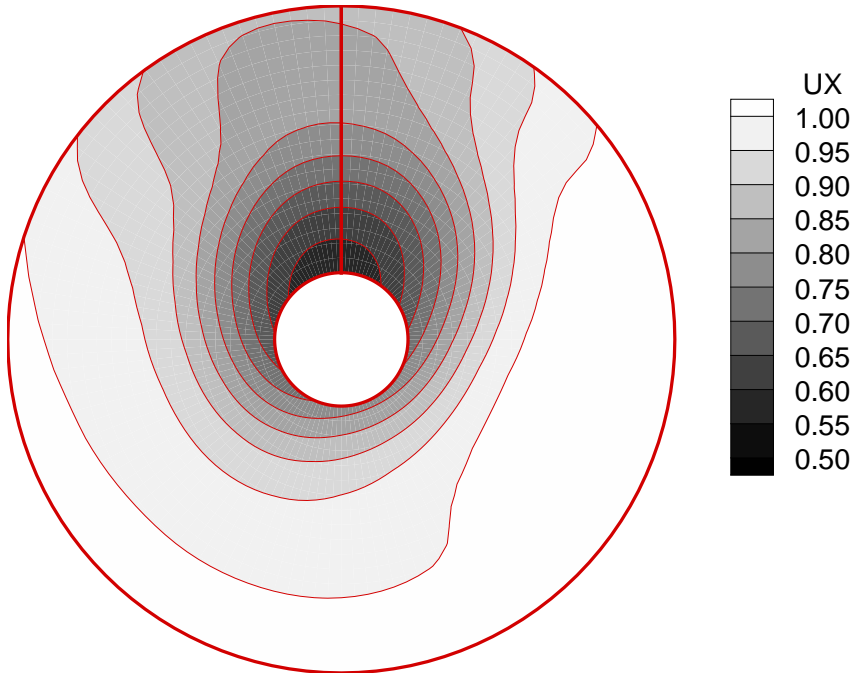


Figure 4.25: Effective wake predicted at the propeller plane, including the propeller-tunnel interaction

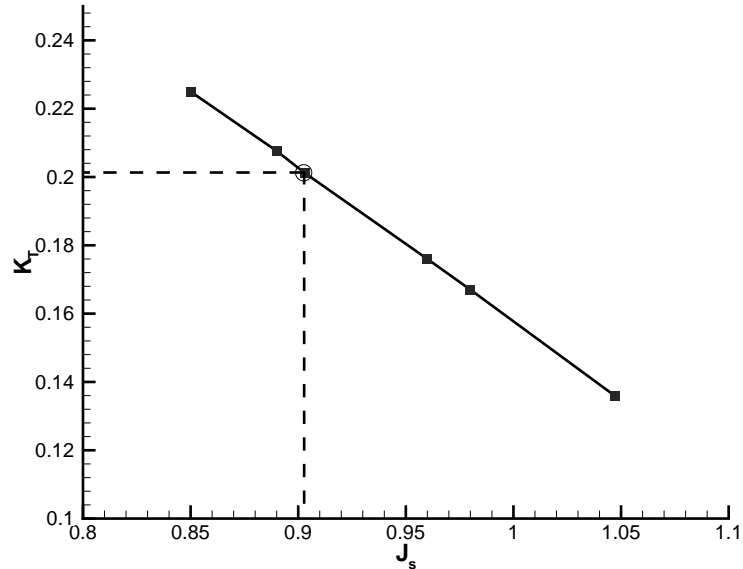


Figure 4.26: Advance ratio predicted for the design $K_T = 0.2012$ for the predicted effective wake through trial and error

4.3.6 Determining Inflow to the Rudder

The predicted effective wake is used as the inflow in MPUF-3A in order to compute the updated propeller loading. Then the propeller advance ratio is adjusted so that the resulting thrust coefficient matches the value of the design thrust coefficient in the experiment. The propeller thrust coefficient is determined at various advance ratios, as shown in Figure 4.26, and the advance ratio which corresponds to the desired value of $K_T = 0.2012$ is achieved through trial and error. The predicted circulation distributions for the propeller using the provided nominal wake and the predicted effective wake are shown in Figure 4.27.

The values of the advance ratio and some other related coefficients in the case of the nominal and the effective wake are given in Table 4.2.

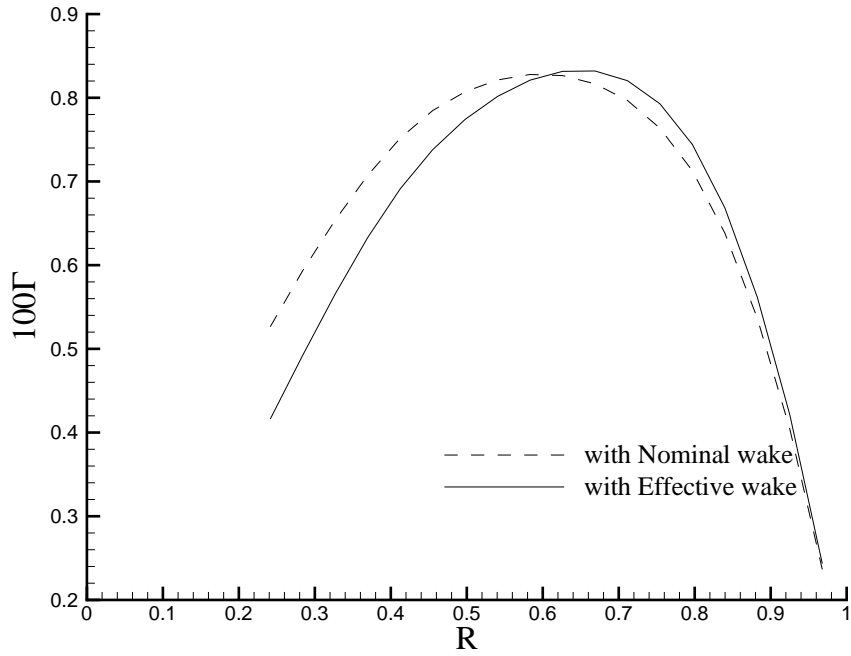


Figure 4.27: Comparison of the loading on the propeller predicted by MPUF-3A using the provided nominal wake and the predicted effective wake

Non-dimensional coefficients	with effective wake	with nominal wake
K_T	0.2012	0.2012
F_n	2.2016	2.302
J_s	0.903	0.96
$F_{r_{rudder}}$	1.5	1.5

Table 4.2: The values of various coefficients using the nominal and the effective wake

MODEL TUNNEL

$$Y_{\text{TOP}} = 1.756R, Y_{\text{BOT}} = 1.12R, Z_{\text{SIDE}} = 1.438R$$



U: 0.10 0.21 0.31 0.42 0.52 0.63 0.73 0.84 0.94 1.05 1.15

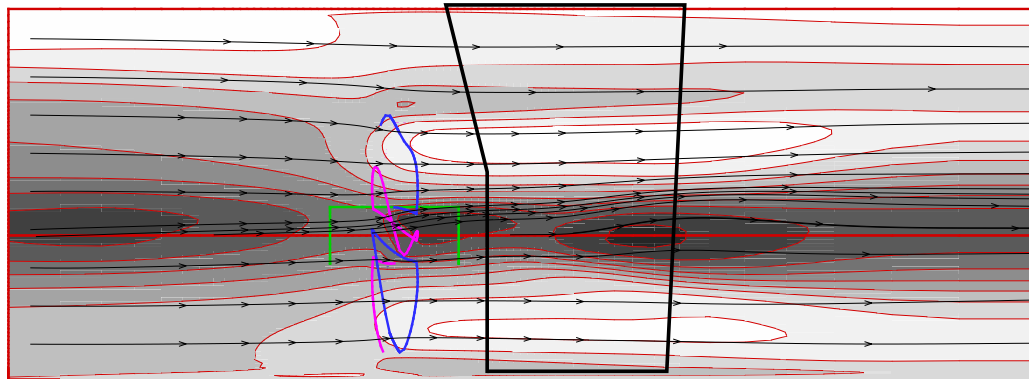


Figure 4.28: Predicted axial velocity contours and streamlines of the propeller flow field at the center plane of the domain

Figure 4.28 shows the axial velocity contours and streamlines at the center plane of the domain. In Figure 4.29, the pressure contours are shown. The expected pressure jump can be seen in the figure across the propeller plane. It should be noted that even though the rudder is shown in these figures, it has not been modeled in the GBFLOW-3D/MPUF-3A simulation.

The tangential velocity contours are shown in the Figure 4.30. Over the rudder, in the propeller slipstream, the tangential velocity varies from positive below the propeller shaft axis to negative above the propeller shaft axis. This variation of the tangential velocity will induce a varying angle of attack over the span of the rudder. The angle of attack varies from negative below the propeller shaft axis to positive above the propeller shaft axis. The tangential velocity contours and total velocity vectors are shown over the rudder in Figure 4.31

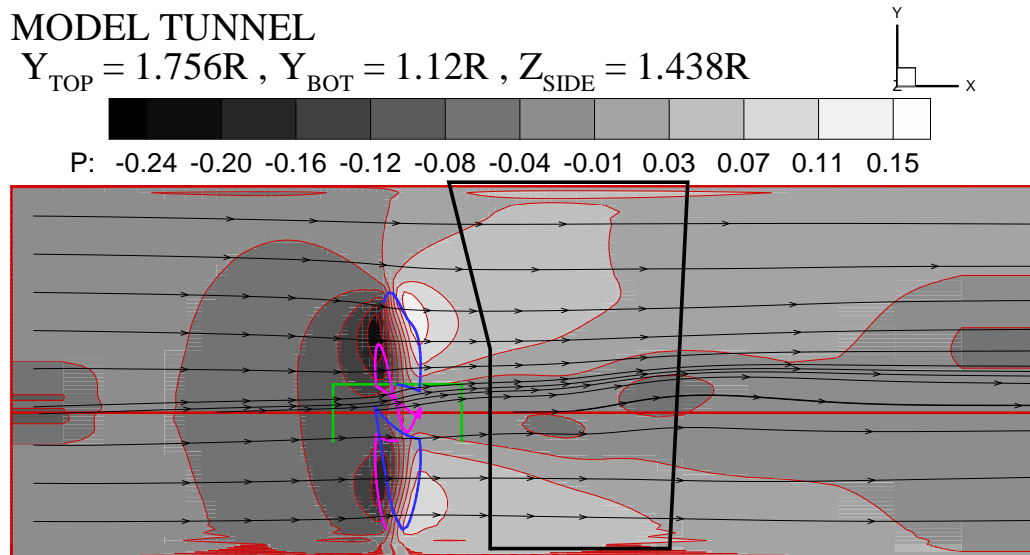


Figure 4.29: Predicted pressure contours and streamlines of the propeller flow field at the center plane of the domain

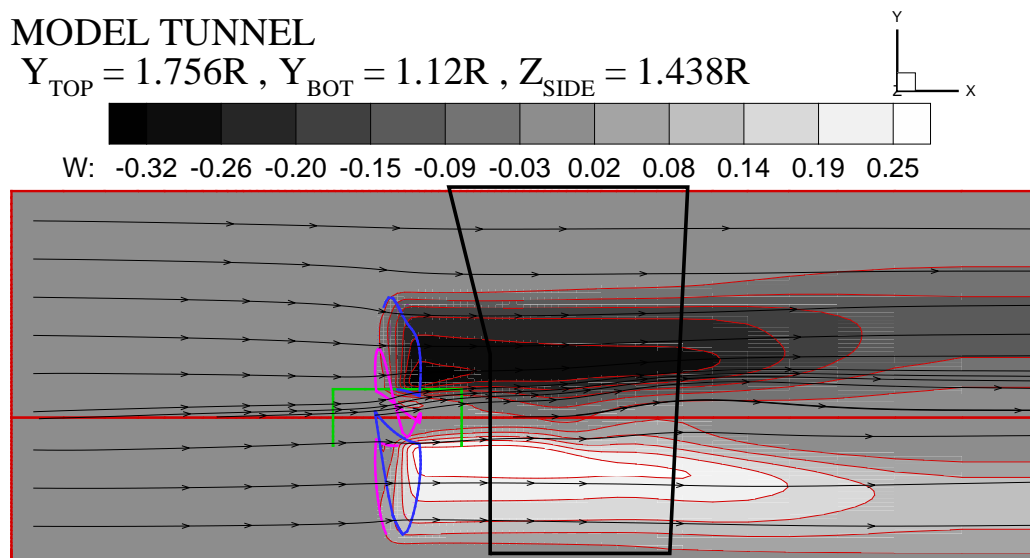


Figure 4.30: Tangential velocity contours and streamlines of the propeller flow field at the center plane of the domain

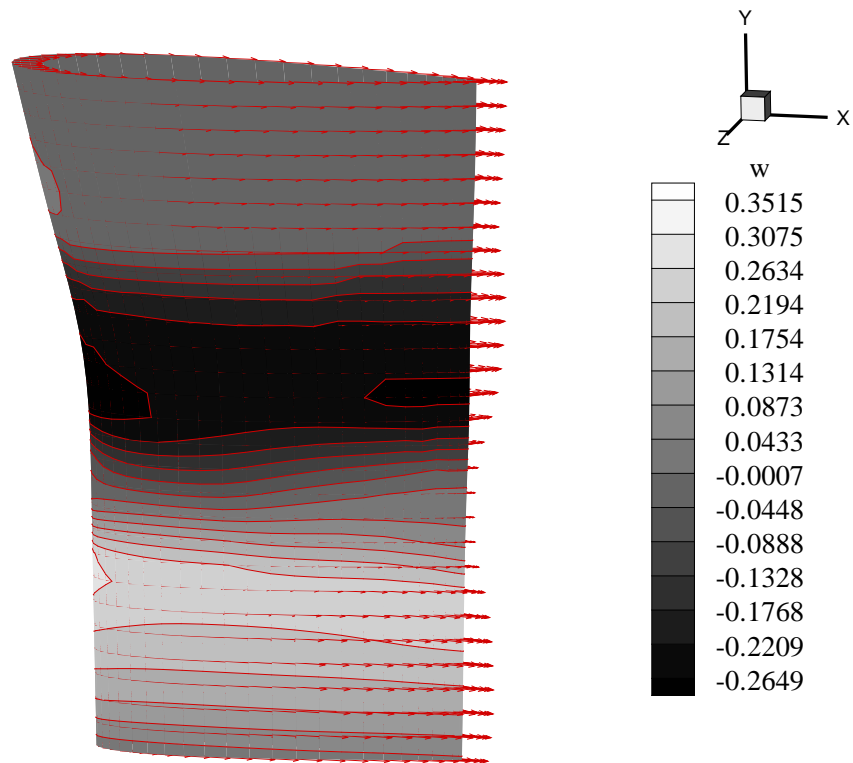


Figure 4.31: Tangential velocity contours and total velocity vectors induced by the propeller to the horn-type rudder

4.3.7 Comparison with Observations from Experiments

The flow-field determined in the previous section is used as the inflow in PROPCAV in order to predict rudder cavitation. In the present work PROPCAV accounts for the top wall (hull) via images (as already described), but does not account for the side and bottom walls of the tunnel, and this could affect the predicted cavity patterns. The effect of side and bottom walls could be included by using a method similar to that described in Kinnas et al. [1998b].

The predicted sheet cavity patterns on the portside of the rudder are shown in Figures 4.32 and 4.33 for two cavitation numbers, together with the observed. The predicted patterns of sheet cavitation seem to match those observed.

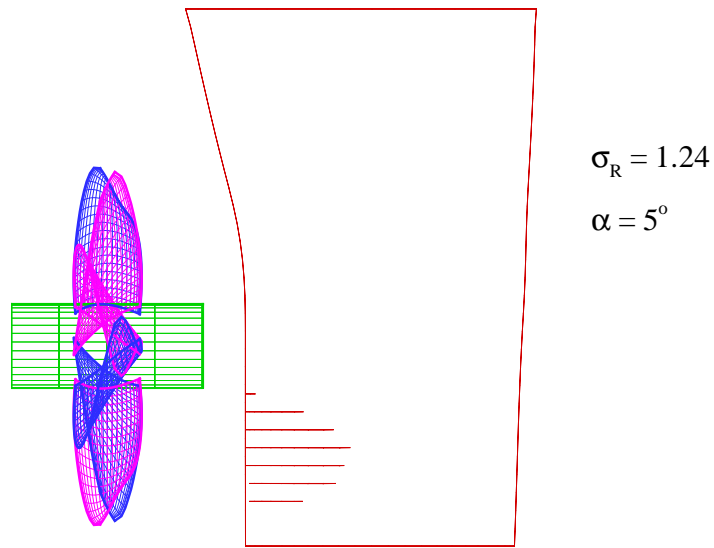
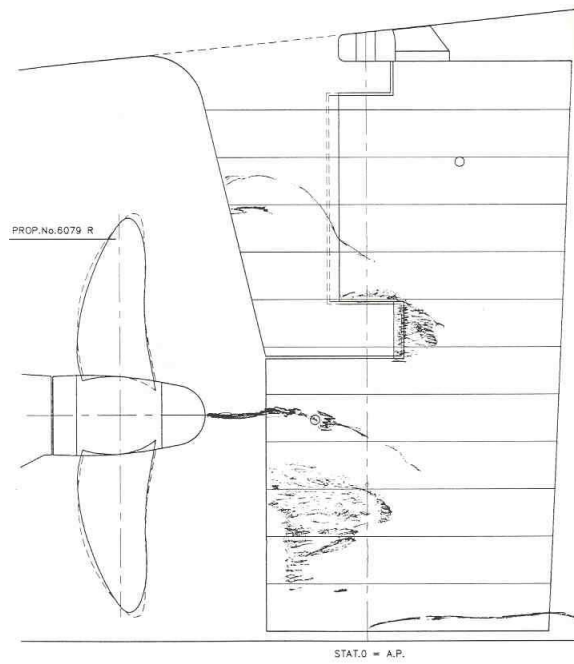


Figure 4.32: Cavity pattern observed (top) and predicted by PROPCAV (bottom) on the port side at a cavitation number $\sigma_R = 1.24$ and $\alpha = 5^\circ$

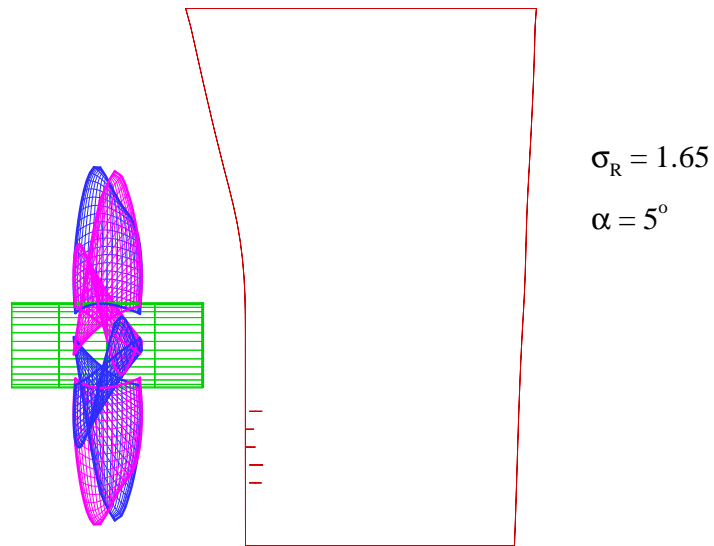
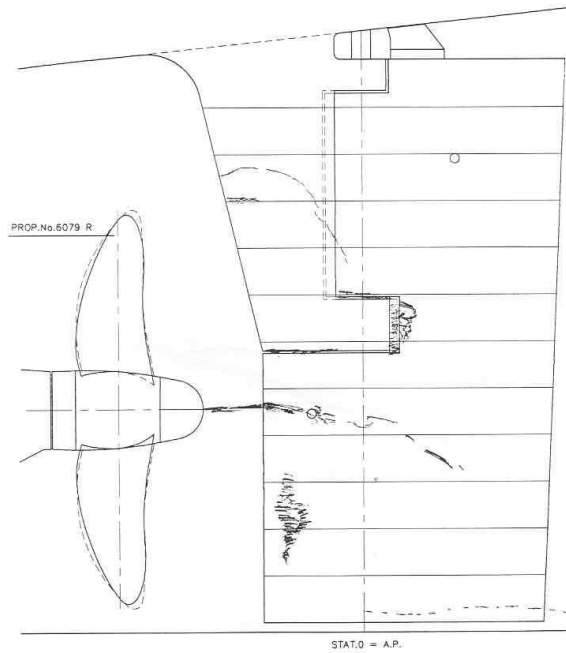


Figure 4.33: Cavity pattern observed (top) and predicted by PROPCAV (bottom) on the port side at a cavitation number $\sigma_R = 1.65$ and $\alpha = 5^\circ$

4.4 Flapped Rudder

The described method is extended to predict the performance of a flapped rudder.

The rudder section, which is a typical hydrofoil section is rotated through an angle α_{flap} , about the pivot axis, which is at a distance of X_f from the leading edge at the bottom section of the rudder, as shown in Figure 4.34. The surface of the rudder, and the flap are re-paneled as shown in Figure 4.35. The wake geometry is aligned such that it leaves from the trailing edge of the rudder at zero angle with respect to the unflapped chord.

The gap between the flap and the main rudder is considered to be sealed hydrodynamically. The gap flow could be modeled by using a method similar to that described in [Pyo and Suh 2000].

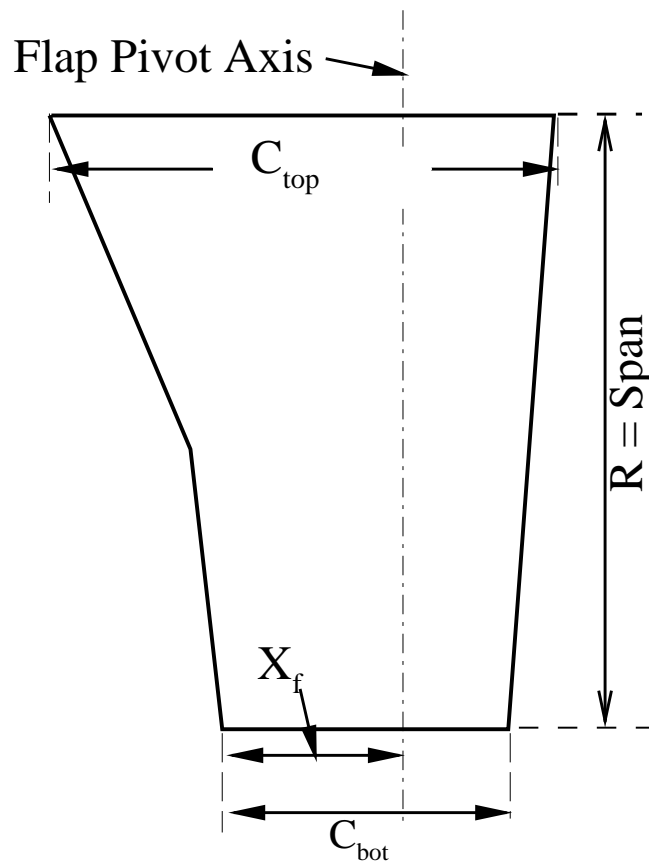
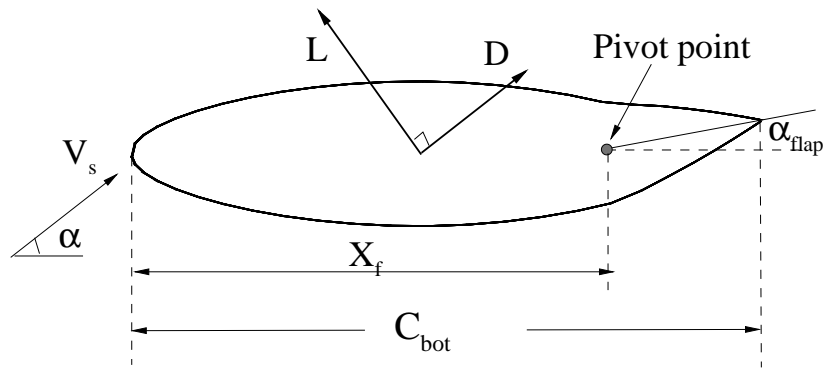


Figure 4.34: Definition of pivot axis and flap angle for flapped rudder

FLAPPED RUDDER GEOMETRY

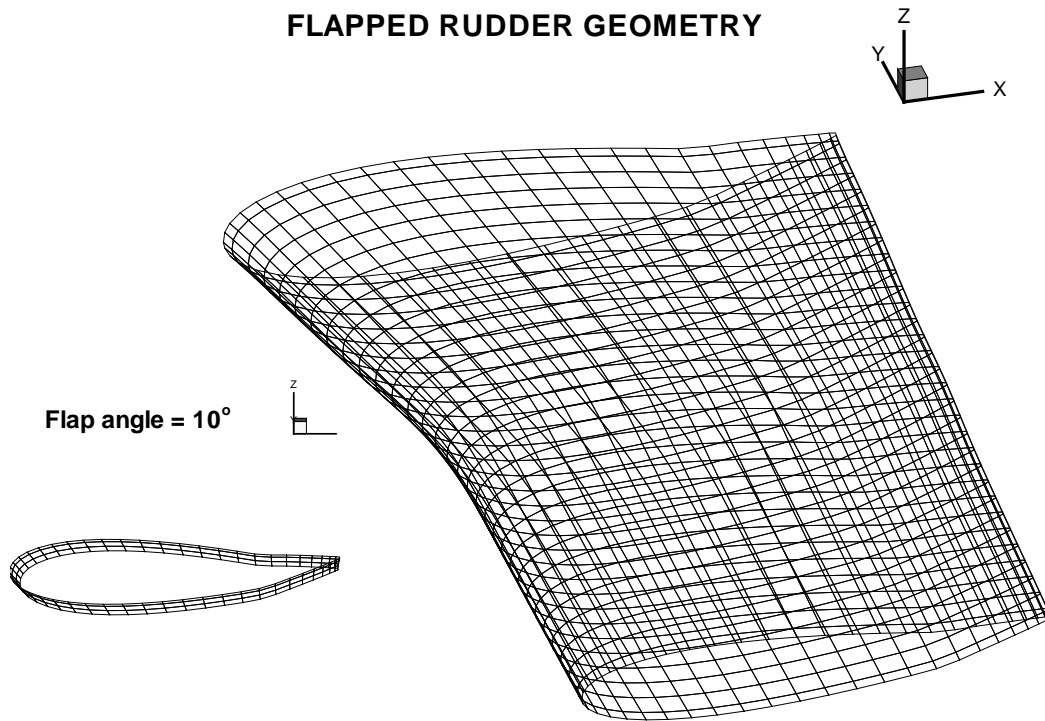


Figure 4.35: Re-paneled geometry of the flapped rudder with a flap angle $\alpha_{flap} = 10^\circ$ and flap pivot axis $X_f/C_{bot} = 0.75$

4.4.1 Convergence Studies for a Flapped Rudder

The two important parameters in this problem are the number of panels along the chordwise and spanwise directions. Convergence studies are shown for both the circulation and pressure distributions over a rudder.

The flapped rudder is subjected to uniform inflow with an angle of attack $\alpha = 0^\circ$. A flap angle of $\alpha_{flap} = 10^\circ$ is introduced about the pivot axis located at 75% of the chord at the bottom section from the leading edge, as shown in Figure 4.35.

The convergence of the circulation distribution obtained from PROPCAV with increasing number of chordwise and spanwise panels is shown in Figures 4.36 and 4.37, respectively. Figure 4.39 shows the convergence of pressure distribution along a strip, at a spanwise location shown in Figure 4.38.

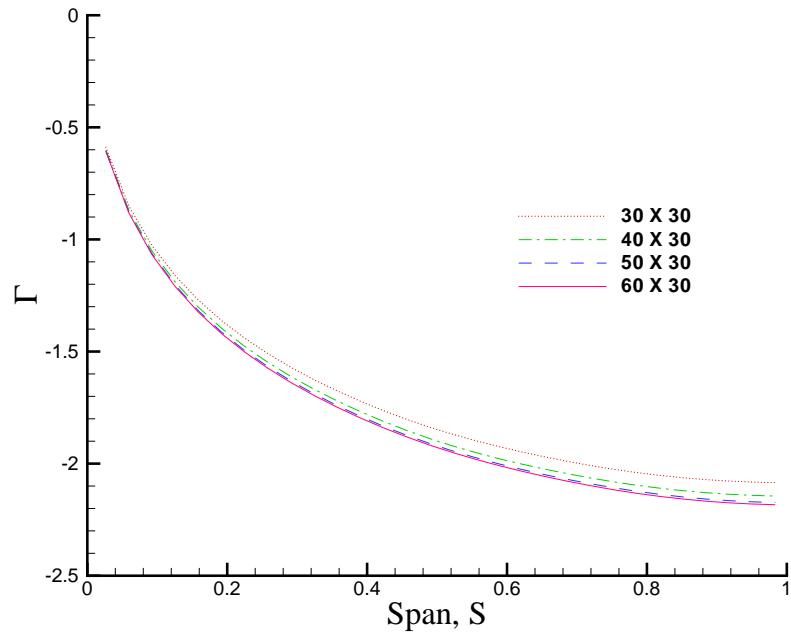


Figure 4.36: Convergence of circulation in chordwise direction for a rudder with flap angle, $\alpha_{flap} = 10^\circ$ and $X_f/C_{bot} = 0.75$

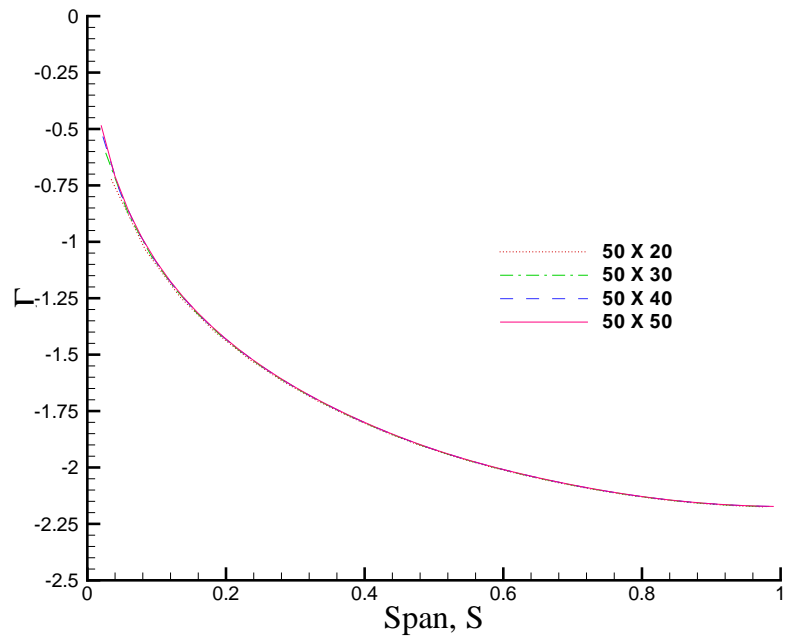


Figure 4.37: Convergence of circulation in spanwise direction for a rudder with flap angle, $\alpha_{flap} = 10^\circ$ and $X_f/C_{bot} = 0.75$

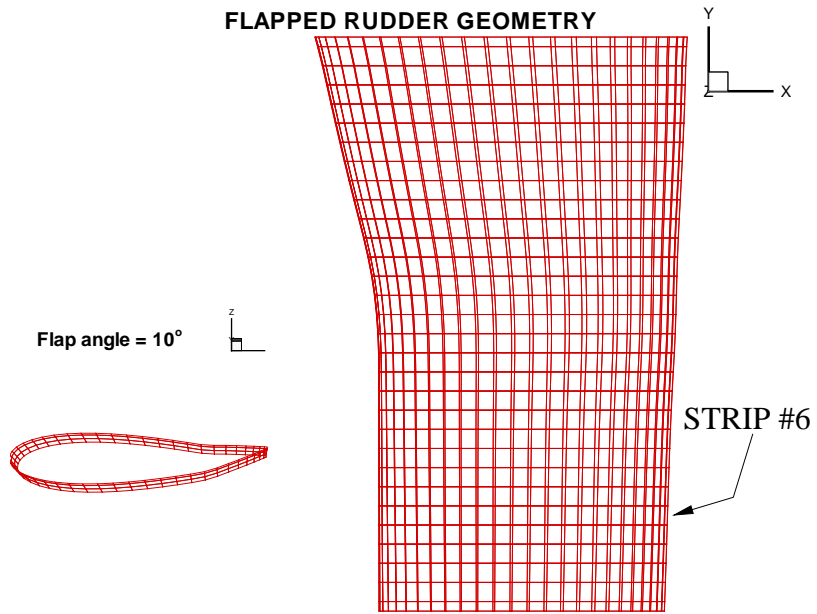


Figure 4.38: Location of the panel strip along the span of the rudder at which the convergence of pressure distribution with the number of chordwise panels is studied

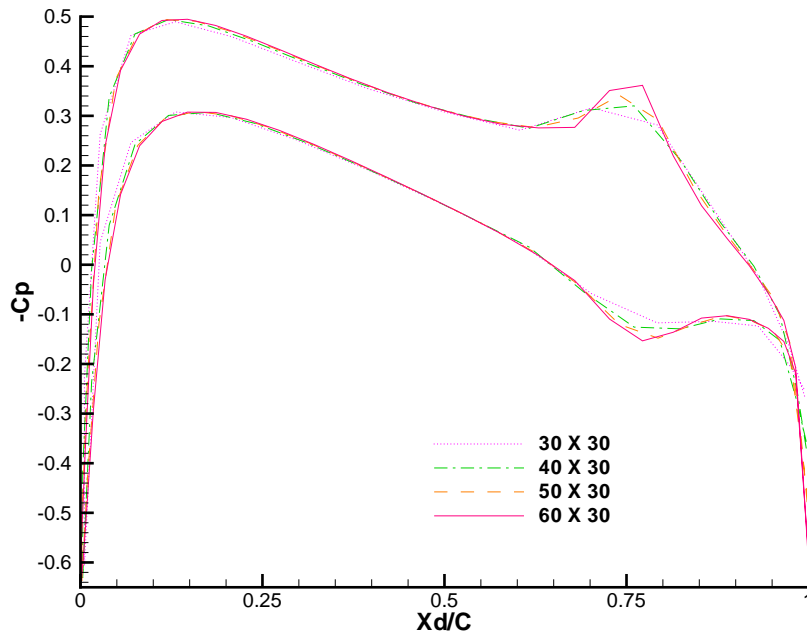


Figure 4.39: Convergence of pressure distribution (along the strip-6 shown in Figure 4.38) for a rudder with flap angle, $\alpha_{flap} = 10^\circ$ and $X_f/C_{bot} = 0.75$

4.4.2 Results for a Flapped Rudder

In this section, predictions of the hydrodynamic forces and the cavity shapes from using PROPCAV on a flapped rudder are presented. The rudder is subjected to a uniform inflow as well as an inflow induced by a propeller.

The lift and drag coefficients for a flapped rudder, with various flap angles are shown in Figure 4.40. The rudder is subjected to a uniform inflow with zero angle of attack. It is seen that with the introduction of small flap angles the rudder produces higher lift and drag forces. The circulation distributions for various flap angles are shown in Figure 4.41. The negative sign in the circulation is due to the fact that positive circulation is defined in the clockwise direction. The lift and drag forces on the rudder with a flap angle $\alpha_{flap} = 0^\circ$, at an angle of attack $\alpha = 0^\circ$ should be 0. The small value of drag at $\alpha_{flap} = 0^\circ$ is due to numerical pressure integration error.

In Figures 4.42 and 4.43, cavity patterns predicted for a flapped rudder subjected to a uniform inflow at a cavitation number $\sigma_R = 0.55$ are shown. It is seen that with a flap angle $\alpha_{flap} = -10^\circ$, the cavitation occurs on the port side of the rudder, and at a flap angle $\alpha_{flap} = 10^\circ$, the cavitation occurs on the starboard side of the rudder. The cavity extends beyond the flap knuckle and the predicted cavities are the image of each other, as expected. This simple test verifies the code in the case of mid-chord back or face cavitation.

The cavity patterns are also predicted for an inflow induced by the propeller, as predicted by GBFLOW-3D/MPUF-3A. The axial velocity contours and the streamlines are shown in Figure 4.44. Figure 4.45 shows the tangential velocity contours. Figures 4.46 and 4.47 show the effect of the flap angle on the predicted cavitation.

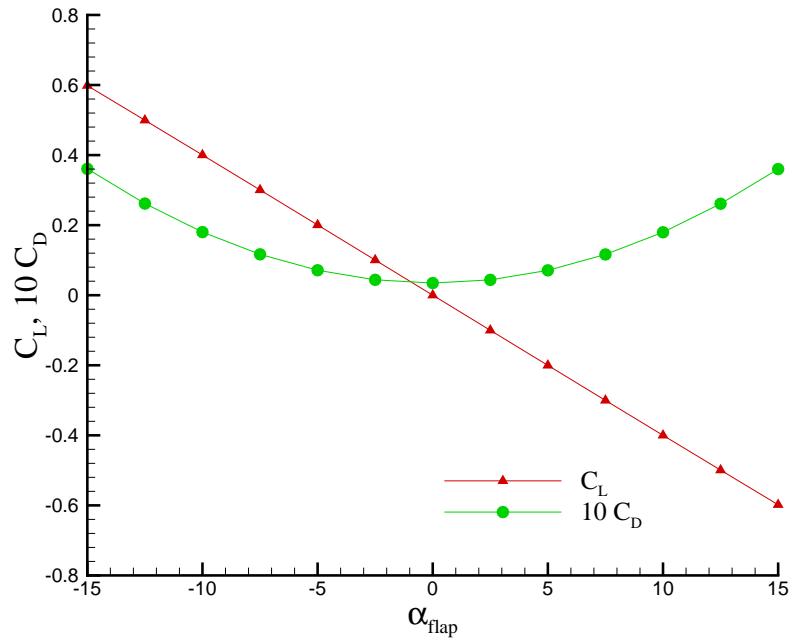


Figure 4.40: Lift and drag coefficients for a flapped rudder with varying flap angles subjected to a uniform inflow

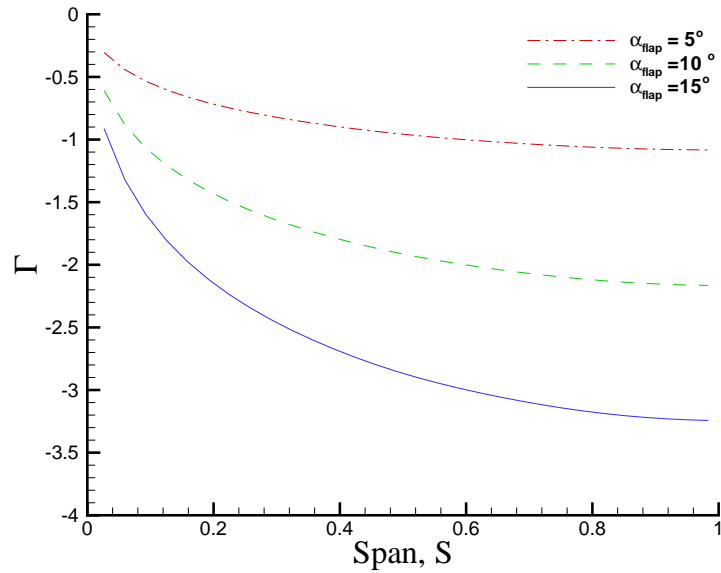


Figure 4.41: Circulation distribution for a flapped rudder with varying flap angles subjected to a uniform inflow

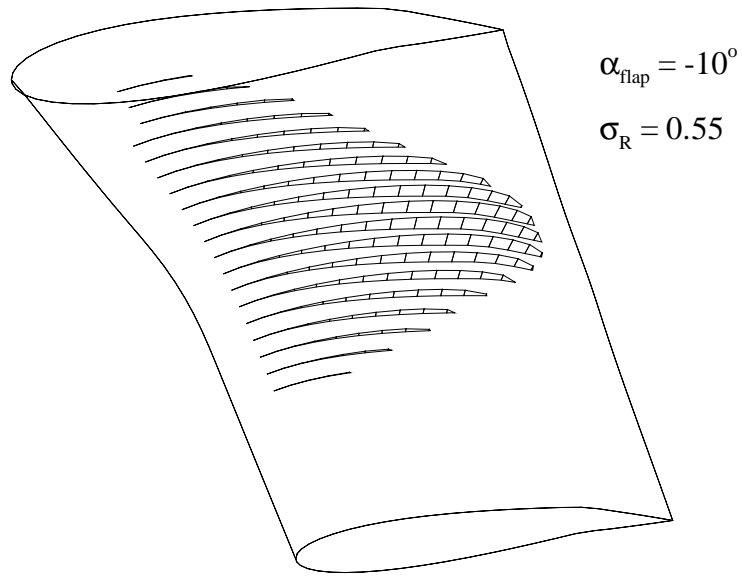


Figure 4.42: Cavitation for a flapped rudder subjected to a uniform inflow at a cavitation number $\sigma_R = 0.55$ and a flap angle $\alpha_{\text{flap}} = -10^\circ$; predicted by PROPCAV

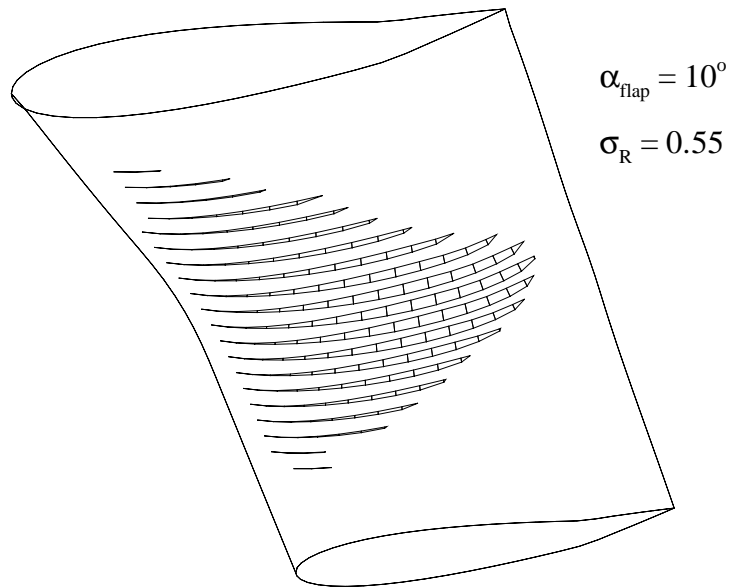


Figure 4.43: Cavitation for a flapped rudder subjected to a uniform inflow at a cavitation number $\sigma_R = 0.55$ and a flap angle $\alpha_{\text{flap}} = 10^\circ$; predicted by PROPCAV

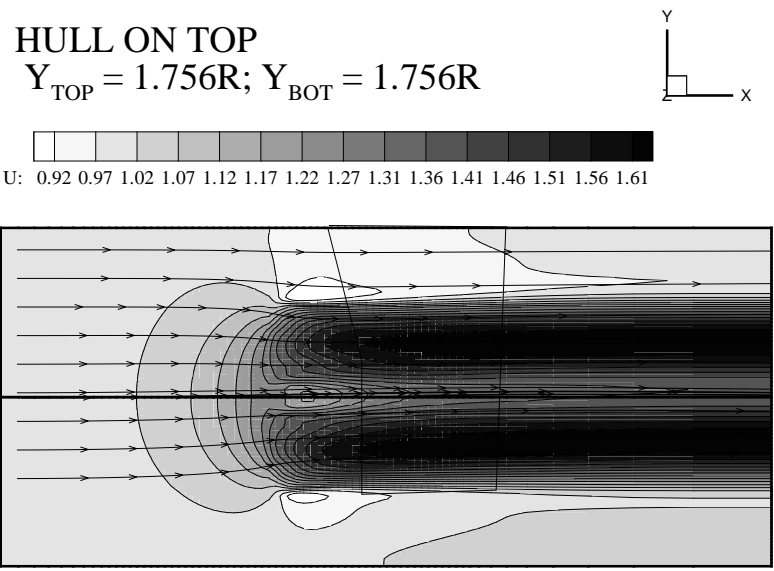


Figure 4.44: Axial velocity contours and streamlines of the propeller flow field at the center plane of the domain

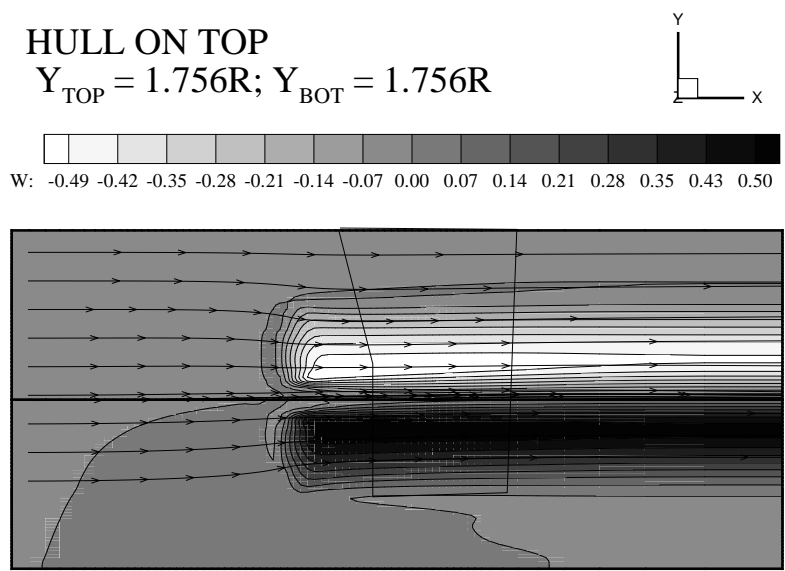


Figure 4.45: Tangential velocity contours and streamlines of the propeller flow field at the center plane of the domain

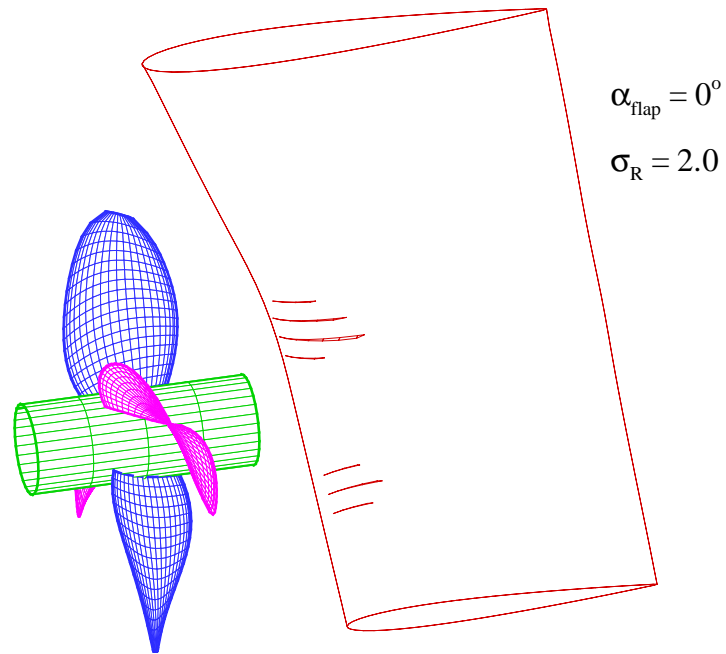


Figure 4.46: Cavitation for a flapped rudder subjected to an inflow induced by the propeller at a cavitation number $\sigma_R = 2.0$ and a flap angle $\alpha_{\text{flap}} = 0^\circ$

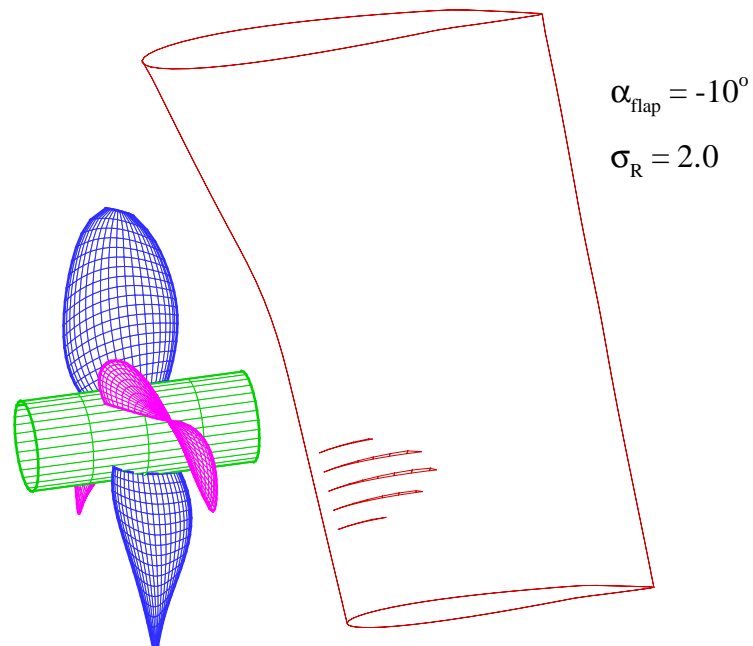


Figure 4.47: Cavitation for a flapped rudder subjected to an inflow induced by the propeller at a cavitation number $\sigma_R = 2.0$ and a flap angle $\alpha_{\text{flap}} = -10^\circ$

4.5 Twisted Rudder

Twisted rudders can be used to avoid cavitation on their surface when the ship travels on a straight path. A twisted rudder is shown in Figure 4.48.

To evaluate the effect of twist angles on the predicted cavitation, the twist distribution shown in Figure 4.49 is applied over a rudder. The predicted cavitation over the twisted rudder subject to the inflow induced by a propeller (shown in Figures 4.44 and 4.45) is presented in this section. The inflow to the twisted rudder, as induced by the propeller, is shown over the rudder control points in Figure 4.50. The propeller produces a swirl which induces a varying angle of attack over the span of the rudder. If a “twist” is applied such that it cancels the induced angle of attack, the cavitation can be reduced.

In Figure 4.51, the cavitation over a rudder without a twist, at a cavitation number $\sigma_R = 2.0$ is shown. As shown in Figure 4.52, with the introduction of a “twist” which cancels the induced angle of attack above the propeller axis, the cavitation on the starboard side of the rudder has been reduced considerably. For this case though the cavitation on the portside has been increased. An appropriate twist distribution could be devised to avoid cavitation over both sides of the rudder. The current method can be used to assess the effect of different twist distributions on the amount of cavitation.

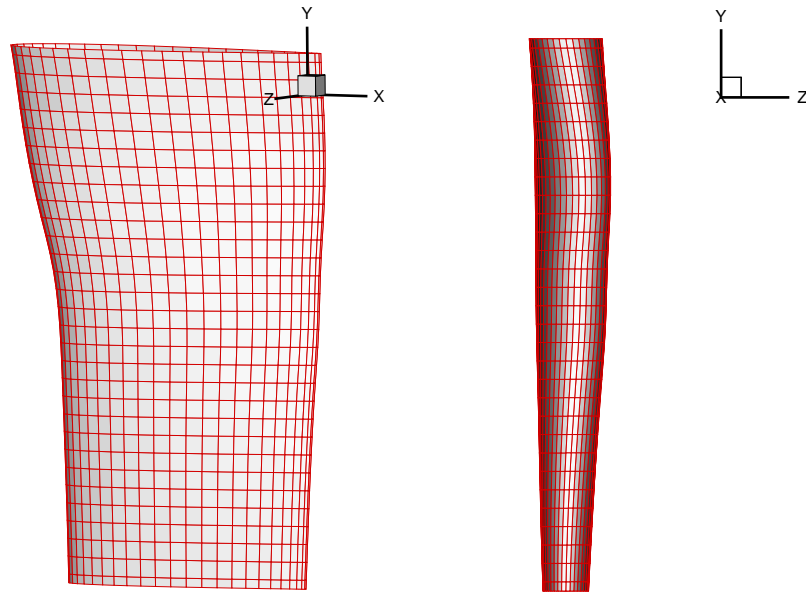


Figure 4.48: BEM model of the twisted rudder geometry

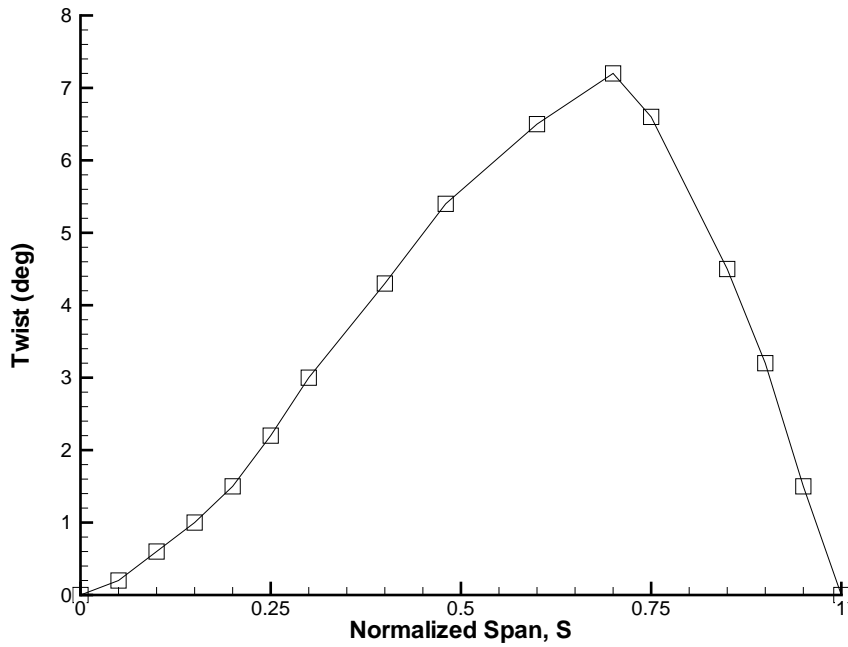


Figure 4.49: Twist angle in degrees over the span of the rudder. $S=0$ is the lower tip of the rudder and $S=1.0$ is the upper tip of the rudder.

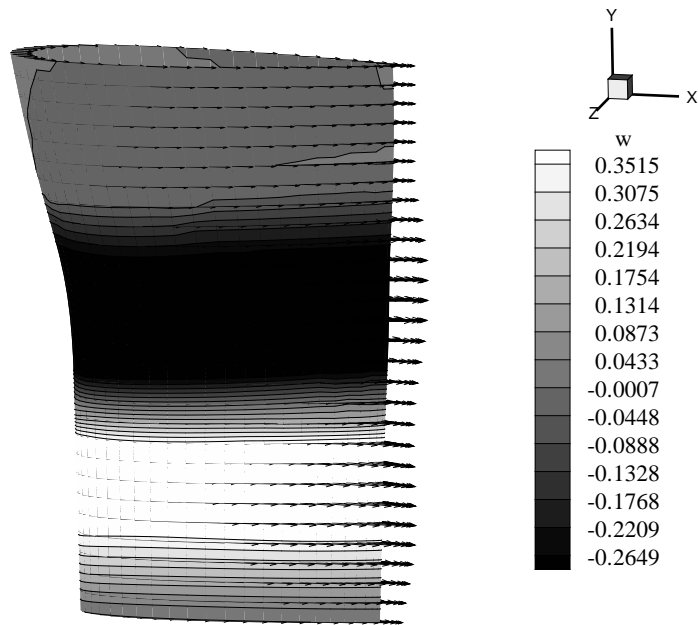


Figure 4.50: Tangential velocity contours and total velocity vectors for the propeller induced flow field over the twisted rudder

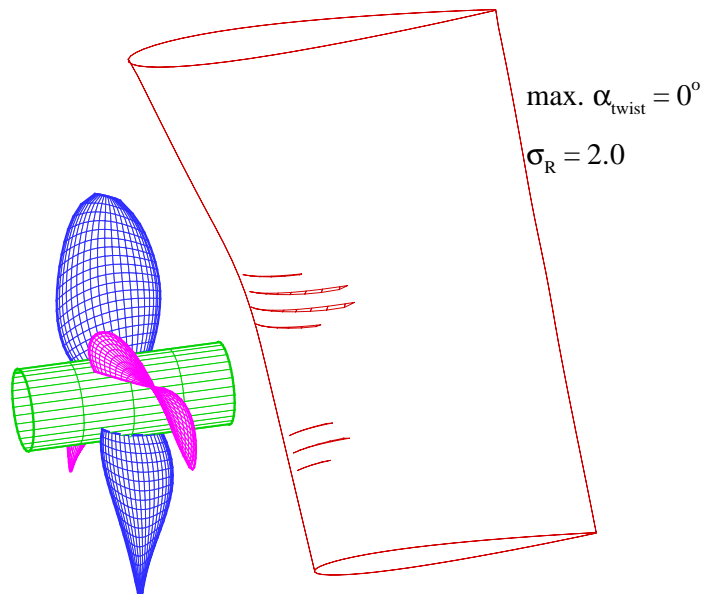


Figure 4.51: Cavitation for a twisted rudder subjected to a propeller induced inflow at a cavitation number $\sigma_R = 2.0$ and a maximum twist angle $\alpha_{twist} = 0^\circ$; predicted by PROPCAV

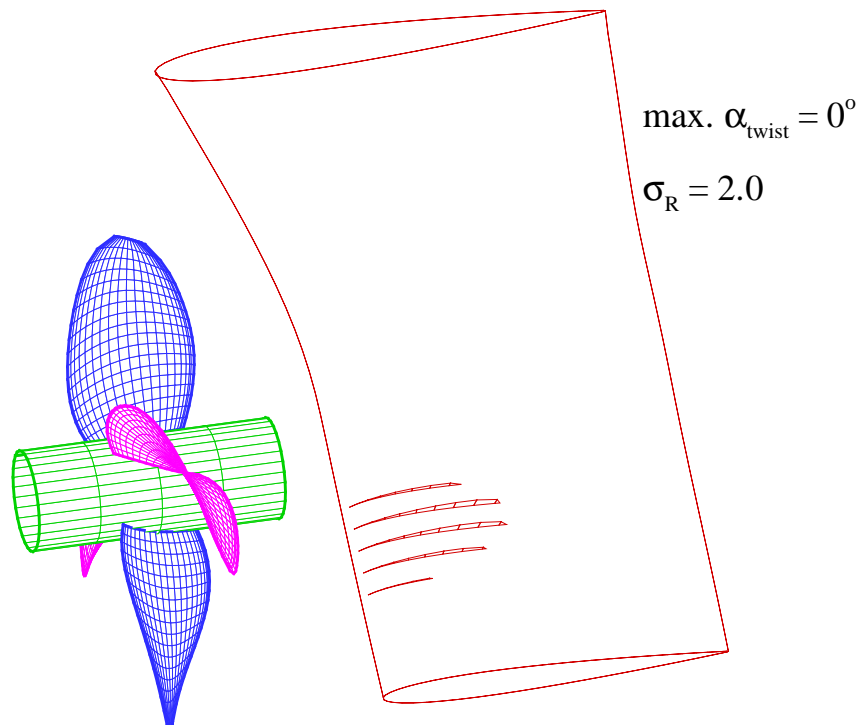


Figure 4.52: Cavitation for a twisted rudder subjected to a propeller induced inflow at a cavitation number $\sigma_R = 2.0$ and a maximum twist angle $\alpha_{twist} = 7.2^\circ$; predicted by PROPCAV

Chapter 5

The Propeller-Rudder Interaction

As already mentioned the effect of the rudder on the propeller could be significant in the case the blockage effects due to the rudder alter the inflow to the propeller.

This chapter discusses the application of the 3-D Euler solver to the problem of propeller-rudder interaction, unlike the work presented in Chapter 4, where only the influence of propeller on the rudder is considered.

The iterative method between the VLM and the 3-D Euler solver is extended in this section to consider the propeller-rudder interaction. The basic idea behind the coupled approach is to predict the effective wake to the propeller which includes the rudder blockage effects. To achieve this objective we solve the Euler equations using a multi-block approach. The propeller is represented by body forces in one finite volume block, whereas the rudder is represented as a solid boundary in the other finite volume block. Since the propeller is represented by body forces a cylindrical grid is more suitable to compute the flow field inside the propeller block. To extend this cylindrical grid over the region where the rudder is located is a very difficult task. On the other hand, it is relatively easy to generate a H-type grid based on a cartesian coordinate system over the rudder. Hence, the flow inside the rudder block

is computed using a H-type grid.

To obtain the interaction between the two blocks, overlapping non-matching grids are used which exchange information on their boundaries through interpolation. This multi-block approach ¹ provides the three-way interaction between the inflow, the propeller and the rudder.

In this chapter, first the H-type grid over the rudder is described, and results from the 3-D Euler solver in the case of a rudder subjected to uniform inflow are presented. The method and results presented in this chapter are “original”. Therefore, the need arises to validate the solver sufficiently before applying it to the intended problem. Hence, the results obtained from the 3-D Euler solver are validated using the results from a boundary element method. This chapter also describes the interpolation scheme which is used to exchange the boundary information between the two blocks. Since the interpolation is performed between two non-matching meshes, validation tests are performed to test the robustness of the interpolation scheme. Finally the method is applied to some propeller and rudder arrangements.

5.1 Grid Generation

The 3-D Euler solver called GBFLOW-MB [Natarajan and Kinnas 2003], is programmed so that the Euler equations can be solved in an (i,j,k)-ordered three dimensional cylindrical grid, where the indices (i,j,k) represent the axial, radial, and circumferential directions respectively, or in a three dimensional H-type grid, where the indices (i,j,k) represent the axial, the vertical, and the horizontal directions.

¹The current method is only using two blocks, but it is still called a multi-block method throughout the thesis

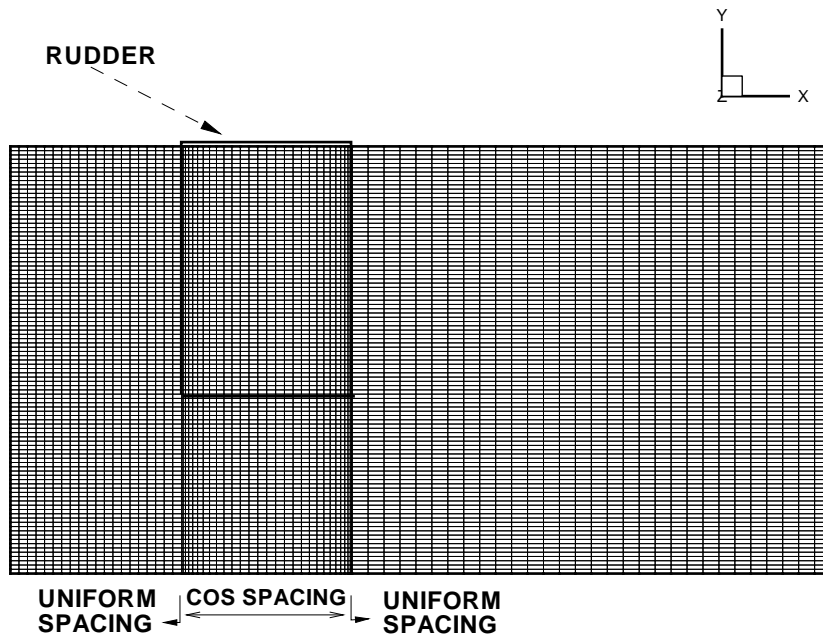


Figure 5.1: H-type grid showing the rudder along the meridional plane

Figure 5.1 shows the grid generated over the rudder at its meridional plane. Full-cosine spacing is used in the rudder section to capture the fluid flow around the leading edge and trailing edge more accurately. Uniform spacings are used in the domains upstream and downstream of the rudder, as shown in Figures 5.1 and 5.2 which show the H-type grid generated for a rudder with a NACA66 section and a 20% thickness to chord ratio ($t_{max}/C = 0.2$).

The H-type grid can also be adapted to more realistic rudder geometries like a horn-type rudder. Figures 5.3 and 5.4 show views of the H-type grid generated over a horn-type rudder with a NACA66 section and a 10% thickness to chord ratio.

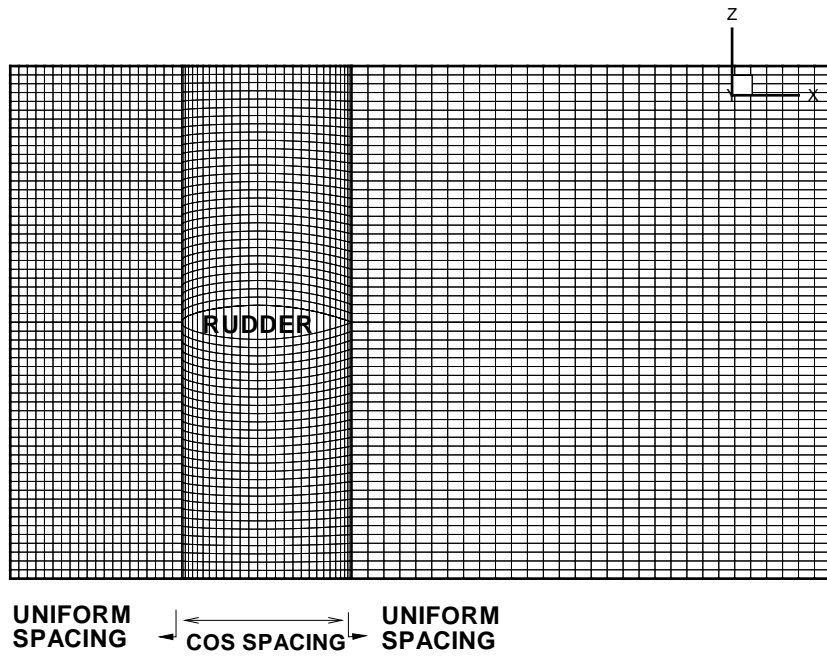


Figure 5.2: Top view of the H-type grid showing the rudder section and the spacing used over a hydrofoil like rudder with $t_{max}/C = 0.2$

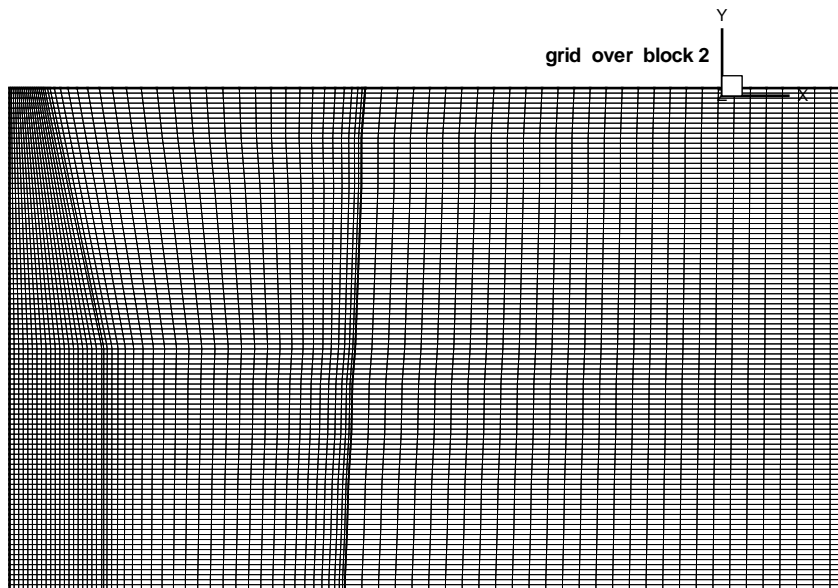


Figure 5.3: Side view H-type grid adapted over a horn-type rudder

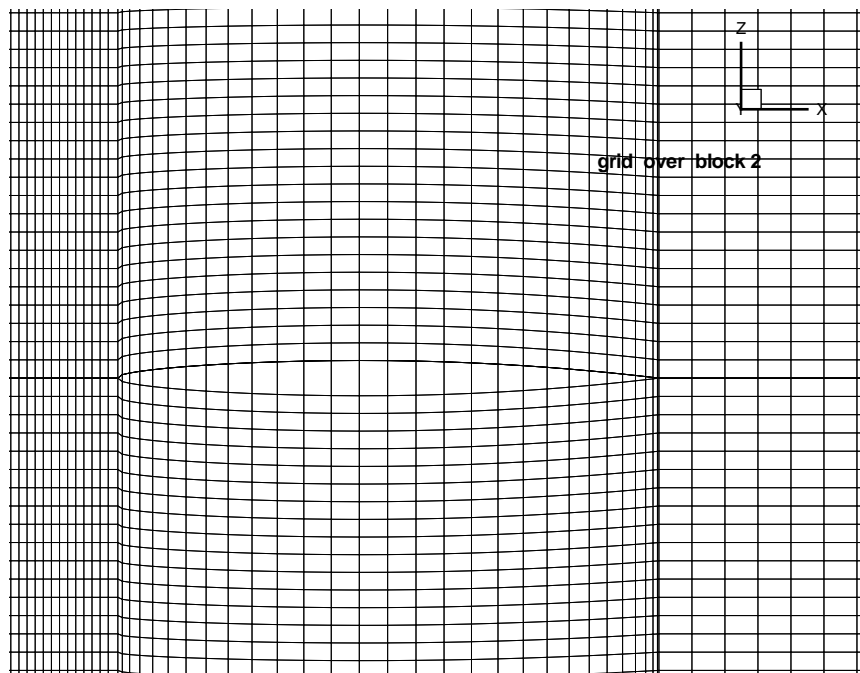


Figure 5.4: Top view of the H-type grid over the section of a horn-type rudder with a NACA66 section ($t_{max}/C = 0.1$)

5.2 Boundary Conditions

As in the case of the 3-D Euler solver, discussed in section 3.2.3, there are six boundaries in the block with the rudder, as shown in Figure 5.5. (a) The upstream boundary where the flow comes in, (b) the downstream boundary where the flow goes out, (c) the hull boundary at the top, (d) the outer boundary at the far field (or the solid boundary in the case of tunnel), (e) the repeat boundary, along the k -indices ($k = k_1, k_2, k_3$) forward of the leading edge and aft of the trailing edge of the rudder, (f) the body boundary over the rudder. The boundary conditions (a), (b), (c), (d) are the same as those defined in 3.2.3.

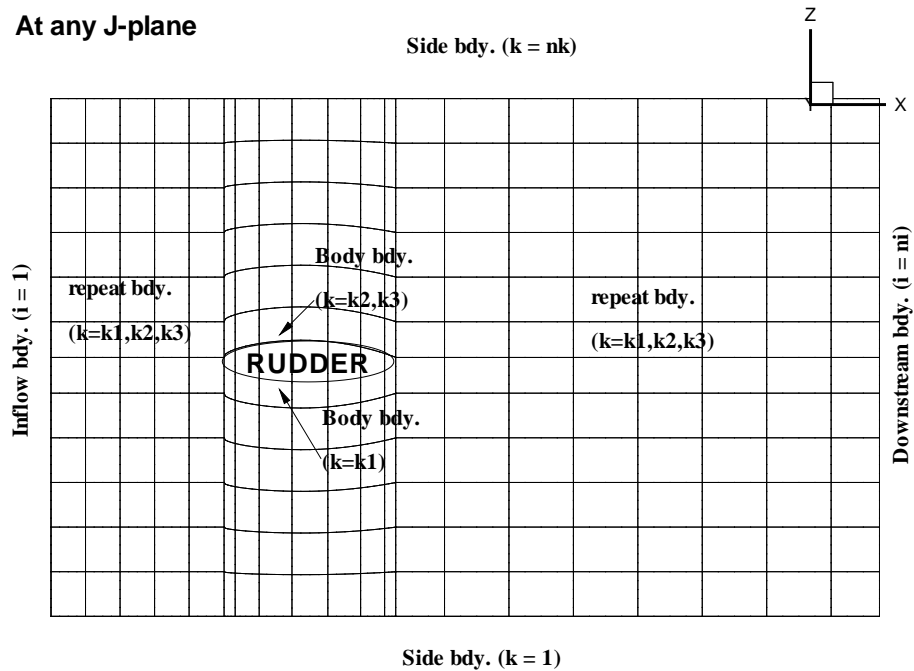


Figure 5.5: Boundary conditions on the H-type grid to compute the flow around the rudder

Three indices ($k = k_1, k_2, k_3$) are used as repeat indices. Two indices run over the

port side of the rudder ($k = k_2, k_3$) and one over the starboard side of the rudder ($k = k_1$). The repeat indices are treated through a pseudo cell technique as shown in Figure 5.6.

- *Repeat Boundary Condition*

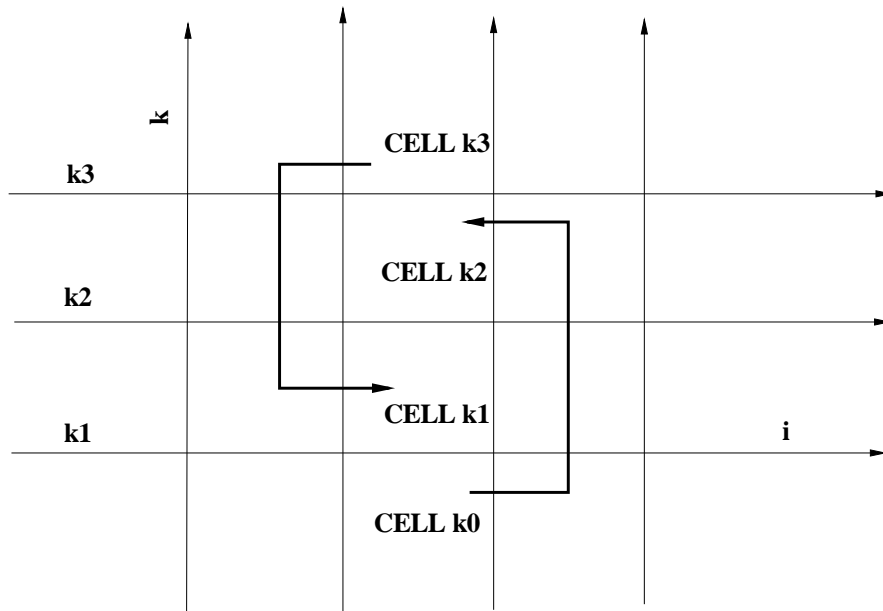


Figure 5.6: Pseudo cell treatment for the cells forward of leading edge and aft of the trailing edge along the repeat indices

The indices ($k = k_1, k_2$) are used to represent pseudo cells of zero thickness which are used to store the data from the neighbouring cells. While solving for the cell (k_0), the data of the cell (k_3) are transferred to the cell (k_1).

$$(u, v, w, p)_{k=k_1} = (u, v, w, p)_{k=k_3} \quad (5.1)$$

and similarly while solving for the cell ($k3$) the data from the cell ($k0$) are transferred to cell ($k2$)

$$(u, v, w, p)_{k=k2} = (u, v, w, p)_{k=k0} \quad (5.2)$$

- *Body Boundary Condition*

The rudder is treated as a solid boundary where the normal component of the velocity is set equal to zero, and where the derivatives of the other velocity components and of the pressure with respect to the direction normal to the rudder surface are taken equal to zero.

$$\frac{\partial(p)}{\partial n} = 0 \quad (5.3)$$

$$\vec{q} \cdot \vec{n} = 0 \quad (5.4)$$

$$\vec{q}_t = \vec{q} - \vec{q}_n \quad (5.5)$$

$$\frac{\partial(\vec{q}_t)}{\partial n} = 0 \quad (5.6)$$

The cells beneath the bottom tip of the rudder, which has non-zero cell volume, are considered as flow-through fluid cells in the 3-D Euler solver.

5.2.1 Fourth-order Smoothing

The three-dimensional Euler solver employs the artificial dissipation (or viscosity) to improve the stability of the numerical method Anderson [1995]. The second and fourth order dissipations, μ_2 and μ_4 , respectively, are scaled by Δt .

$$\mathbf{U}_{(i,j,k)}^{n+1} = \mathbf{U}_{(i,j,k)}^n + \sum_{c=A,B,C,\dots,H} (\delta \mathbf{U}_{(i,j,k)}^n)_c + \Delta t (\mu_2 - \mu_4) \quad (5.7)$$

where A, B, C, \dots, H are the neighbouring 8 cells to the grid point (i, j, k) . The fourth order dissipation coefficient is defined as,

$$\mu_4 = \sigma_4 (\delta_{iiii} \mathbf{U}_{(i,j,k)}^n + \delta_{jjjj} \mathbf{U}_{(i,j,k)}^n + \delta_{kkkk} \mathbf{U}_{(i,j,k)}^n) \quad (5.8)$$

where, Δt is the pseudo time step and δ_{iiii} is the fourth order finite central difference operator,

$$\delta_{iiii} = ()_{i-2} - 4()_{i-1} + 6()_i - 4()_{i+1} + ()_{i+2} \quad (5.9)$$

As shown in Figure 5.7, the artificial dissipation is not applied along the $k - index$ direction on the indices close to the rudder section. The operator δ_{kkkk} when applied over grid lines of constant value of $k - index$ close to the rudder, which computes a weighted average based on the values on either side of the rudder, an erroneous value of artificial dissipation is obtained, since the artificial dissipation on one side of the rudder is not influenced by the flow characteristics on the other side of the rudder. To avoid such discrepancies the artificial dissipation is applied only along the $i - index, j - index$ directions and for $k - index$ lines which are 1 or 2 indices away from the surface of the rudder. An alternative, more accurate way would be to use backward or forward finite difference schemes. However, this would increase the complexity of the code without significant effect on the convergence of the Euler solver.

Note: numbers in circles are weighting coefficients of finite central difference of fourth order

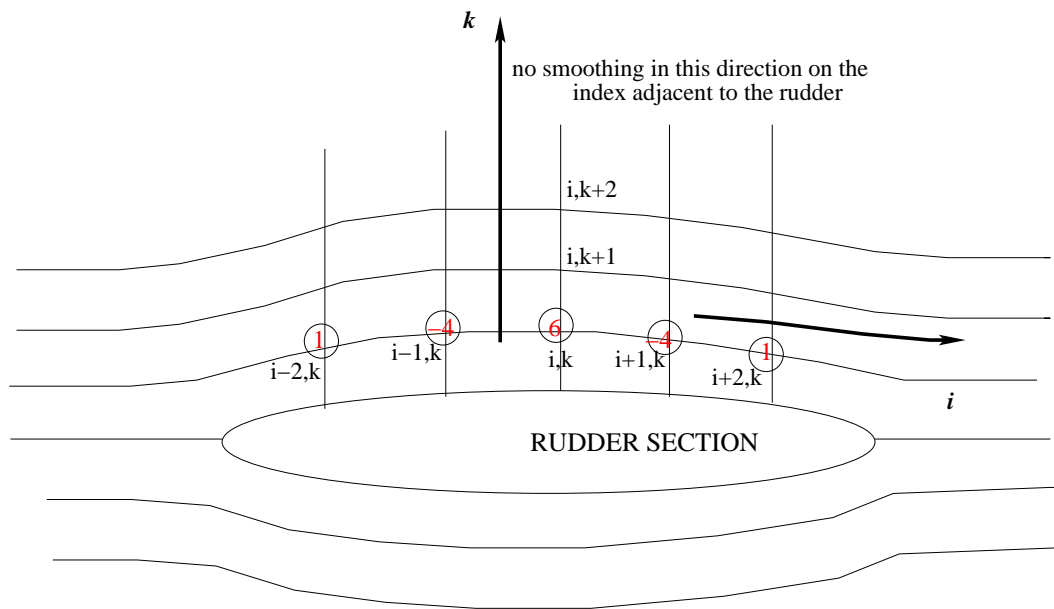


Figure 5.7: Applying the 4th-order smoothing along the indices close to the rudder section

5.3 Results for Flow Around the Rudder

This section describes results from the 3-D Euler solver in the case of a rudder inside a tunnel. Each of the related runs required 20 hours of CPU time on a Compaq Professional Workstation XP1000. A typical, though simplified, rudder geometry with a NACA66 section and a 20% thickness to chord ratio is shown in Figure 5.8. Figure 5.9 shows the axial velocity contours at the center plane of the grid. The accelerated flow at about midchord of the rudder can be seen in this figure. The pressure contours at the center plane of the grid are shown in Figure 5.10, where the pressure drop (stagnation point) at the leading edge of the rudder is evident. The oscillations in the results close to the tip of the rudder, as shown in Figures 5.9 and 5.10, could be due to the fact that the rudder thickness at the tip is non-zero. The cells beneath the tip of the rudder is treated as a flow-through fluid cells in the 3-D Euler solver. These inaccuracies at the tip region require further studies. Figures 5.11 and 5.12 show the axial velocity contours and tangential velocity contours along with streamlines over a rudder section at a spanwise location ($Y = 1.0$) close to the top wall of the tunnel. The contours show some velocities within the region of the rudder, which is due to plotting error.

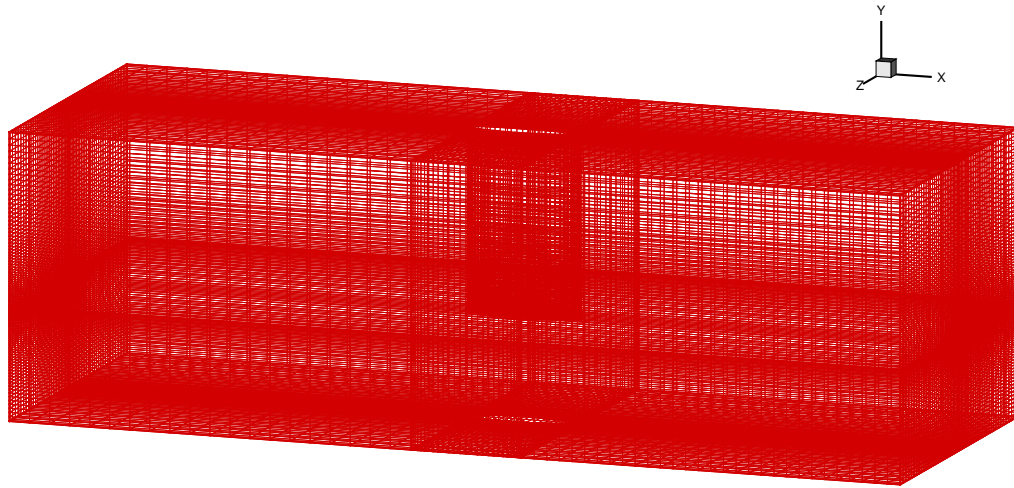


Figure 5.8: Three-dimensional grid used to model the rudder with 20% thickness ratio and NACA66 thickness form

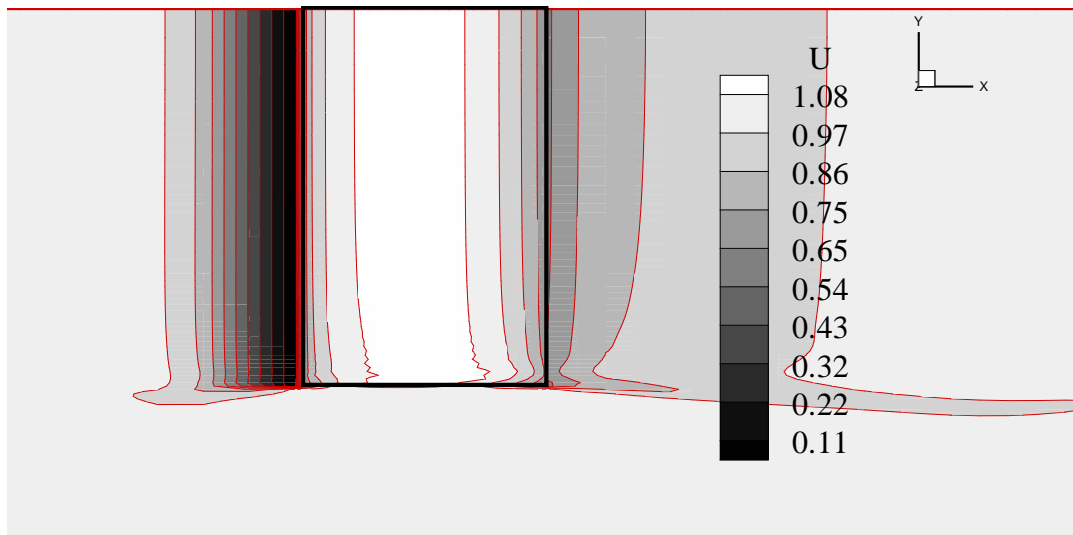


Figure 5.9: Axial velocity contours at the center plane of the grid for a rudder inside a tunnel

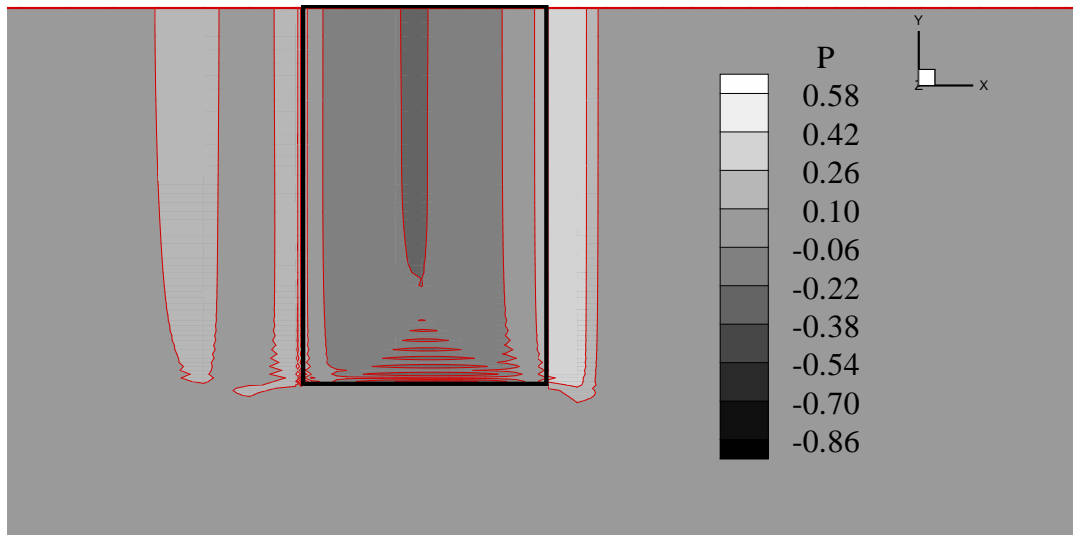


Figure 5.10: Pressure contours at the center plane of the grid for a rudder inside a tunnel

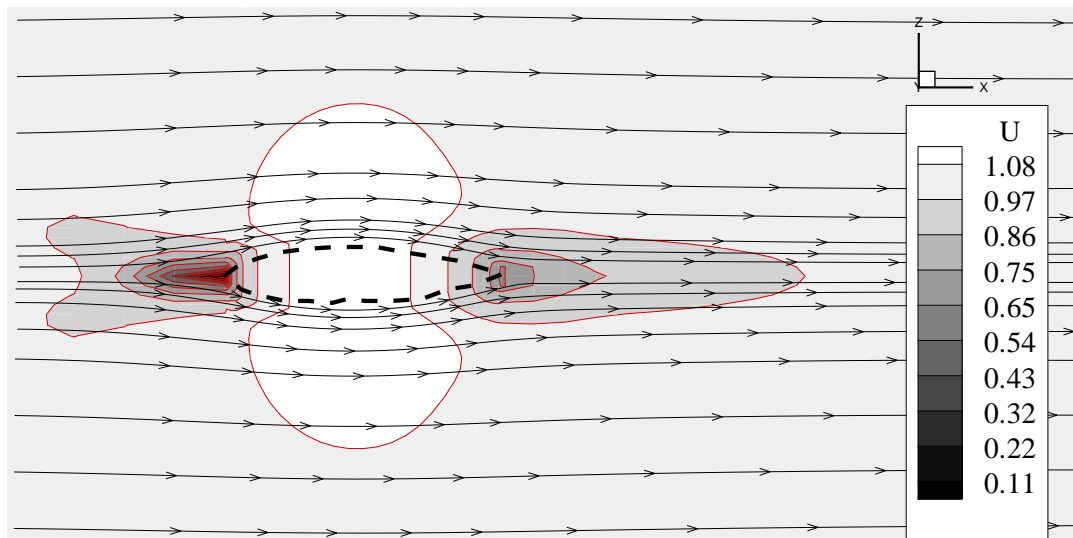


Figure 5.11: Axial velocity contours along with stream lines at a rudder section located at $y = 1.0$ (looking from the top wall of the tunnel) close to the top wall of the tunnel. The rudder section is also shown. The values inside the rudder section is due to plotting error.

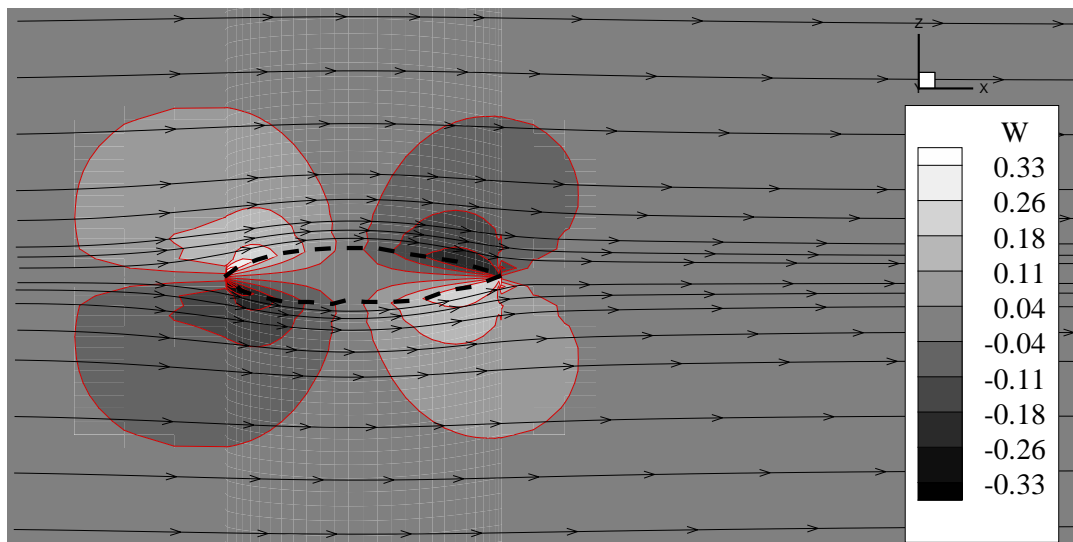


Figure 5.12: Tangential velocity contours along with streamlines at a rudder section located at $y = 1.0$ (looking from the top wall of the tunnel) close to the top wall of the tunnel. The rudder section is also shown. The values inside the rudder section is due to plotting error.

5.4 Validation tests

Results from the 3-D Euler solver applied to the rudder inside a tunnel are validated versus those from a low order potential based BEM. In the BEM solver, the effects of the tunnel on the rudder are included iteratively, as described in the following section.

5.4.1 Inclusion of the Tunnel Effects in the BEM

The flow around the rudder is assumed to be incompressible, inviscid and irrotational, hence the perturbation potential, ϕ , can be defined as :

$$\vec{q} = \vec{U}_{in} + \nabla\phi \quad (5.10)$$

The tunnel and hydrofoil are modeled separately and the effect of one on the other is dealt iteratively, as described in [Kinnas et al. 1998b]. The effect of the top wall of the tunnel is modeled by imaging the ruder and the other walls, as shown in Figure 5.13.

The BEM integral equation for the hydrofoil including the tunnel effects is given by:

$$2\pi\phi = \int_{S_B} \left[\phi \frac{\partial}{\partial n} \frac{1}{r} - \frac{\partial\phi}{\partial n} \frac{1}{r} \right] dS + \int_{S_W} (\Delta\phi) \frac{\partial}{\partial n} \frac{1}{r} dS + 4\pi\phi_T \quad (5.11)$$

Similarly, the BEM integral equation for the tunnel including the hydrofoil effect is given by:

$$2\pi\phi = \int_{S_T} \left[\phi \frac{\partial}{\partial n} \frac{1}{r} \right] dS + 4\pi\phi_H \quad (5.12)$$

where, ϕ_H and ϕ_T are the perturbation potential on hydrofoil and tunnel respectively.

The kinematic boundary condition on the tunnel walls requires the flow to be tangent to the tunnel wall. Thus, the source strengths, $\frac{\partial\phi}{\partial n}$, are known in terms of the inflow velocity \vec{U}_{in} :

$$\frac{\partial\phi}{\partial n} = -\vec{U}_{in} \cdot \vec{n} = 0; \text{ (on the tunnel walls)} \quad (5.13)$$

where \vec{n} is the normal vector on the tunnel surface pointing into the fluid.

The above integral equation is discretized with constant strength dipoles and sources distributed over quadrilateral panels on the rudder and tunnel surface. The unknowns ϕ_H and ϕ_T are determined by inverting the resulting system of equations as shown below:

$$\left[\begin{array}{c|c} A_{H-H} & A_{H-T} \\ \hline A_{T-H} & A_{T-T} \end{array} \right] \left[\begin{array}{c} \phi_H \\ \phi_T \end{array} \right] = \left[\begin{array}{c} B_H \\ B_T \end{array} \right] \quad (5.14)$$

The iterative technique employed solves the hydrofoil and the tunnel problem separately. The hydrofoil problem is solved as,

$$A_{H-H} \cdot \phi_H = B_H - A_{H-T} \cdot \phi_T \quad (5.15)$$

similarly, the tunnel problem is solved as,

$$A_{T-T} \cdot \phi_T = B_T - A_{T-H} \cdot \phi_H \quad (5.16)$$

In the first iteration, the potential on the tunnel walls is considered to be 0 (i.e. $\phi_T = 0$). As the iterations progress, the hydrofoil-tunnel interaction is felt on the loading of the hydrofoil. The iterations are performed till the loading on the hydrofoil converges within a tolerance of 10^{-3} (usually 3 – 4 iterations suffice).

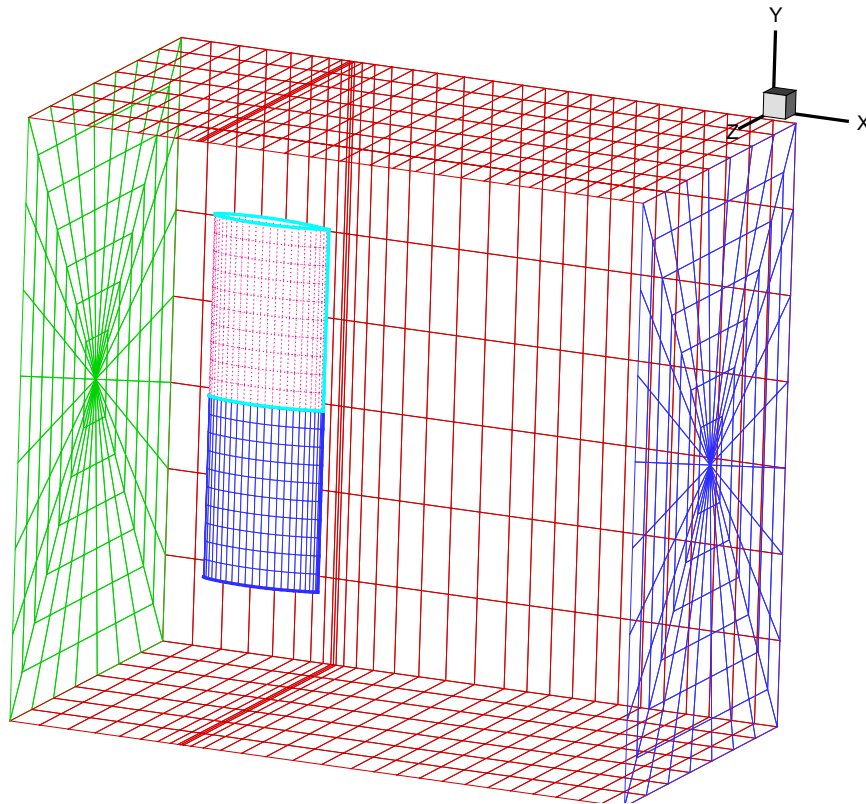


Figure 5.13: Tunnel and hydrofoil, including the images with respect to the top wall (not shown), as modeled through the panel method

5.4.2 Comparison of the Results from the Euler and the Panel Method

The flow over a rudder inside a rectangular tunnel of width, $W = 2.0$ and height, $H = 1.66$, (the units are normalized with the span of the rudder as, $S = 1$) is solved using both the methods. The tunnel along with the hydrofoil, and their images as used in the panel method are shown in Figure 5.13.

The pressure distributions over the rudder are obtained using the panel method and the 3-D Euler solver, and are compared in Figure 5.14, at various locations along the span of the rudder. The rudder has a NACA66 thickness form with 20% thickness

to chord ratio. In Figures 5.15 and 5.16, the pressure distributions obtained from the two methods are compared at different sections along the span of the rudder. Similar comparisons for a rudder with 10% thickness to chord ratio are shown in Figures 5.17 and 5.18.

The pressure distributions predicted from 3-D Euler solver compare reasonably well with those obtained from the panel method, except at locations close to the leading edge, especially in the case of a 10% thick foil. This discrepancy could be due to the change in the aspect ratio of the cells close to the leading edge. By using half-cosine spacing or a spacing with an expansion ratio in the region forward of the rudder, the flow at the leading edge effect could be captured more accurately. Further study is needed to reconcile the significant inaccuracies at the leading edge, as well as the overall accuracy of the Euler solver.

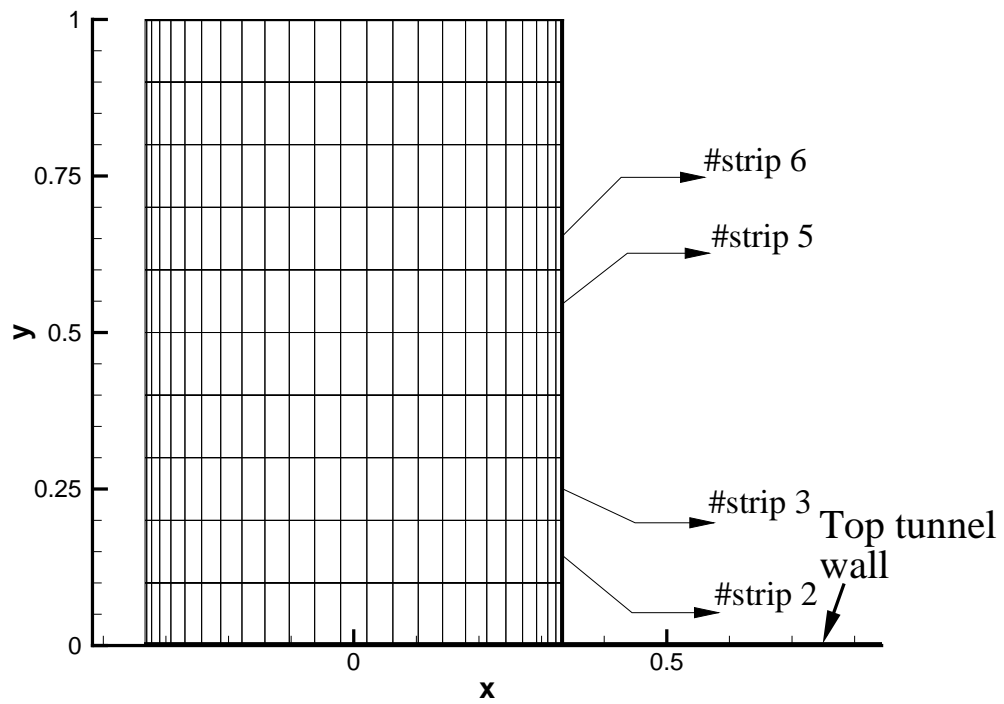


Figure 5.14: Pressure distributions obtained from the 3-D Euler solver and the panel method results are compared in the figures that follow at the shown locations. $y = 0$ is the upper tip (close to the top wall) and $y = 1$ is lower tip of the rudder

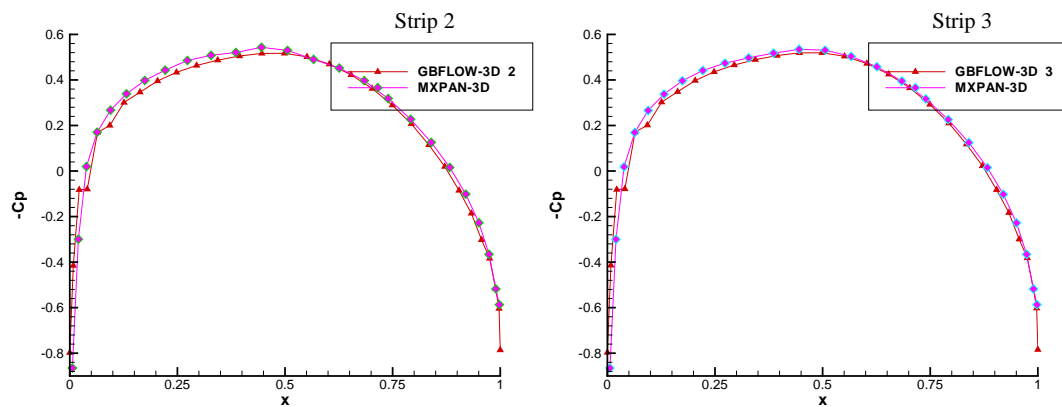


Figure 5.15: Comparison of pressure distributions obtained from the 3-D Euler solver and the panel method for a rudder with $t/C = 0.2$, at sections close to the top wall of the tunnel

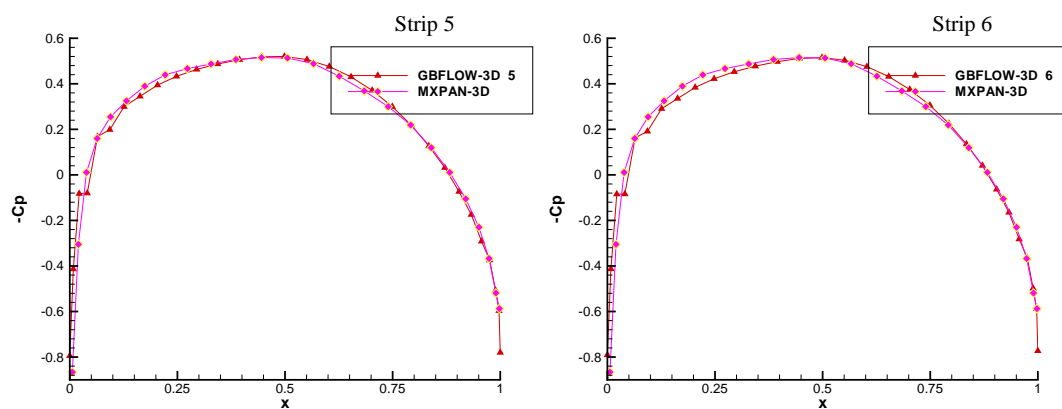


Figure 5.16: Comparison of pressure distributions obtained from the 3-D Euler solver and the panel method for a rudder with $t/C = 0.2$, at sections close to the bottom of the rudder

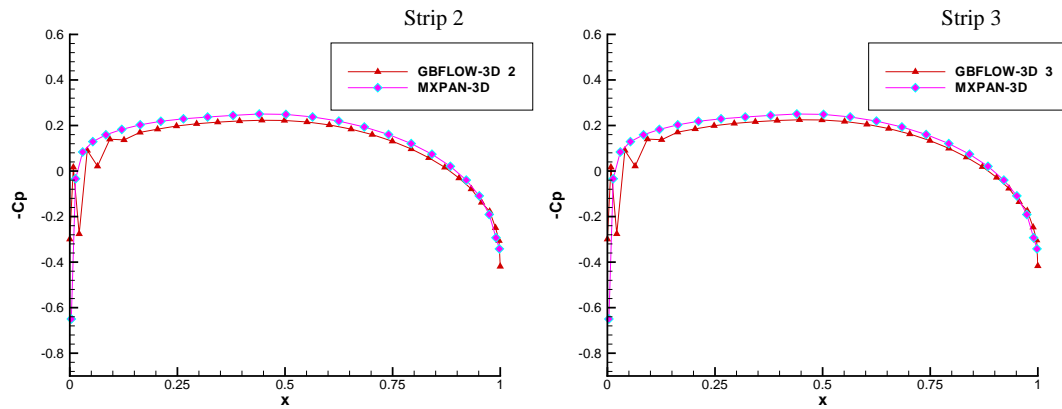


Figure 5.17: Comparison of pressure distributions obtained from the 3-D Euler solver and the panel method for a rudder with $t/C = 0.1$, at sections close to the top wall of the tunnel

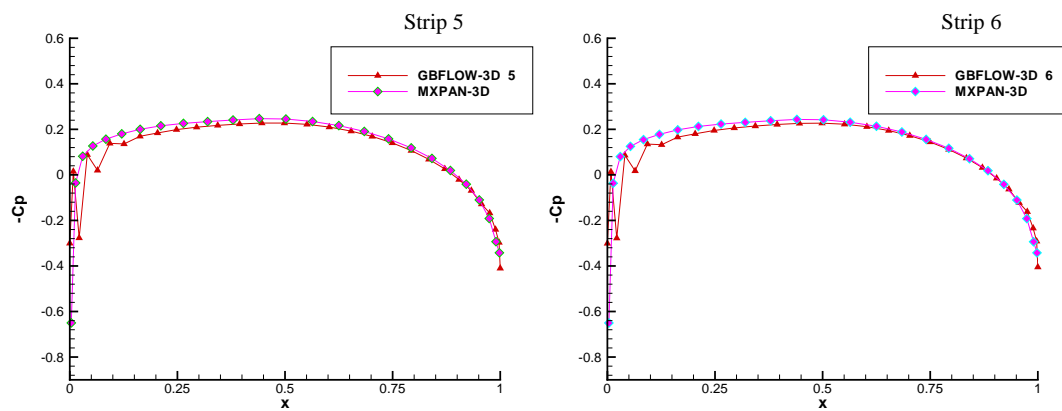


Figure 5.18: Comparison of pressure distributions obtained from the 3-D Euler solver and the panel method for a rudder with $t/C = 0.1$, at sections close to the bottom of the rudder

5.5 Multi-Block Method

As already mentioned in Section 5.1, the propeller-rudder interaction will be evaluated by using the multi-block approach in the Euler solver. In this approach, the flow around the propeller is computed in one block and the flow around the rudder is computed in another block, as shown in Figure 5.19. Overlapping non-matching grids are used in the two blocks. The overlapping zone, common to the two blocks, has been found to improve the convergence of the iterative process between the two blocks. The information on the common boundaries of the two blocks is exchanged through interpolations. The code for the present method is named GBFLOW-MB [Natarajan and Kinnas 2003].

5.5.1 Iterative Process to Compute the Effective Wake

The three components in the iterative process are the propeller solver (MPUF-3A), the 3-D Euler solver (GBFLOW-MB) for block-1 in which the propeller is represented with body forces and, the 3-D Euler solver for block-2 in which the rudder is modeled as a solid boundary. The iterative process starts with the propeller analysis using the nominal wake as inflow. Using the computed propeller loading, the body forces which represent the propeller in the Euler equations are calculated. The 3-D Euler solver computes the velocity flow field in block-1 by using the body forces found in the previous step. The effective wake to the propeller is then computed by subtracting the propeller induced velocities from the total velocity field. The predicted total velocity field and pressures in block-1, are now interpolated and the velocities and pressures are calculated at the grid points of the inflow boundary for block-2. With these interpolated inflow conditions, the flow field around the rudder is computed in

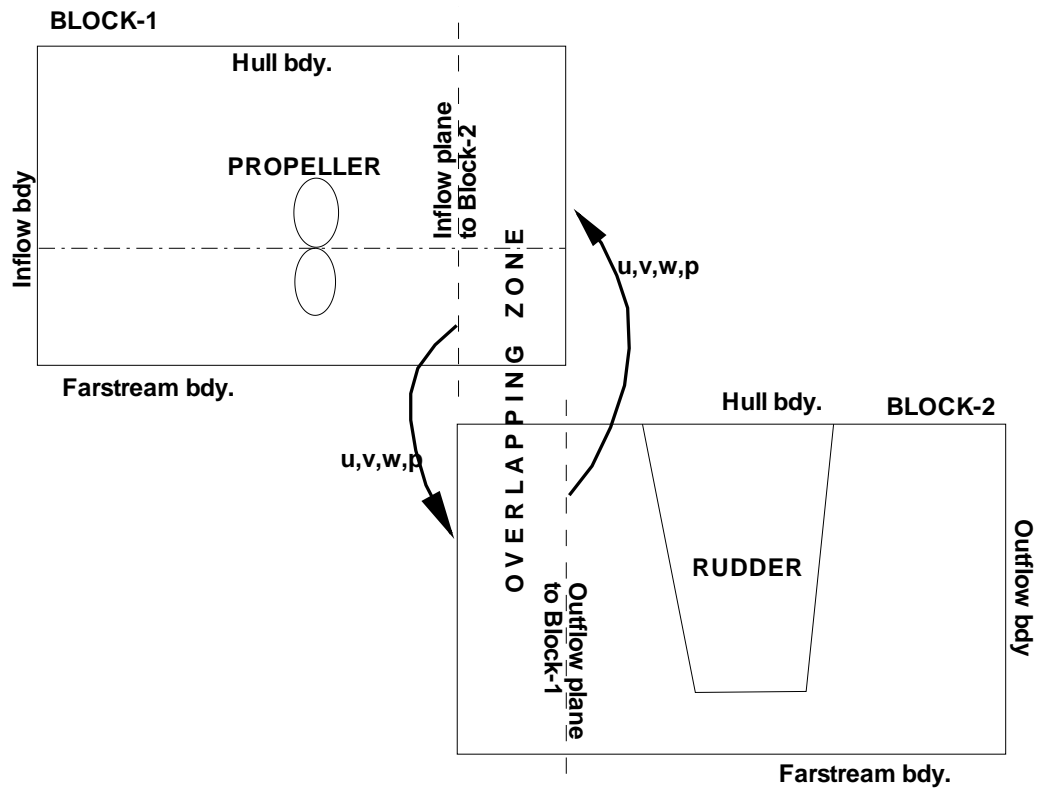


Figure 5.19: The two blocks used in the 3-D Euler solver

block-2. The predicted total velocity field and pressures in block-2 are interpolated and the outflow pressures for block-1 are calculated. The VLM solver (MPUF-3A) uses the new effective wake as the new inflow to compute the updated propeller loading. The iterative process continues until the propeller loading converges within a specified tolerance. It has been found that the iterative process usually converges within five to seven iterations between the two blocks. The number of iterations increases with decreasing distance between the propeller and the rudder.

5.5.2 Interpolation Scheme

The two blocks need to communicate with each other in order to determine each one's effect on the other. A cylindrical grid is used in block-1 in order to accommodate the representation of the propeller by body forces, whereas an H-type adapted grid is used to model the rudder in block-2. The two meshes are shown in Figures 5.20 and 5.21. To transfer the data from one block to the other, the values (u, v, w, p) need to be interpolated on the boundaries of the overlapping zone.

In order to obtain the total velocity components and pressures at the H-type grid points from the values at the cylindrical grid points linear interpolation is performed. To obtain the pressures at the cylindrical grid points from the H-type grid points, quadratic interpolation is performed.

As shown in Figure 5.22, the values at a grid point at which the data have to be interpolated is determined from the cell nodal values, in the case of linear interpolation (i.e. from block-1 to block-2). The interpolation along the circumferential direction is performed first, to determine the values at two radial locations, a and b . With these values, a linear interpolation along the radial direction is used to determine the value

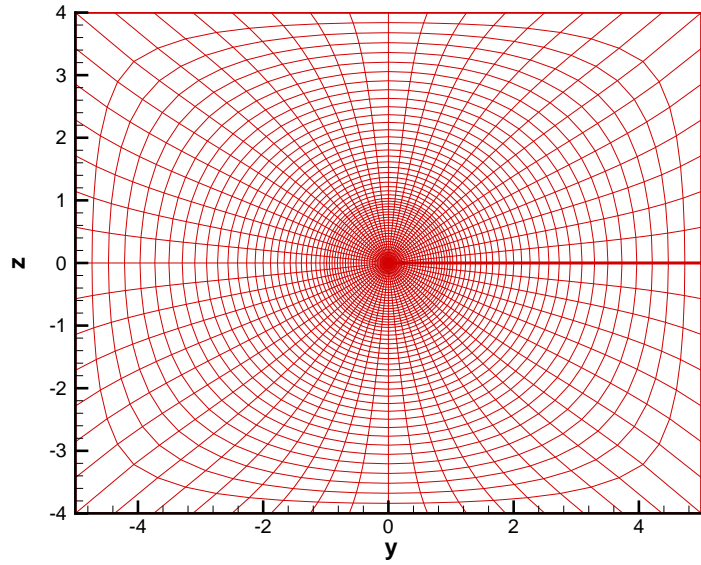


Figure 5.20: Cylindrical grid used in block-1 at the inflow plane for block-2 (as shown in Figure 5.19)

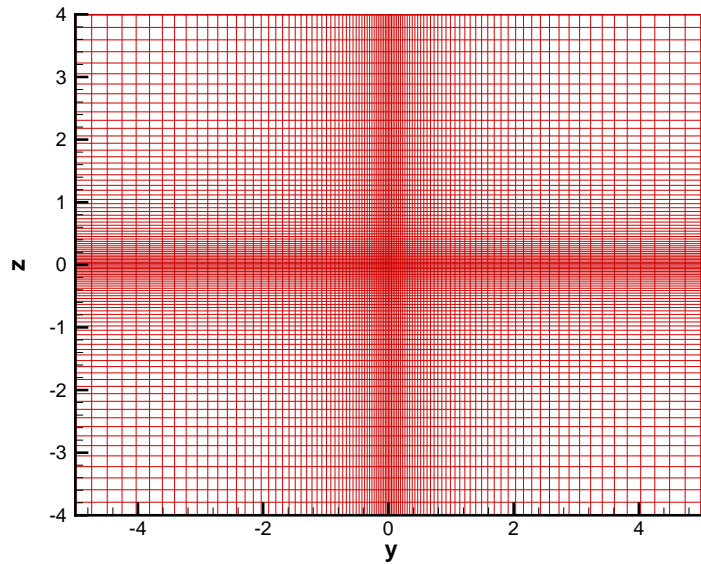
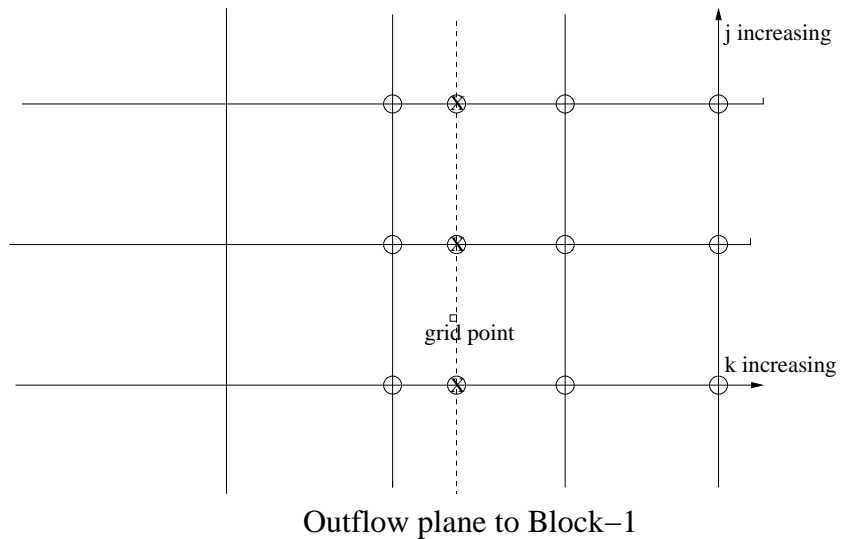
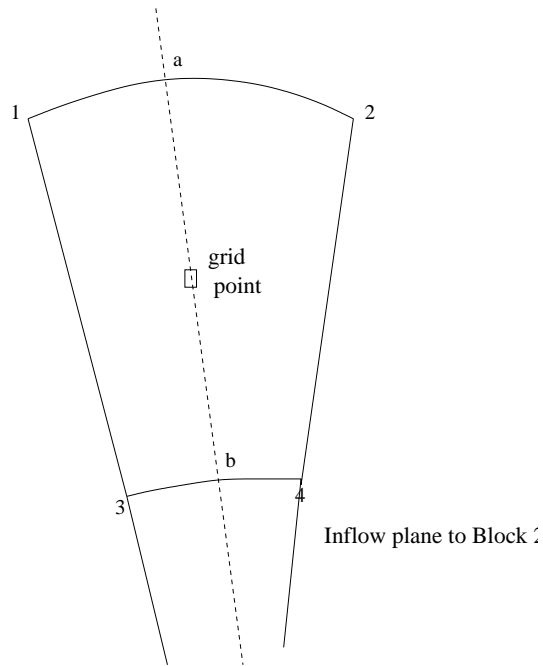


Figure 5.21: H-type grid used in block-2 at the outflow plane for block-1 (as shown in Figure 5.19)



- the value at these grid points are used to interpolate along k- direction on to ⊗ these points
- ⊗ the value at these points are used to interpolate along j- direction to determine the value at the control point

Figure 5.22: Interpolation technique used to transfer data from block-1 to block-2 (top) and block-2 to block-1 (bottom)

at the point.

In the case of determining the values at a point using quadratic interpolation (i.e. from block-2 to block-1), the interpolation is performed from the neighbouring cell values along both j and k -indices, as shown at the bottom of Figure 5.22.

5.5.3 Validation of the Interpolation scheme

Since the interpolations are performed between two non-matching meshes, the interpolation error must be quantified. Moreover, these interpolations are performed at each iteration back and forth between the two blocks. The interpolation error could propagate within each iteration between block-1 and 2, and could thus affect the convergence of the iterative process, or the accuracy of the results.

In this section, the interpolation schemes are validated using analytical functions. An analytical function $f(y, z) = \sqrt{y^3 + z^3} + 1$ is assumed in the H-type grid, as shown in Figure 5.23. Interpolations are performed to recover the same function in the cylindrical grid. The recovered function is shown in Figure 5.24. The local interpolation error is defined as:

$$\Delta f = f_{cyl} - f_{h-type} \quad (5.17)$$

$$\epsilon = \frac{\Delta f}{f} \quad (5.18)$$

and the error is plotted in Figure 5.25. The magnitude of error is of the order 10^{-3} .

The interpolation scheme is also tested for the case of transfer of data from block-1 to block-2 with the same cubic function, $f(y, z) = \sqrt{y^3 + z^3} + 1$. The cubic function is assumed in the cylindrical grid. Interpolations are performed to recover the same function in the H-type grid. The function recovered is shown in Figure 5.26. The

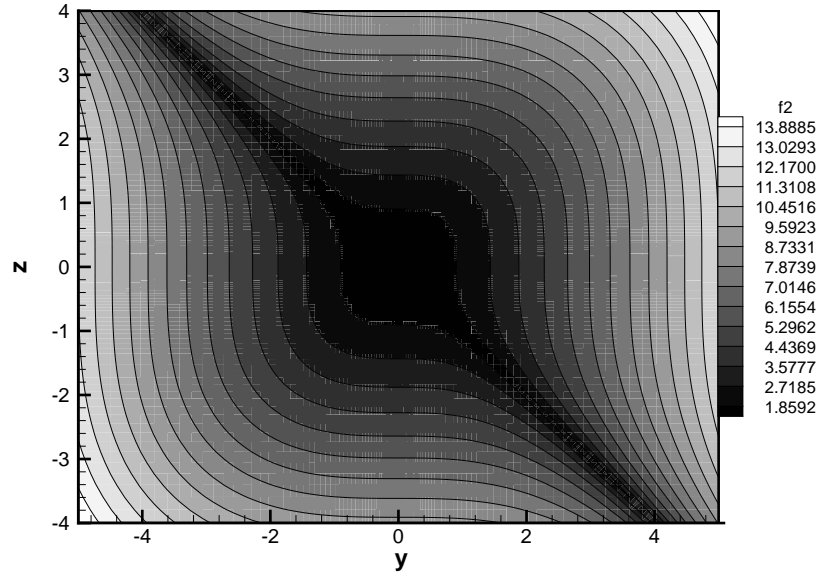


Figure 5.23: Analytical function assumed on the H-type grid (shown in Figure 5.21)

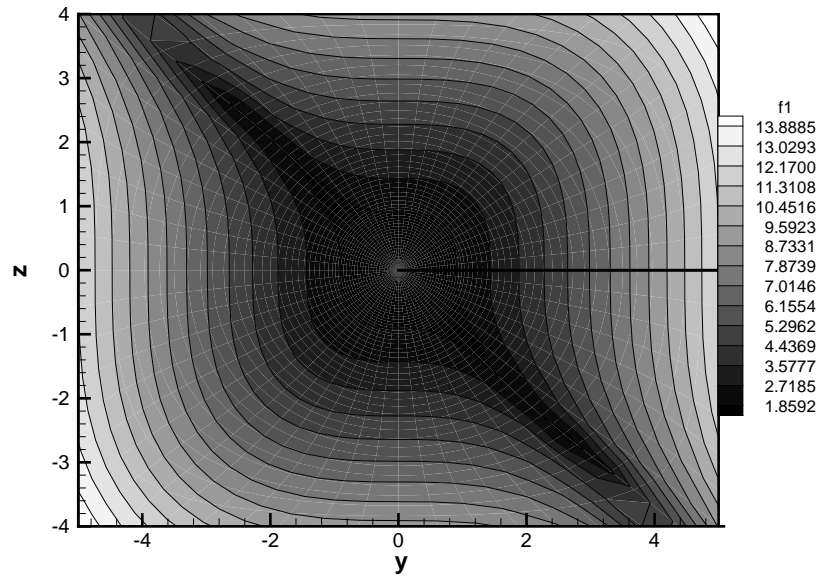


Figure 5.24: Analytical function recovered on the cylindrical grid (shown in Figure 5.20) after performing interpolations from values in the H-type grid

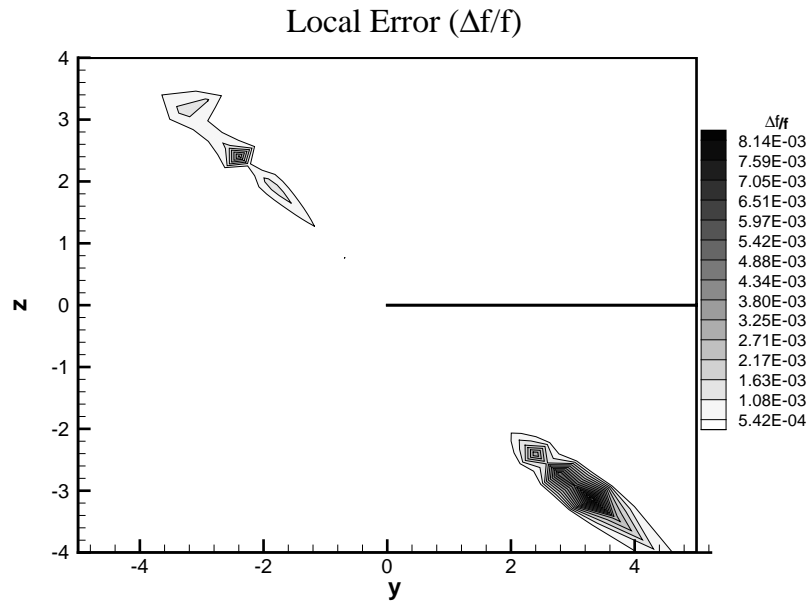


Figure 5.25: Local relative error for a function, $f(y, z) = \sqrt{y^3 + z^3} + 1$

local relative interpolation error is shown in Figure 5.27. It can be seen that the interpolation error is high along the corners of the domain, due to the coarse grids used in the cylindrical grid. Nevertheless, the magnitude of the error over most of the domain is in the order of 10^{-3} .

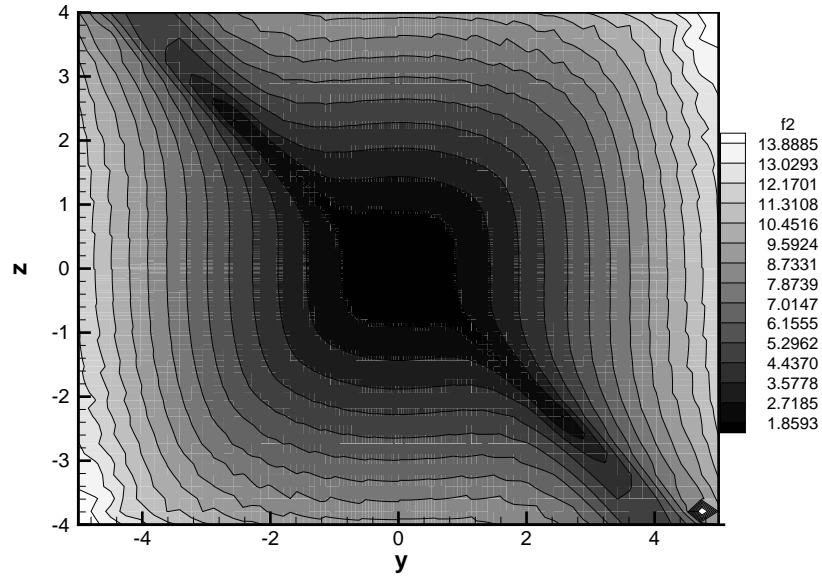


Figure 5.26: Analytical function recovered on the H-type grid (shown in Figure 5.21) after performing interpolations from values in the H-type grid

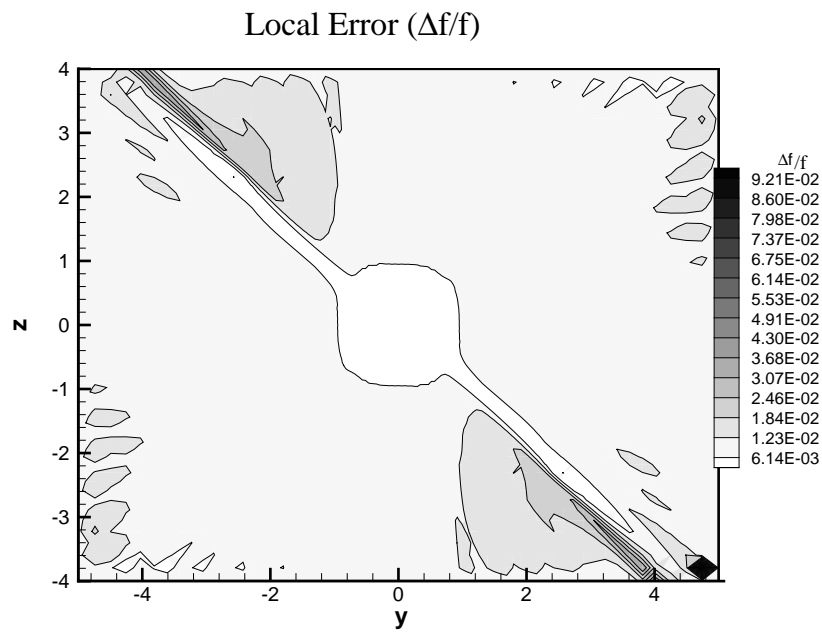


Figure 5.27: Local relative error for a function, $f(y, z) = \sqrt{y^3 + z^3} + 1$

5.6 Results of Propeller-Rudder Interaction

The propeller-rudder interaction is performed for a straight rudder with a NACA66 thickness form and 20% thickness to chord ratio, and a horn-type rudder with a NACA00 thickness form and a 20% thickness to chord ratio.

5.6.1 Results for a Straight Rudder

This subsection describes the results from an iterative run between MPUF-3A and GBFLOW-MB, to determine the propeller-rudder interaction for a straight rudder with a NACA66 thickness form and 20% thickness to chord ratio. Uniform inflow is assumed in predicting the propeller forces in MPUF-3A. In GBFLOW-MB, the top boundary is treated as a flat hull, and the side and bottom boundaries are treated as far-stream boundaries. The solution usually requires three such iterations for the convergence of propeller forces within a tolerance of 10^{-3} . The computational domain used in the 3-D Euler solver is shown in Figure 5.28. Figure 5.29 shows the tangential velocity contours along the center plane in both the blocks. From this figure it can be seen that the vortical flow induced by the propeller is cancelled downstream of the rudder trailing edge. In Figure 5.30, the axial velocity distribution is shown along the center plane, where the effect of the rudder is clearly shown. The presence of the rudder causes the flow to accelerate past the rudder.

Figure 5.31 shows the effective wake predicted at a plane located at $X_{eff} = -0.3$. The 3-way interaction between the inflow, the propeller and the rudder has been accounted for in the evaluation of the effective wake. The presence of the rudder causes a decrease in the axial velocity at an upstream axial location (blockage effect of the rudder).

The relative local error in the flow field is studied at an axial location ($X = 0.3$) in the overlapping zone between block-1 and 2. Figure 5.32 shows the relative error in the axial velocity, and Figure 5.33 shows the relative error in the tangential velocity. The relative local error is defined as,

$$\Delta f = f_{block1} - f_{block2} \quad (5.19)$$

$$\epsilon = \frac{\Delta f}{f_{block2}} \quad (5.20)$$

with f being the calculated quantity (u, v, w, p). The magnitude of the error is in the order 10^{-3} over most of the domain of computation.

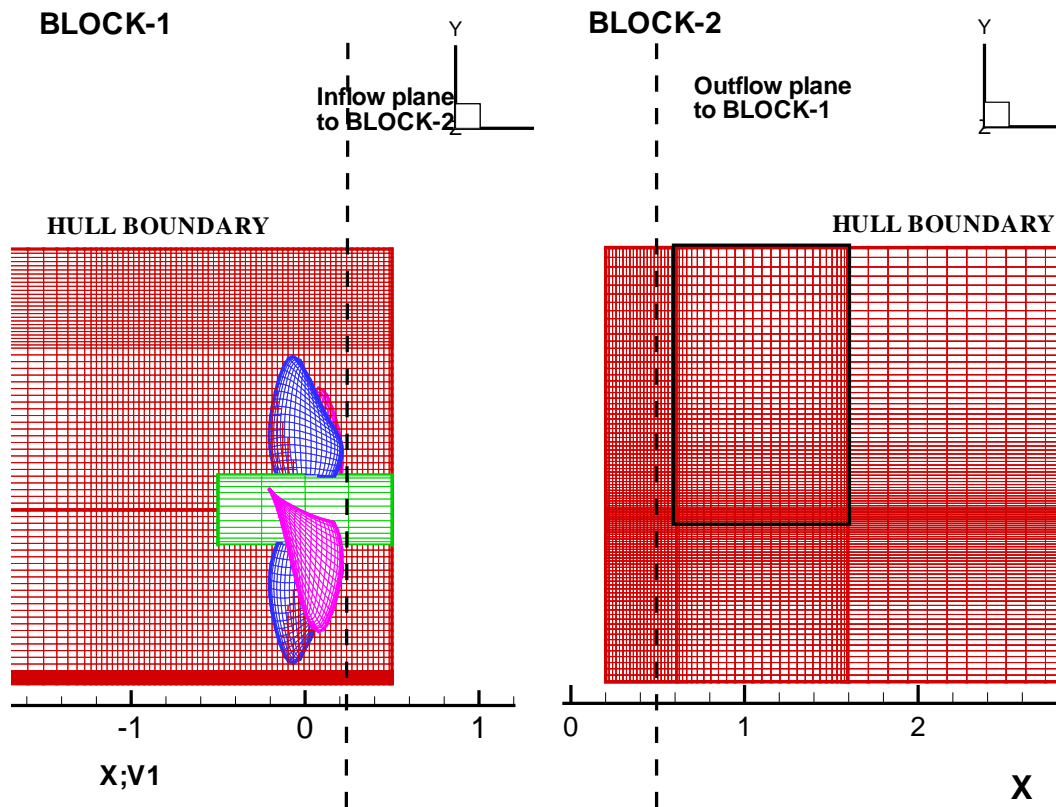


Figure 5.28: 3-D Euler solver grid showing rudder with NACA66 section and 20% thickness ratio

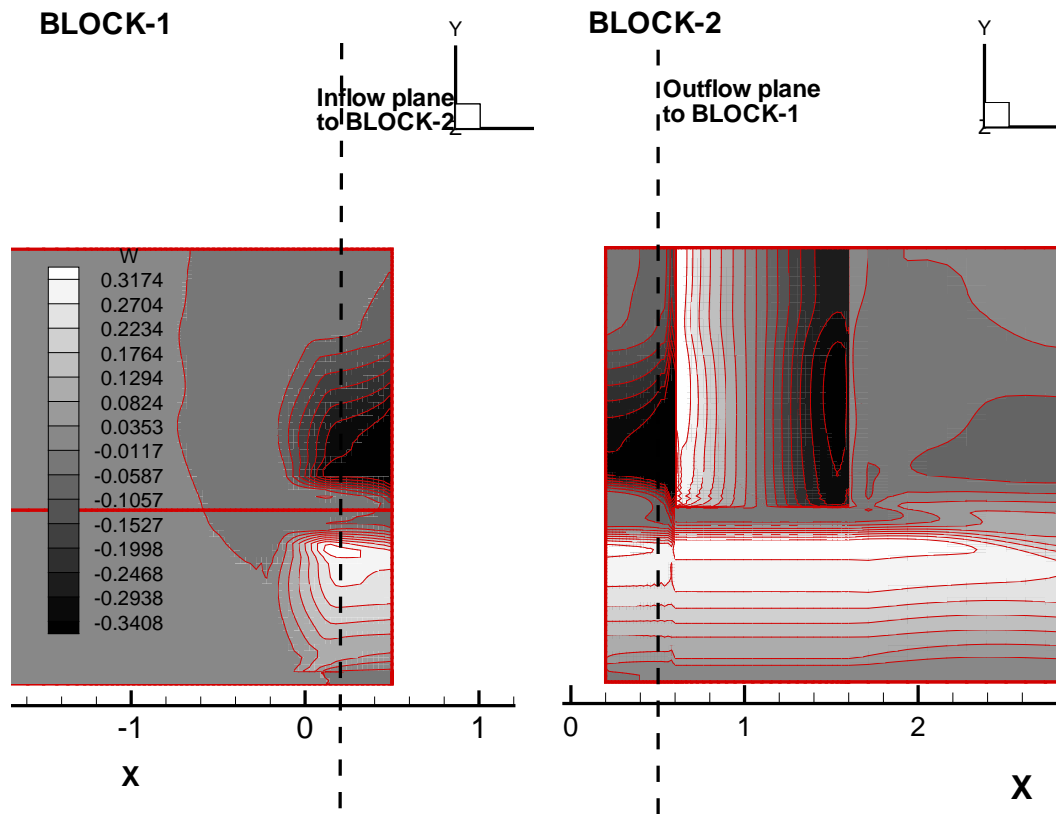


Figure 5.29: Tangential velocity contours on the center plane of Block-1 and 2 for a straight rudder

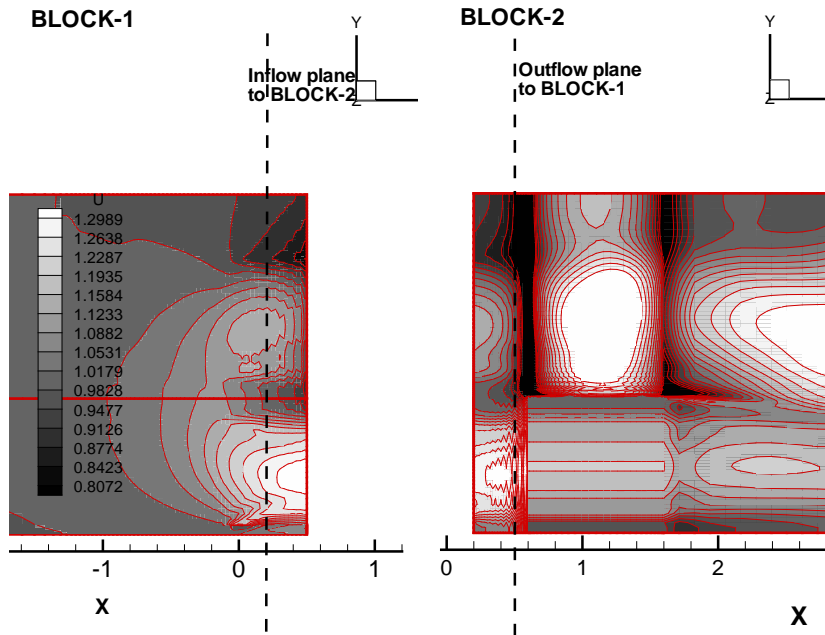


Figure 5.30: Axial velocity contours on the center plane of Block-1 and 2 for a straight rudder

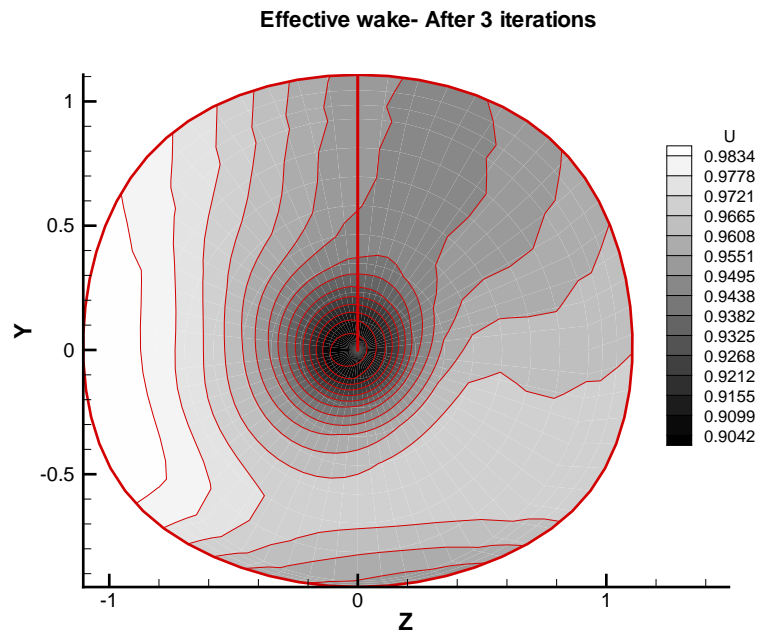


Figure 5.31: Effective wake predicted after 3 iterations with the propeller-rudder interaction

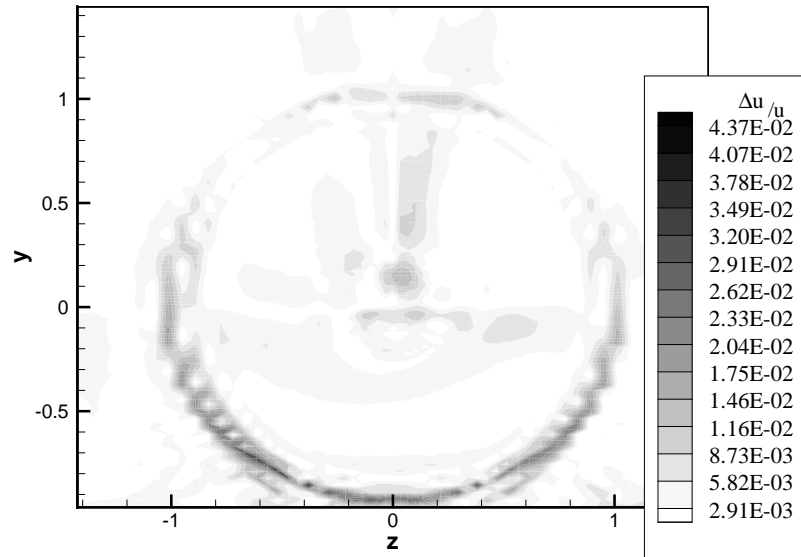


Figure 5.32: Local relative error in axial velocity at a plane $X = 0.3$ in the overlapping zone

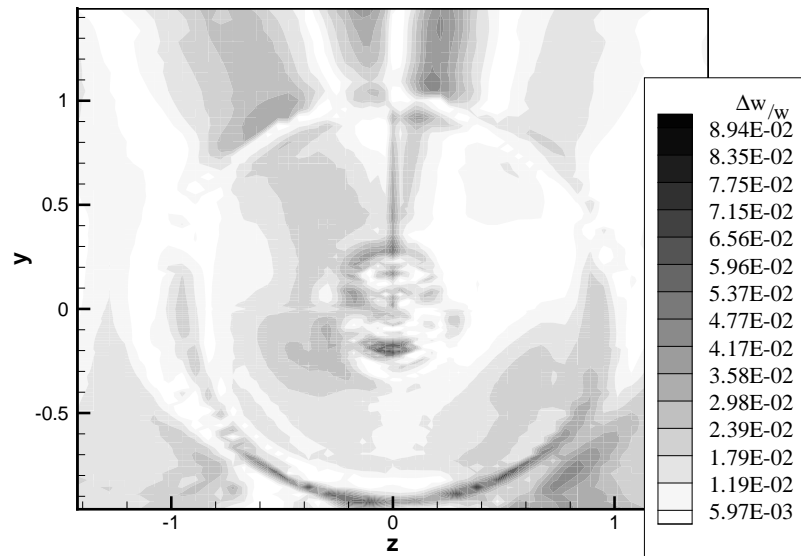


Figure 5.33: Local relative error in tangential velocity at a plane $X = 0.3$ in the overlapping zone

5.6.2 Results for a Horn-type Rudder

This subsection describes the results from applying the iterative method on a horn-type rudder with a NACA0020 thickness form. The solution requires 7 such iterations for the propeller forces to converge within a tolerance of 10^{-3} . The computational domain used in the 3-D Euler solver is shown in Figure 5.34. Figure 5.35 shows the tangential velocity contours along the center plane for both blocks. From this figure it can be seen clearly that the vortical flow induced by the propeller is cancelled downstream of the rudder trailing edge. In Figure 5.36 the axial velocity distribution is shown along the center plane, where the effect of the rudder is clearly shown.

Figure 5.37 shows the effective wake predicted at a plane located at $X_{eff} = -0.3$. The presence of the rudder causes a decrease in the axial velocity at an axial location upstream of the rudder.

The convergence of the propeller thrust and the torque coefficients with number of iterations is shown in Figure 5.38.

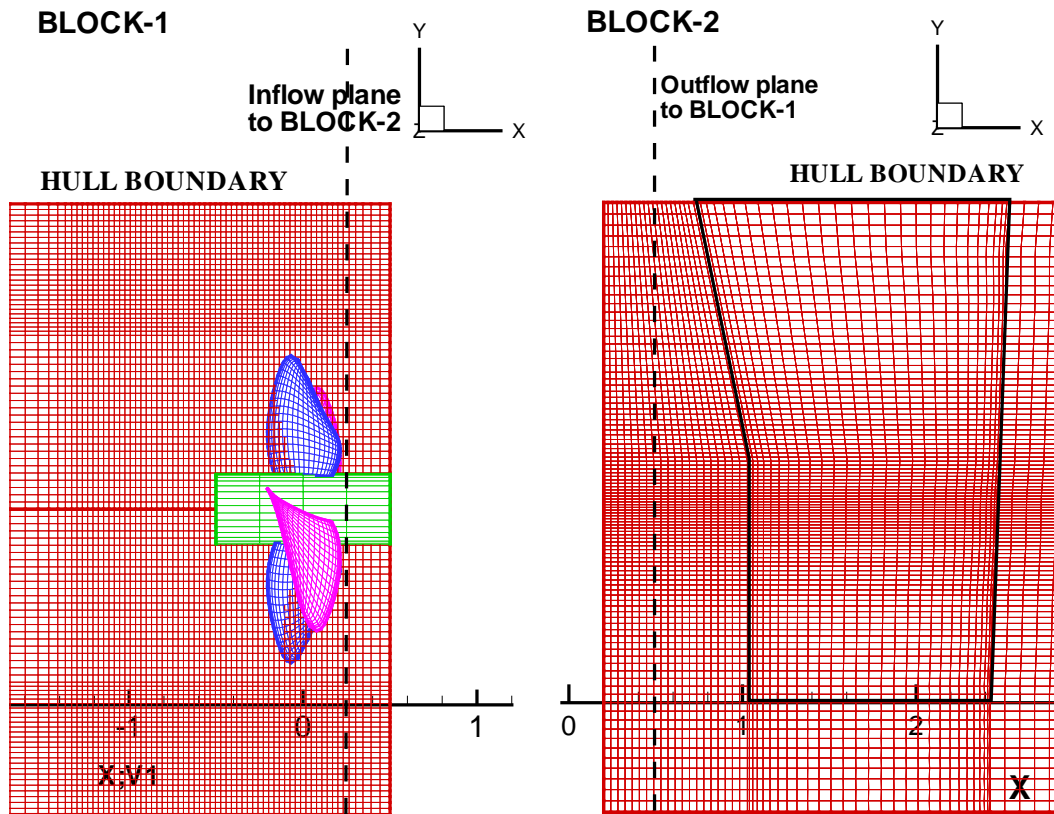


Figure 5.34: 3-D Euler solver grid showing horn-type rudder with NACA0020 section

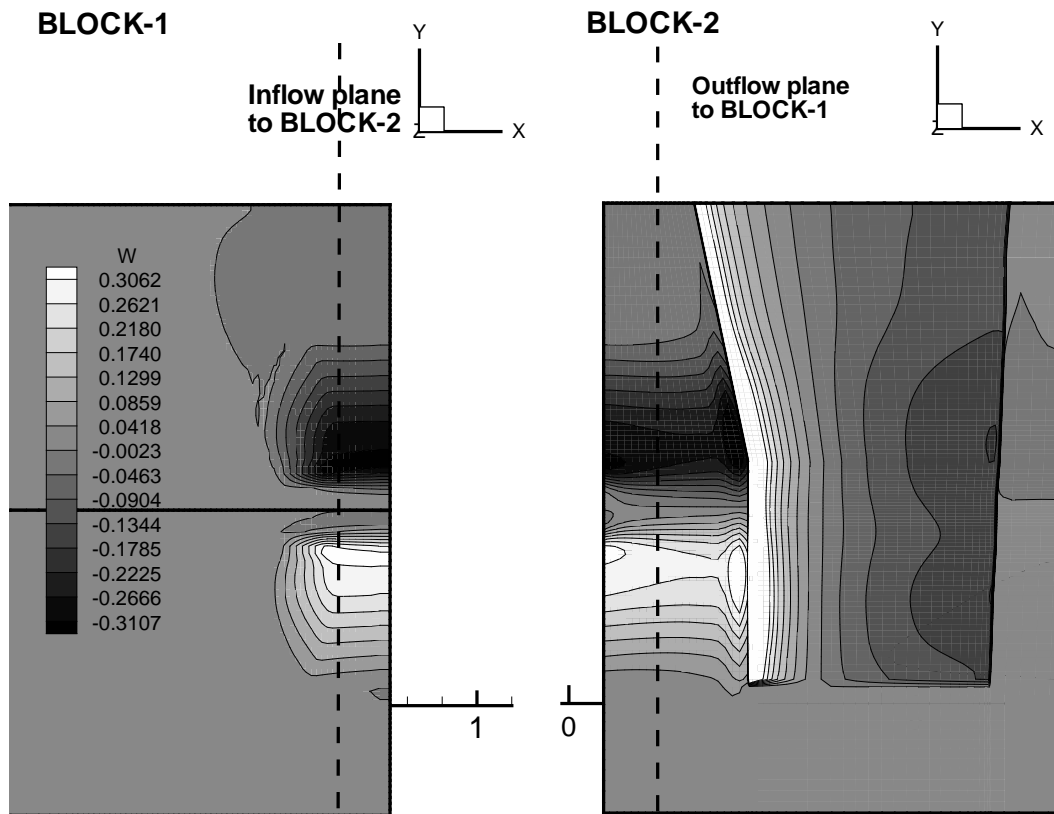


Figure 5.35: Tangential velocity contours on the center plane of block-1 and 2 for a horn-type rudder

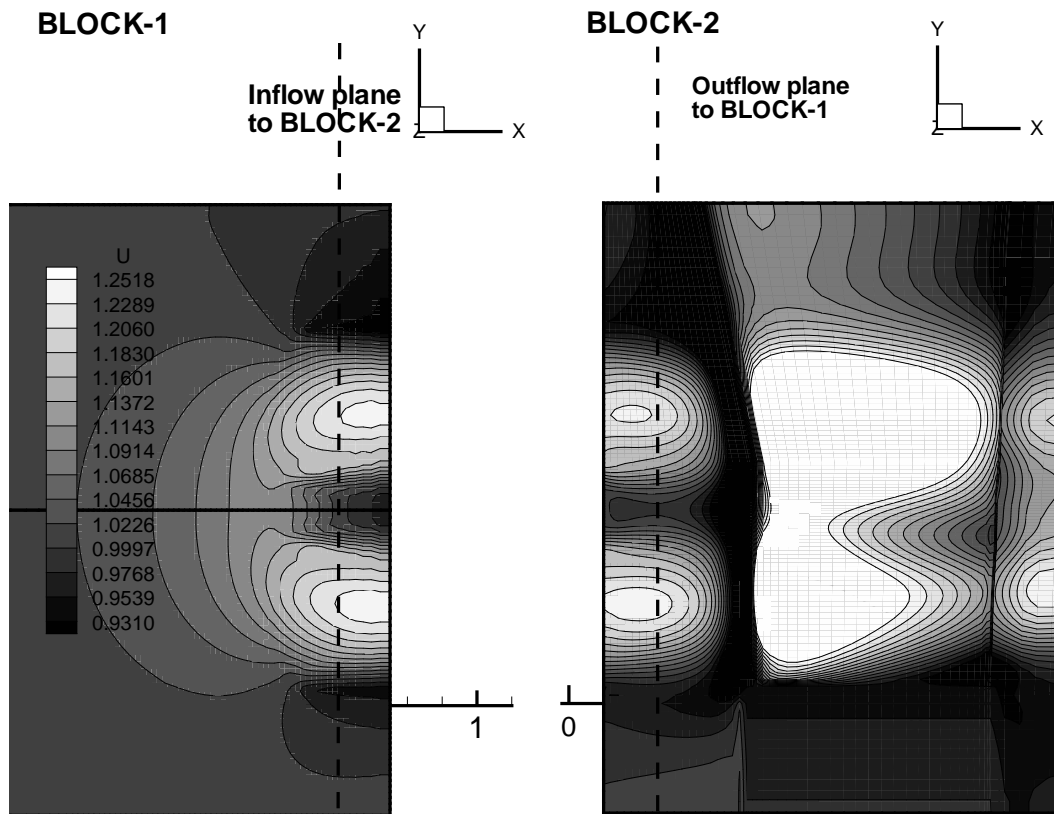


Figure 5.36: Axial velocity contours on the center plane of block-1 and 2 for a horn-type rudder

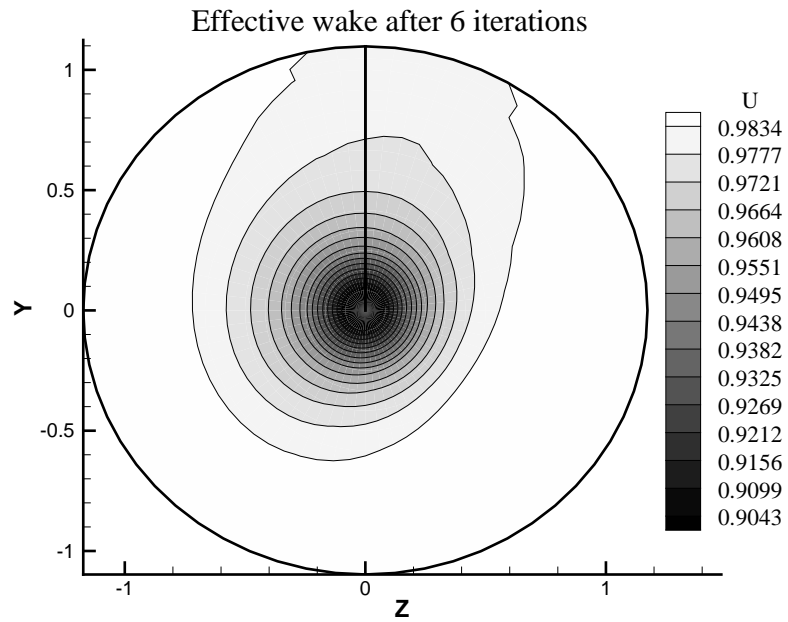


Figure 5.37: Effective wake predicted after 6 iterations with the propeller-rudder interaction

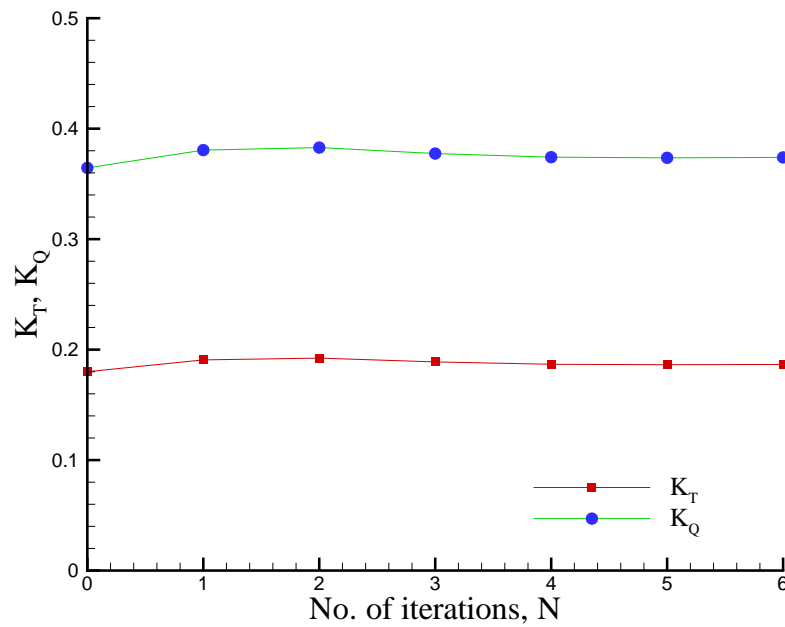


Figure 5.38: Convergence of propeller forces with the number of iterations

Chapter 6

Conclusions and Recommendations

6.1 Conclusions

In this thesis an existing low-order potential based boundary element method was extended to predict sheet cavitation over a rudder subjected to the flow induced by a propeller. The hydrostatic effects and hull effects were included in the formulation. Several convergence and validation studies were performed. The current method can predict cavitation pattern and forces over realistic rudder geometries, like horn-type rudders, flapped rudders and twisted rudders, using the propeller induced inflow. The predicted cavitation patterns were found to match reasonably well with those observed in an experiment of a horn-type rudder inside a cavitation tunnel.

An existing three-dimensional steady Euler solver was applied to predict the inflow induced by a propeller to a rudder. The method was extended to predict the flow through a square tunnel. The 3-D Euler solver was also extended to predict the flow around a rudder, where the rudder is represented as a solid boundary. The results from the 3-D Euler solver in the case of uniform flow, including the tunnel wall effects, were validated to those from an existing boundary element method.

An existing vortex-lattice method based potential flow solver applied to the propeller

was successfully coupled with the 3-D Euler solver to predict the propeller-rudder interaction, using a multi-block approach.

The simulation for the complete propeller-rudder interaction requires large computation grids and CPU time. The computations were performed with 70x50x60 cells in the propeller block and 70x100x60 cells in the rudder block. The solution required approximately 7 iterations between the two blocks for the convergence of propeller forces within a tolerance of 10^{-3} . The whole run required 96 hours of CPU time on a Compaq Professional Workstation XP1000.

The present work has extended and coupled existing numerical tools successfully to predict rudder cavitation and the complete propeller-rudder interaction.

6.2 Recommendations

The present work is only a first step in developing a robust and accurate tool to predict the propeller-rudder interaction and rudder cavitation. Following are some recommendations for future research.

** Rudder cavitation prediction*

- A horn-type rudder has a movable part and an immovable horn part. The scheme which was developed for the rudder with the flap could be extended to horn-type rudders as well. The effect of rudder angles could be modeled more accurately by developing a paneling scheme which would treat the immovable part as rigid and the movable part at an angle with respect to the pivot axis. This scheme could also predict the effect of the rudder angle on cavitation

more accurately than the present scheme of rotating the inflow, which is valid only for small angles.

- For flapped rudders and horn-type rudders there exists a gap between the movable and the immovable part. The gap flow between the components could be considered through a gap flow model as discussed in [Pyo and Suh 2000], where the gap flow is modeled as a Couette viscous flow. This gap flow effect could be incorporated in the kinematic boundary conditions at the inlet and the outlet of the gap by including the flux through the gap.
- The present method of cavitation prediction on rudders includes the effect of hull through the image model. However this assumes a flat hull and this is not always the case. Hence, the tunnel walls need to be modeled numerically. The tunnel is modeled in the BEM using adaptive gridding around the top section of the rudder, as shown in Figure 6.1. The cavitating flow around the rudder is modeled along with the tunnel in PROPCAV. The effect of one on the other could be dealt iteratively, as described in Section 5.4.1.
- The present method can also be extended to predict unsteady cavitation on rudders, in the case the unsteadiness of the propeller induced flow is considered.

* *Propeller-rudder interaction*

- The propeller-rudder interaction determined through the 3-D Euler solver need to be further validated. First, systematic convergence studies and comparisons

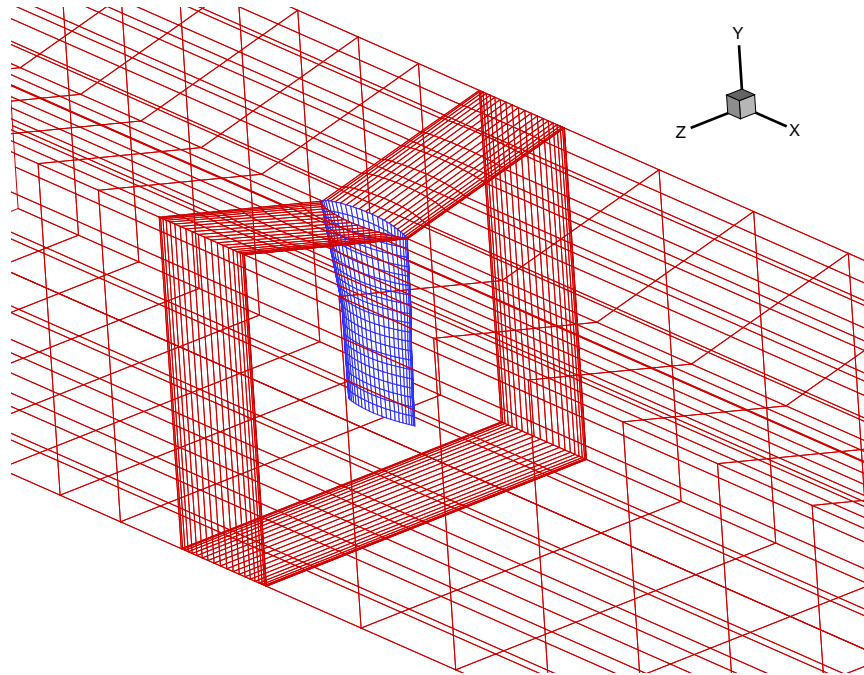


Figure 6.1: Tunnel geometry adapted with the top section of the rudder (modeled in BEM)

with results of other methods need to be performed. Then, the results predicted from the 3-D Euler solver need to be compared with those measured in experiments.

- The 3-D Euler solver, could be extended to apply to more realistic rudder geometries such as rudders with flap and twisted rudders.
- The multi-block approach could be extended to determine the flow past multi-component propulsor systems such as twin-podded propulsors and torpedo rudders. The twin-pod is a propulsor system with two podded propulsor units operating on either side (port and starboard) of the ship. A torpedo rudder is a steering device, where the rudder is mounted over a pod as shown in Figure 6.2 taken From [Halstensen 2002].

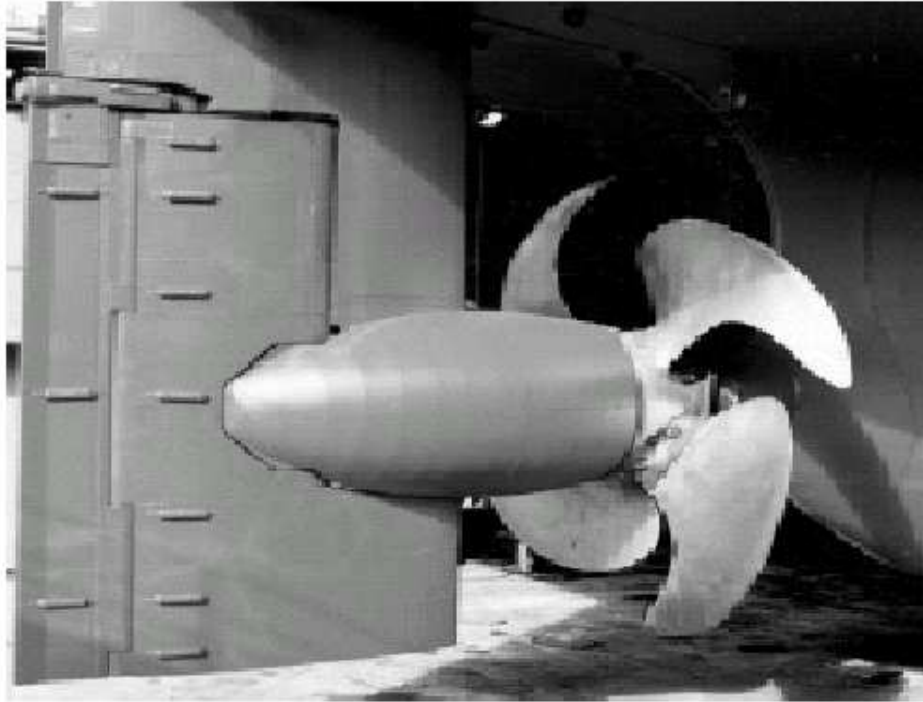


Figure 6.2: Torpedo rudder from [Halstensen 2002]

Generating a grid over a torpedo rudder is a difficult task. This could be overcome by modeling the components separately in two different blocks, where the pod along with the propeller is represented in one block, and the rudder is represented as a solid boundary in the other block. The generated grids over the two blocks will have to be non-matching. Through this multi-block approach, the information on the boundaries could be exchanged between the blocks through interpolations. The velocities and the pressure predicted in the block with the pod is given as inflow condition to the block with the rudder. Similarly, the pressures over the rudder predicted from the block with the rudder is transferred to the block with the pod. Iterations between the blocks should be performed till the propeller forces converge.

Bibliography

- Anderson, J. (1995). *Computational Fluid Dynamics: The Basics with Applications*. McGraw-Hill, Inc., New York.
- Breslin, J., Van Houten, R., Kerwin, J., and Johnsson, C.-A. (1982). Theoretical and experimental propeller-induced hull pressures arising from intermittent blade cavitation, loading, and thickness. *Trans. SNAME*, 90.
- Choi, J. (2000). *Vortical Inflow – Propeller Interaction Using Unsteady Three-Dimensional Euler Solver*. PhD thesis, Department of Civil Engineering, The University of Texas at Austin.
- Choi, J. and Kinnas, S. (2003). Prediction of unsteady effective wake by an euler solver/vortex-lattice coupled method. *Journal of Ship Research*, Vol. 47, pp.131 144.
- Choi, J.-K. and Kinnas, S. (1998). A 3-D Euler solver and its application on the analysis of cavitating propellers. In *Proceedings of the 25th ATTC*, Iowa City, Iowa. American Towing Tank Conference.
- Choi, J.-K. and Kinnas, S. (2000a). Non-axisymmetric effective wake prediction by using an unsteady three-dimensional Euler solver. In *Propellers/Shafting '00 Symposium*, Virginia Beach, VA. Soc. Naval Arch. & Marine Engrs.

- Choi, J.-K. and Kinnas, S. (2000b). An unsteady 3-D Euler solver coupled with a cavitating propeller analysis method. In *23rd Symposium on Naval Hydrodynamics*, Val de Reuil, France.
- Choi, J.-K. and Kinnas, S. (2001). Prediction of non-axisymmetric effective wake by a 3-D Euler solver. *Journal of Ship Research*, 45(1):13–33.
- Chorin, A. J. (1967). A numerical method for solving incompressible viscous flow problems. *Journal of Computational Physics*, 2:pp.12–26.
- Courant, R., Friedrichs, K., and Lewy, H. (1967). On the partial difference equations of mathematical physics. *IBM Journal*, pages pp.215–234.
- Djomehri, M., Biswas, R., and Benitez, N. (2000). Load balancing strategies for multi-block overset grid applications. *NAS-03-007*.
- Greeley, D. and Kerwin, J. (1982). Numerical methods for propeller design and analysis in steady flow. *Trans. SNAME*, 90.
- Gu, H., Natarajan, S., Gupta, A., and Kinnas, S. (2003). GBFLOW (version 1.1) user's manual. Ocean Engineering Report 03-3, Ocean Engineering Group, UT Austin, Austin, TX.
- Halstensen, S. (2002). Efficiency rudder on fast single-screw such as ropax or container ships. *Motor Ship Marine Propulsion Conference, Copenhagen*.
- Han, J., Kong, D., Kim, Y., and Lew, J. (1999). Analysis of propeller-rudder interaction with rudder angle. *Annual Autumn Meeting of SNAK, Taejon, Korea*, pages pp. 206–209.

- Han, J., Kong, D., Song, I.-H., and Lee, C.-S. (2001). Analysis of cavitating flow around the horn-type rudder in the race of a propeller. *Fourth International Symposium on Cavitation, California Institute of Technology, Pasadena, CA USA, CAV2001:sessionB9.005.*
- Hsin, C. (1989). *Development and Analysis of Panel Methods for Propellers in Unsteady Flow*. PhD thesis, M.I.T., Department of Ocean Engineering.
- Huang, T. and Cox, B. (1977). Interaction of afterbody boundary layer and propeller. In *Symposium on Hydrodynamics of Ship and Offshore Propulsion System*, Høvik outside Oslo.
- Huang, T. and Groves, N. (1980). Effective wake : Theory and experiment. In *13th Symposium on Naval Hydrodynamics*, Tokyo.
- Huang, T., Wang, H., Santelli, N., and Groves, N. (1976). Propeller/stern boundary layer interaction on axisymmetric bodies : Theory and experiment. Technical Report DTNSRDC 76-0113, DTNSRDC.
- Hyams, D., Sreenivas, K., Sheng, C., and Nichols, S. (2000). An unstructured multi-element solution algorithm for complex geometry hydrodynamics simulations. *24th Symposium on Naval Hydrodynamics, Val de reuil, FRANCE.*
- Kakar, K. (2002). Computational Modeling of FPSO Hull Roll Motions and Two-component Marine Propulsion Systems. Master's thesis, Department of Civil Engineering, The University of Texas at Austin.
- Kerwin, J., Keenan, D., Black, S., and Diggs, J. (1994). A coupled viscous/potential flow design method for wake adapted multi-stage, ducted propulsors using generalized geometry. *Trans. SNAME*, 102.

- Kerwin, J., Kinnas, S., Lee, J.-T., and Shih, W.-Z. (1987). A surface panel method for the hydrodynamic analysis of ducted propellers. *Trans. SNAME*, 95.
- Kerwin, J., Kinnas, S., Wilson, M., and J., M. (1986). Experimental and analytical techniques for the study of unsteady propeller sheet cavitation. In *Sixteenth Symposium on Naval Hydrodynamics*, Berkeley, California.
- Kerwin, J. and Lee, C.-S. (1978). Prediction of Steady and Unsteady Marine Propeller Performance by Numerical Lifting-Surface Theory. *Trans. SNAME*, 86.
- Kerwin, J., Taylor, T., Black, S., and McHugh, G. (1997). A coupled lifting-surface analysis technique for marine propulsors in steady flow. In *Propellers/Shafting '97 Symposium*, pages 1–15 (Paper No. 20), Virginia Beach, VA. Soc. Naval Arch. & Marine Engrs.
- Kinnas, S. (1991). Leading-edge corrections to the linear theory of partially cavitating hydrofoils. *Journal of Ship Research*, 35(1):pp. 15–27.
- Kinnas, S. (1992). A general theory for the coupling between thickness and loading for wings and propellers. *Journal of Ship Research*, 36(1):pp. 59–68.
- Kinnas, S., Choi, J., Lee, H., and Young, J. (2000). Numerical cavitation tunnel. In *NCT50, International Conference on Propeller Cavitation*, Newcastle upon Tyne, England.
- Kinnas, S., Choi, J., Lee, H., Young, Y., Gu, H., Kakar, K., and Natarajan, S. (2002). Prediction of cavitation performance of single/multi-component propulsors and their interaction with the hull. *Trans. SNAME*.

- Kinnas, S. and Fine, N. (1989). Theoretical prediction of the midchord and face unsteady propeller sheet cavitation. In *Proceedings of the Fifth International Conference on Numerical Ship Hydrodynamics*, Hiroshima, Japan.
- Kinnas, S. and Fine, N. (1992). A nonlinear boundary element method for the analysis of unsteady propeller sheet cavitation. In *Nineteenth Symposium on Naval Hydrodynamics*, pages 717–737, Seoul, Korea.
- Kinnas, S. and Fine, N. (1993a). A numerical nonlinear analysis of the flow around two- and three-dimensional partially cavitating hydrofoils. *Journal of Fluid Mechanics*, 254:151–181.
- Kinnas, S. and Fine, N. E. (1993b). A boundary element method for the analysis of the flow around 3-d cavitating hydrofoils. *Journal of Ship Research*, 37:213–224.
- Kinnas, S., Griffin, P., Choi, J.-K., and Kosal, E. (1998a). Automated design of propulsor blades for high-speed ocean vehicle applications. *Trans. SNAME*, 106.
- Kinnas, S. and Hsin, C. (1992). A boundary element method for the analysis of the unsteady flow around extreme propeller geometries. *AIAA Journal*, 30(3):688–696.
- Kinnas, S., Lee, H., and Mueller, A. (1998b). Prediction of propeller blade sheet and developed tip vortex cavitation. In *22nd Symposium on Naval Hydrodynamics*, pages 182–198, Washington, D.C.
- Kinnas, S. and Pyo, S. (1999). Cavitating propeller analysis including the effects of wake alignment. *Journal of Ship Research*, 43(1):38–47.

- Kudo, T. and Kinnas, S. (1995). Application of unsteady vortex/source lattice method on supercavitating propellers. In *24th American Towing Tank Conference*, Texas A&M University.
- Lee, C.-S. (1979). *Prediction of Steady and Unsteady Performance of Marine Propellers with or without Cavitation by Numerical Lifting Surface Theory*. PhD thesis, M.I.T., Department of Ocean Engineering.
- Lee, H. and Kinnas, S. (2001). Modeling of unsteady blade sheet and developed tip vortex cavitation. In *CAV 2001: Fourth International Symposium on Cavitation*, Pasadena, CA. California Institute of Technology.
- Lee, H. and Kinnas, S. (2003). Application of bem in the prediction of unsteady blade sheet and developed tip vortex cavitation on marine propellers. *Journal of Ship Research*, Accepted for publication.
- Lee, H., Natarajan, S., and Kinnas, S. (2003). MPUF3A (version 1.2) user's manual. Ocean Engineering Report 03-2, Ocean Engineering Group, UT Austin, Austin, TX.
- Lee, J.-T. (1987). Propeller steady flow analysis program using a potential based panel method. Technical report, Department of Ocean Engineering, MIT.
- Molland, A. F. (1981). *The free-stream characteristics of ship skeg-rudders*. PhD thesis, Department of Ship Science, University of Southampton.
- Morino, L. and Kuo, C.-C. (1974). Subsonic Potential Aerodynamic for Complex Configurations : A General Theory. *AIAA Journal*, vol 12(no 2):pp 191–197.

- Mueller, A. and Kinnas, S. (1999). Propeller sheet cavitation predictions using a panel method. *Journal of Fluids Engineering*, 121:282–288.
- Natarajan, S. and Kinnas, S. (2003). GBFLOW-MB (version 1.0) user's manual. Ocean Engineering Report 03-4, Ocean Engineering Group, UT Austin, Austin, TX.
- Newman, J., Pankajakshan, R., Whitfield, D., and Taylor, L. (2002). Computational design optimization using rans. *24th Symposium on Naval Hydrodynamics, Fukuoka, JAPAN*.
- Ni, R.-H. (1982). A multiple-grid scheme for solving the Euler equations. *AIAA Journal*, 20(11):pp.1565–1571.
- Ohkusu, M., editor (1996). *Advances in Marine Hydrodynamics*. Computational Mechanics Publications, Southampton, UK.
- Pyo, S. and Suh, J. (2000). Numerical prediction of open water performance of flapped rudders. *SOTECH Vol. 4, No. 1, pp.1 10*.
- Ruprecht, A., Bauer, C., Gentner, C., and Lein, G. (1999a). Parallel computation of stator-rotor interaction in an axial turbine. *ASME PVP Conference, CFD Symposium, Boston*.
- Ruprecht, A., Bauer, C., and Heitele, M. (1999b). Unsteady forces on the blading of an axial turbine caused by stator-rotor interaction. *IAHR WG 'The Behaviour of Hydraulic Machinery under Steady Oscillatory Conditions', Brno*.
- Shen, Y., Jiang, C. W., and Kruger, K. (2000). Uss bulkeley (ddg 84) twisted rudder coordinated trial results. *NSWCCD-50-TR-2000/056*.

- Shen, Y., Remmers, K., and Jiang, C. W. (1997). Effects of ship hull and propeller on rudder cavitation. *Journal of Ship Research*, Vol. 41, No. 3, pp.172-180.
- Shih, W.-Z. (1988). *A Combined Euler Equation/Surface Panel Solution to The Shear Interaction Problem of An Open or Ducted Propeller*. PhD thesis, Department of Ocean Engineering, M.I.T.
- Stern, F., Kim, H., Patel, V., and Chen, H. (1988a). Computation of viscous flow around propeller-shaft configurations. *Journal of Ship Research*, 32(4):pp.263–284.
- Stern, F., Kim, H., Patel, V., and Chen, H. (1988b). A viscous-flow approach to the computation of propeller- hull interaction. *Journal of Ship Research*, 32(4):pp. 246–262.
- Stierman, E. (1989). The influence of the rudder on propulsive performance - part i. *International Shipbuilding Progress*, 36:pp. 303–334.
- Tamashima, M., Matsui, S., Yang, J., Mori, K., and Yamazaki, R. (1993). The method for predicting the performance of propeller-rudder system with rudder angles and its application to the rudder design. *Transaction of the West-Japan Society of Naval Architects*, 86:pp. 53–76 (in Japanese).
- Young, Y. and Kinnas, S. (1999). Numerical and experimental validation of a cavitating propeller bem code. In *Cavitation and Multiphase Flow Forum*, San Francisco, CA. 3rd ASME/JSME Joint Fluids Engineering Conference.
- Young, Y. and Kinnas, S. (2001). A bem for the prediction of unsteady midchord face and/or back propeller cavitation. *Journal of Fluids Engineering*, 123.

- Young, Y. and Kinnas, S. (2003a). Analysis of supercavitating and surface-piercing propeller flows via bem. *Journal of Computational Mechanics*.
- Young, Y. and Kinnas, S. (2003b). Numerical modeling of supercavitating propeller flows. *Journal of Ship Research*, 47:48–62.
- Young, Y. L. (2002). *Numerical Modeling of Supercavitating and Surface-Piercing Propellers*. PhD thesis, Department of Civil Engineering, The University of Texas at Austin.

Vita

Shreenaath Natarajan was born in Chennai, India on July 16, 1980. He is the son of Mohana and Natarajan Sundaram. He obtained his Bachelor of Technology in Naval Architecture from the Indian Institute of Technology at Madras in July, 2001. He started his Masters program in civil engineering at The University of Texas at Austin in September, 2001.

Permanent address: 23, Bhakthavachalam Street, West Mambalam
Chennai-600033, India

This thesis was typeset with \LaTeX^\ddagger by the author.

[‡] \LaTeX is a document preparation system developed by Leslie Lamport as a special version of Donald Knuth's \TeX Program.